Master's thesis

NTNU
Norwegian University of Science and Technology
Faculty of Natural Sciences
Department of Physics

Kristine Schüller

Detection of Millicharged Dark Matter in Underground Detectors

Master's thesis in Applied Physics and Mathematics
Supervisor: Michael Kachelrieß
February 2023

NTNU
Norwegian University of
Science and Technology

Kristine Schüller

Detection of Millicharged Dark Matter in Underground Detectors

Master's thesis in Applied Physics and Mathematics
Supervisor: Michael Kachelrieß
February 2023

Norwegian University of Science and Technology
Faculty of Natural Sciences
Department of Physics

NTNU
Norwegian University of
Science and Technology

Abstract

Millicharged particles are possible candidates in the search for dark matter, and they can be produced in cosmic ray interactions via meson decays. From the cosmic ray meson flux, we find the corresponding flux of millicharged particles that can be detected in underground detectors. From these results we construct an exclusion plot in the mass-charge plane of the millicharged particles, narrowing their possible parameter space and thus moving one step further in the search for millicharged dark matter. To improve these results we investigate the energy loss experienced by millicharged particles of different charges, masses, and incoming energies traversing the Earth toward an underground detector from all angles. We focus on the $2 \to 2$ processes of millicharged particles scattering off electrons and nuclei. As an additional result, we present initial investigations of the $2 \to 3$ process of bremsstrahlung. We find that in the already excluded region, assuming only downward-moving millicharged particles is reasonable. However, for the still open region the contribution from upward-moving particles should also be considered.

Sammendrag

Milliladede partikler er mulige kandidater i søket etter mørk materie, og de kan produseres i kosmiske stråleinteraksjoner via forfall av mesoner. Fra den kosmiske meson-fluksen finner vi den tilsvarende fluksen av milliladede partikler som kan detekteres i underjordiske detektorer. Fra disse resultatene konstruerer vi et ekslusjonsplot i masse-ladningsplanet til de milliladede partiklene, som innsnevrer deres mulige parameter-rom og dermed tar oss ett steg videre i søket etter milliladet mørk materie. For å forbedre disse resultatene undersøker vi energitapet for milliladede partikler med ulike ladninger, masser og energier når de traverserer jorden på vei mot en underjordisk detektor fra ulike vinkler. Vi fokuserer på prosessene for milliladede partikler som spres av elektroner og atomkjerner. Som et tilleggsresultat begynner vi å utforske energitapet forårsaket av bremsestråling. Resultatene våre viser at i det allerede utelukkede området av de milliladede partiklenes parameter-rom er det rimelig å anta at milliladede partikler kun når en underjordisk detektor ovenfra. For området som fortsatt er åpent burde man i tillegg ta oppadgående milliladede partikler med i betraktning.

Acknowledgements

This Master thesis is a continuation of my project thesis [1] that was written in the spring of 2022. Both were written at the Norwegian University of Science and Technology in Trondheim. Several chapters and sections are adapted from the project thesis, and they are marked as such. The work on the master thesis started in September 2022, and was finished in February 2023. It was written under the supervision of Prof. Michael Kachelrieß.

I would like to thank Prof. Michael Kachelrieß for his guidance. During our weekly meetings he has guided the way for my research, lent me useful books and helped me clear up any questions I have had. I would also like to thank him for his helpful feedback on draft versions of this thesis. I extend my thanks to Jonas Tjemsland for always being willing to help, and for our discussions. I would also like to thank my boyfriend Martin for his support and proofreading.

Kristine Schüller
February 15, 2023

Contents

List of Figures

Chapter 1

Introduction

1.1 Motivation[†]

The search for dark matter (DM) remains one of the most important unsolved problems in physics. Enormous efforts are being put into the search, both theoretically and experimentally. The discovery of DM would be considered one of the most important moments of scientific history. Even if the search does not succeed, we would be forced to reassess our current understanding of nature [2].

The history of dark matter began in 1933, when Fritz Zwicky published his article about the Coma cluster [3]. He found that the velocity dispersion of the galaxies in the cluster was so high that the system could only be stable if more matter was present than the observed visible matter [4]. He stated that this had to be due to the presence of a type of unobserved matter, which he called "dark matter" [4]. Similar results were found by other physicists shortly after, noting the discrepancy between the galaxy masses predicted by the velocity dispersions and the amount of light they emitted [4].

More observations pointing toward the existence of dark matter were made studying the rotation curves of galaxies. A rotation curve shows the orbital velocities of galaxy components as a function of distance from the galactic center, and from them, the mass of the galaxy can be determined [4]. In 1970, Rubin and Ford noted in an article [5] how the rotation curve of the Andromeda nebula remained approximately constant as a function of radius [4]. The rotation curve is shown in Figure 1.1. In the early 1970s, more articles on rotation curves were

[†]Adapted from [1].

published, and it was noted that the rotation curves of galaxies tend to be flat, a feature which suggests that there is more mass present than the light of the galaxies indicates [4]. The flatness of the rotation curves can thus be used as an argument for the existence of DM [4].

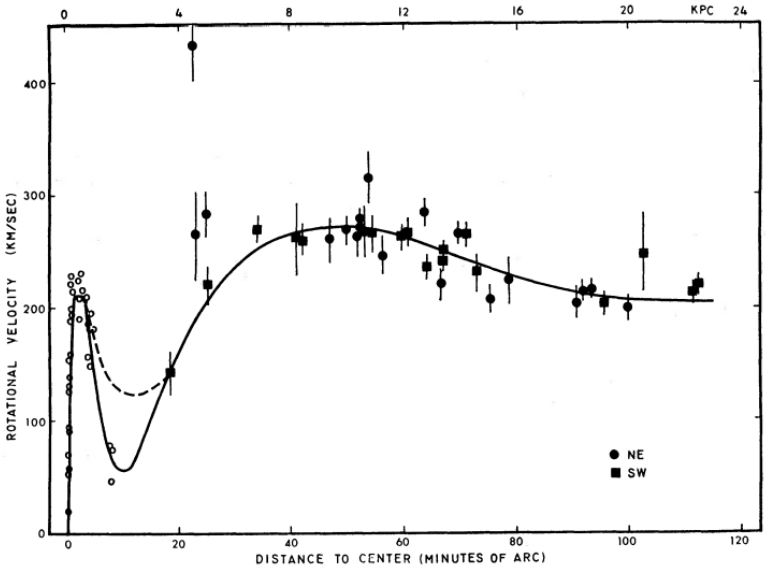

Figure 1.1: Rotation curve made by Rubin and Ford, taken from their 1970 article [5]. The curve shows optically studied rotation of ionized hydrogen in the Andromeda galaxy [4].

Initially, the presence of unobserved matter was seen as just one of many possible explanations for these observations regarding the velocity dispersions and rotation curves of galaxies [4]. It was only later that the problems of the discrepancy between the mass predicted by the emitted light of galaxies and their velocity dispersions or rotational curves were identified as two problems with the same explanation: the existence of DM [4].

Initially, the term "dark matter" was used to refer to dark astrophysical objects such as dark stars, planets or cold gas. Today, it refers to the unknown particles that make up the bulk of the matter density of the universe [6]. Due to the discovery of atmospheric neutrino oscillations in the Super-Kamiokande (SK) experiment, there is strong evidence for massive neutrinos as non-baryonic

candidates for DM [7]. However, even if the neutrino mass is up to 5 eV, they still could not account for all the DM in the universe [7], and neither can diffuse baryons [2]. Thus, other candidates have to be investigated. Today most physicists agree that DM has to consist of particles outside the standard model (SM) [6]. There are several promising beyond SM candidates of DM, which makes the DM search very intriguing.

The DM particles have to satisfy various criteria. Most importantly, they have to interact weakly with the SM particles, otherwise they should already have been detected. Research is progressively reducing the allowed regions of the parameter spaces of possible DM particles. Because of this, lighter DM particles in the sub-GeV range have recently attracted increasing attention. It has recently been noted that cosmic rays can be a possible source of detectable DM particles in this mass range [8].

1.1.1 MCPs as candidates for dark matter

From the known particles of the SM, it seems that all particles have an electric charge that is a multiple of 1/3 e, where e is the electron charge. However, it is theoretically possible that there exist particles with electric charge ϵe, where ϵ can be any real number [9]. A particle with $\epsilon \ll 1$ is called a millicharged particle (MCP), and it is a possible candidate for DM.

An MCP is a generic particle with a charge much smaller than the electron charge. The small charge makes the MCP weakly coupled to the SM photon, and due to this coupling, the Feynman rules of quantum electrodynamics (QED) can be applied to MCPs as long as the photon coupling is scaled by the size of the MCP charge. MCPs can be produced through the decay of cosmic ray mesons, and by applying the Feynman rules for QED to the MCPs we can calculate the MCP flux resulting from cosmic ray interactions, as done by Kachelrieß and Tjemsland in [8]. By combining the estimated MCP flux with experimental detector results, we can place restrictions on which MCPs stand as candidates for DM.

Observations of MCPs would not only give us information about what DM is made up of, but it would also prove that particles with charges not being a multiple of 1/3 e can exist. Thus, investigating the parameter space of MCPs is an important task in the intriguing search for new physics.

1.2 Outline

The energy loss experienced by MCPs when traversing the Earth can affect the expected MCP signal in an underground detector. This thesis is devoted to investigating the Earth attenuation of a flux of MCPs produced in cosmic rays.

Firstly, we find the flux of MCPs from the cosmic ray meson flux. We then use these results together with experimental data to construct an exclusion plot in the MCP mass-charge plane, reproducing the results found in [8]. As a manner of improving the exclusion plot, we investigate the energy loss of MCPs traversing the Earth on their way toward an underground detector. Our main goal is to investigate the attenuation of the MCP flux due to the $2 \to 2$ scattering processes of MCPs scattering off electrons and nuclei. As an additional result, initial investigations of the $2 \to 3$ process of MCP bremsstrahlung are presented.

The first few chapters present the theory needed for obtaining our results. Chapter 2 summarizes the basics of particle kinematics. We then present some general theory about MCPs in Chapter 3, including how they can be produced in meson decays. Further, we summarize how MCPs can be detected in experiments and explain how to make exclusion plots in their mass-charge plane. Then the Feynman rules for QED are summarized in Chapter 4, and how they can be applied to MCPs is explained. Finally, we look at the Earth attenuation of MCPs along their path toward an underground detector in Chapter 5. This is done separately for scattering off electrons and nuclei, and for the process of bremsstrahlung.

Our results are presented in Chapter 6. Firstly, the results for the integrated MCP flux and the resulting exclusion plot in the mass-charge plane of MCPs are shown. Then we present the results related to the calculated energy loss of MCPs traversing the Earth due to them scattering off electrons and nuclei. For the case of bremsstrahlung, numerical problems were present, and we discuss possible ways of approaching these issues.

In Chapter 7 we discuss the accuracy of our results and present suggestions for further work. We also discuss the reasonableness of our assumptions and approximations and present some upcoming experiments. Finally, we conclude and reflect on the impact of our results in Chapter 8.

1.3 Conventions and notation[†]

We define e as the negative electron charge. We use natural units, setting $\hbar = c = 1$, where $\hbar$ is Planck's reduced constant and c is the speed of light. We use the following convention for the metric tensor:

$$g_{\mu\nu} = \begin{pmatrix} 1 & 0 & 0 & 0 \\ 0 & -1 & 0 & 0 \\ 0 & 0 & -1 & 0 \\ 0 & 0 & 0 & -1 \end{pmatrix}. \tag{1.1}$$

Four-vectors are denoted by light italic type (p), while three-vectors are denoted by bold type ($\mathbf{p}$). The scalar product between two four-vectors p and q is defined as

$$p^\mu q_\mu = g_{\mu\nu} p^\mu q^\nu = p^0 q^0 - p^i q^i = p^0 q^0 - \mathbf{p} \cdot \mathbf{q}, \tag{1.2}$$

where we use the Einstein summation convention, summing over repeated indices. We use Greek letters for four-vectors and Latin letters for three-vectors.

In the Dirac representation, the 4×4 gamma matrices γ^μ are defined by

$$\gamma^0 = \begin{pmatrix} \mathbb{1} & 0 \\ 0 & -\mathbb{1} \end{pmatrix} \tag{1.3}$$

and

$$\gamma^i = \begin{pmatrix} 0 & \sigma^i \\ -\sigma^i & 0 \end{pmatrix}, \tag{1.4}$$

where $\mathbb{1}$ is the 2×2 identity matrix and σ^i are the Pauli spin matrices defined by

$$\sigma^1 = \begin{pmatrix} 0 & 1 \\ 1 & 0 \end{pmatrix}, \quad \sigma^2 = \begin{pmatrix} 0 & -\mathrm{i} \\ \mathrm{i} & 0 \end{pmatrix}, \quad \sigma^3 = \begin{pmatrix} 1 & 0 \\ 0 & -1 \end{pmatrix}. \tag{1.5}$$

We use the Feynman slash notation where

$$\not{p} = \gamma^\mu p_\mu. \tag{1.6}$$

For a particle a, we denote its four-momentum by p_a, its mass by m_a, and its energy by E_a. To avoid confusion, we generally name incoming particles using letters and outgoing particles using numbers.

[†]Adapted from [1].

Chapter 2

Kinematics

This chapter gives a brief summary of important concepts and relations that we will use in our calculations for MCPs later on.

2.1 Lorentz transformations[†]

The section is based on Section 43 in [10]. The momentum four-vector for a particle is denoted by $p = (E, \mathbf{p})$, where E is the energy of the particle and $\mathbf{p}$ is its three-momentum. The square of the four-momentum is given by

$$p^2 = p^\mu p_\mu = E^2 - |\mathbf{p}|^2 = m^2, \tag{2.1}$$

where m is the invariant mass of the particle. The velocity of the particle is given by $\boldsymbol{\beta} = \mathbf{p}/E$, and the Lorentz factor γ is defined as

$$\gamma = \frac{1}{\sqrt{1-\beta^2}} = \frac{E}{m}, \tag{2.2}$$

which goes toward infinity as the particle's velocity approaches the speed of light. Lorentz transformations transform quantities from one inertial frame to another. The energy and momentum of a particle $p = (E, \mathbf{p})$ as seen from a frame moving at a relative velocity of β_f are given by

$$\begin{pmatrix} E^* \\ \mathbf{p}^*_\parallel \end{pmatrix} = \begin{pmatrix} \gamma_f & -\gamma_f\beta_f \\ -\gamma_f\beta_f & \gamma_f \end{pmatrix} \begin{pmatrix} E \\ \mathbf{p}_\parallel \end{pmatrix} \tag{2.3}$$

[†]Adapted from [1].

and

$$\mathbf{p}_T^* = \mathbf{p}_T, \tag{2.4}$$

where $\mathbf{p_T}$ is the part of $\mathbf{p}$ perpendicular to $\boldsymbol{\beta_f}$, $\mathbf{p}_\parallel$ is the part of $\mathbf{p}$ parallel to $\boldsymbol{\beta_f}$ and γ_f is the Lorentz factor corresponding to $\beta_\mathbf{f}$. The square of the four-momentum defined in Equation (2.1) is a Lorentz-invariant quantity, which means it remains constant under Lorentz transformations. Other four-vectors transform in the same way as the four-momentum in Equation (2.3).

We will do our calculations in either the center of momentum (CM) frame or in the lab frame. The CM frame is the frame in which the total momentum of the incoming particles is zero, and we will use the superscript * to denote CM variables. The lab frame is defined as the frame in which the target particle is at rest. Figure 2.1 shows an illustration of a collision in both frames.

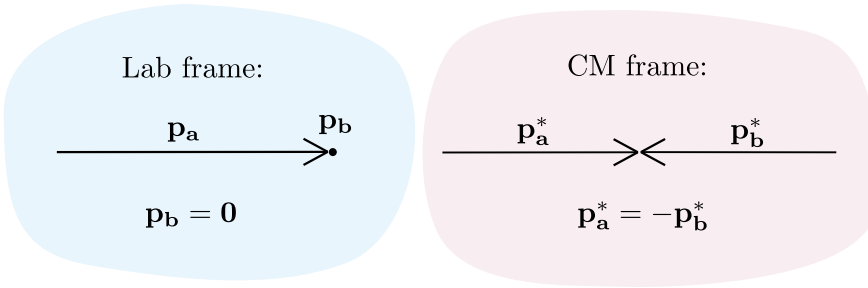

Figure 2.1: Illustration of the lab frame and CM frame for two colliding particles a and b. $\mathbf{p_a}$ is the three-momentum of particle a, while $\mathbf{p_b}$ is the three-momentum of particle b. The superscript * denotes variables in the CM frame.

2.2 Decay rates[†]

In this section, we present some useful formulas for particle decays, as presented in Chapter 6 in [11]. The decay rate for a given particle decay gives the probability for the decay to happen within a given period of time. The decay rate is given by the product of the absolute square of the amplitude, $|\mathcal{M}|^2$, and the phase space. The phase space factor is kinematic, and it depends on the

[†]Adapted from [1].

energies, masses, and momenta of the particles involved in the decay. The amplitude is dynamical, and it is calculated using the appropriate Feynman rules for evaluating the Feynman diagrams of the decay. The Feynman rules for QED will be given in Section 4.1. The decay rate Γ of a particle a into the particles $1, 2, ..., n$ is given by

$$\begin{aligned}\Gamma =& \frac{S}{2m_a} \int |\mathcal{M}|^2 (2\pi)^4 \delta^4 (p_a - p_1 - p_2 - ... - p_n) \\ & \times \prod_{j=1}^{n} 2\pi \delta \left(p_j^2 - m_j^2\right) \Theta \left(p_j^0\right) \frac{\mathrm{d}^4 p_j}{(2\pi)^4},\end{aligned} \tag{2.5}$$

where m_i is the mass and p_i is the four-momentum of particle i, Θ is the Heaviside step function, δ is the Dirac delta function, and S is the symmetry factor. The symmetry factor corrects for double counting if there are identical particles in the final state. The integral over the time components can easily be done by utilizing the delta functions.

The branching ratio (BR) for a decay is the fraction of decaying particles that decay by a given decay mode. The BR for a given decay mode Γ_i is defined as

$$\mathrm{BR}_i = \frac{\Gamma_i}{\Gamma_{\mathrm{tot}}}, \tag{2.6}$$

where Γ_{tot} is the sum of the individual decay rates:

$$\Gamma_{\mathrm{tot}} = \sum_{i=1}^{n} \Gamma_i. \tag{2.7}$$

2.2.1 Two-body decays

For a two-particle decay, we use the delta functions to do the integral over the time components so that we can rewrite Equation (2.5) as

$$\begin{aligned}\Gamma =& \frac{S}{2m_a} \int |\mathcal{M}|^2 (2\pi)^4 \delta^4 (p_a - p_1 - p_2) \\ & \times \frac{1}{2\sqrt{\mathbf{p_1}^2 + m_1^2}} \frac{1}{2\sqrt{\mathbf{p_2}^2 + m_2^2}} \frac{\mathrm{d}^3 \mathbf{p_1}}{(2\pi)^3} \frac{\mathrm{d}^3 \mathbf{p_2}}{(2\pi)^3},\end{aligned} \tag{2.8}$$

which is a more useful format for doing calculations.

2.2.2 Three-body decays

We will summarize some important relations for three-body decays given in Section 43.4.3 in [10]. We consider a three-body decay where the incoming particle a decays into three particles 1, 2, and 3. We define

$$\begin{aligned} p_{ij} =& p_i + p_j, \\ m_{ij}^2 =& p_{ij}^2. \end{aligned} \tag{2.9}$$

The differential decay rate for a three-body decay can be written as

$$\mathrm{d}\Gamma = \frac{1}{(2\pi)^5} \frac{1}{16 m_a^2} |\mathcal{M}|^2 \, |\mathbf{p_1'}| \, |\mathbf{p_3}| \, \mathrm{d}m_{12} \mathrm{d}\Omega_1^{'} \mathrm{d}\Omega_3, \tag{2.10}$$

where $(|\mathbf{p_1'}|, \Omega_1^{'})$ is the momentum of particle 1 in the rest frame of particles 1 and 2, and Ω_3 is the solid angle of particle 3 in the rest frame of the decaying particle. The absolute values of the three-momenta $|\mathbf{p_1'}|$ and $|\mathbf{p_3}|$ can be expressed as

$$|\mathbf{p_1'}| = \frac{\left[(m_{12}^2 - (m_1 + m_2)^2)(m_{12}^2 - (m_1 - m_2)^2)\right]^{1/2}}{2 m_{12}} \tag{2.11}$$

and

$$|\mathbf{p_3}| = \frac{\left[(m_a^2 - (m_{12} + m_3)^2)(m_a^2 - (m_{12} - m_3)^2)\right]^{1/2}}{2 m_a}. \tag{2.12}$$

A scatter plot of $\mathrm{d}\Gamma$ with axes m_{12}^2 and m_{23}^2 is called a Dalitz plot. Dalitz plots are a useful tool for gaining information about the squared amplitude of a decay. The higher the density of points in a region, the higher the probability for the corresponding event to occur. A constant $|\bar{\mathcal{M}}|^2$ gives a constant probability for each event inside the allowed region of the plot. A qualitative sketch of a Dalitz plot is shown in Figure 2.2, with the kinematic limits indicated in the figure. The allowed region is the area that corresponds to kinematically allowed decays, marked in blue in Figure 2.2. The standard form of writing the partial decay rate for the Dalitz plot is

$$\mathrm{d}\Gamma = \frac{1}{(2\pi)^3} \frac{1}{32 m_a^3} |\bar{\mathcal{M}}|^2 \mathrm{d}m_{12}^2 \mathrm{d}m_{23}^2. \tag{2.13}$$

For a given value of m_{12}, the maximum and minimum values of m_{23} are

$$(m_{23}^2)_{\max} = \left(E_2^{'} + E_3^{'}\right)^2 - \left(\sqrt{E_2^{'2} - m_2^2} - \sqrt{E_3^{'2} - m_3^2}\right)^2 \tag{2.14}$$

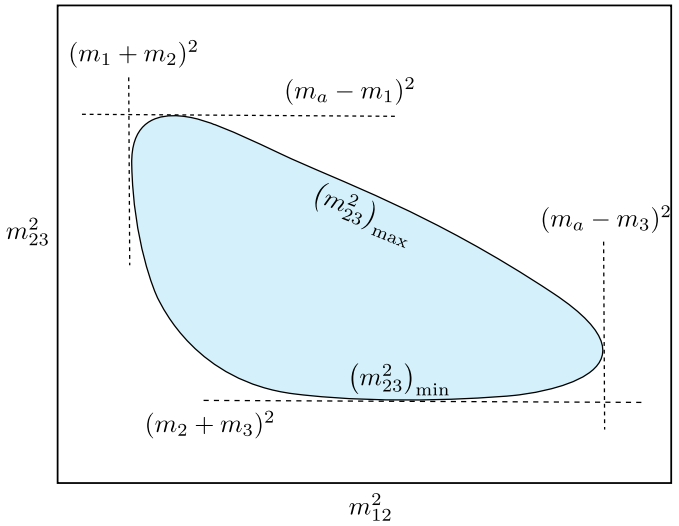

Figure 2.2: Sketch of a Dalitz plot illustrating the kinematical limits restricting the allowed phase space region. The allowed region is marked in blue.

and

$$(m^2_{23})_{\min} = \left(E_2^{'} + E_3^{'}\right)^2 - \left(\sqrt{E_2^{'2} - m_2^2} + \sqrt{E_3^{'2} - m_3^2}\right)^2 , \tag{2.15}$$

where $E_2^{'}$ and $E_3^{'}$ are the energies of particles 2 and 3 in the rest frame of particles 1 and 2. These energies can be expressed as

$$E_2^{'} = \frac{1}{2m_{12}}\left(m^2_{12} - m_1^2 + m_2^2\right) \tag{2.16}$$

and

$$E_3^{'} = \frac{1}{2m_{12}}\left(m_a^2 - m^2_{12} - m_3^2\right). \tag{2.17}$$

2.3 Scattering cross sections

The cross section for particle scattering is the product of the absolute square of the amplitude for the process, the flux factor and the phase space. For two

particles a and b scattering with an n-body final state the differential cross section is given by

$$\mathrm{d}\sigma = \frac{1}{F}|\mathcal{M}|^2 \mathrm{d}\Phi_n \left(p_a + p_b; p_1, \ldots, p_n\right), \tag{2.18}$$

where F is the flux factor and $\mathrm{d}\Phi_n$ describes the phase space [12]. In the lab frame, the flux factor can be written as

$$4\sqrt{\left(p_a \cdot p_b\right)^2 - m_a^2 m_b^2}(2\pi)^{3n-4} = 4m_b|\mathbf{p_a}|(2\pi)^{3n-4}, \tag{2.19}$$

where we have gathered all the factors of 2π [12].

2.3.1 Scattering of two particles into two particles

We define the variables for a two-body scattering process as shown in Figure 2.3. The Mandelstam variables are defined by

$$\begin{aligned} s &= \left(p_a + p_b\right)^2 = \left(p_1 + p_2\right)^2, \\ t &= \left(p_a - p_1\right)^2 = \left(p_b - p_2\right)^2, \\ u &= \left(p_a - p_2\right)^2 = \left(p_b - p_1\right)^2, \end{aligned} \tag{2.20}$$

and they represent useful Lorentz-invariant quantities for two-body scattering [12]. They satisfy

$$s + t + u = \sum m_i^2, \tag{2.21}$$

which is often useful in calculations [12].

2.3.2 Scattering of two particles into three particles

This section is based on [13], and it gives all the formulas necessary to compute the phase space integral for $2 \to 3$ scattering. The equations will be given without derivation, more details are given in [13]. We will start by describing the phase space using two invariants and two angles. Then we will show how these two angles can be expressed using invariants. Lastly, limits will be given for all integration variables.

We name our particles as shown in Figure 2.4, where the incoming particles are referred to as a and b, and the outgoing particles as 1, 2, and 3. The standard

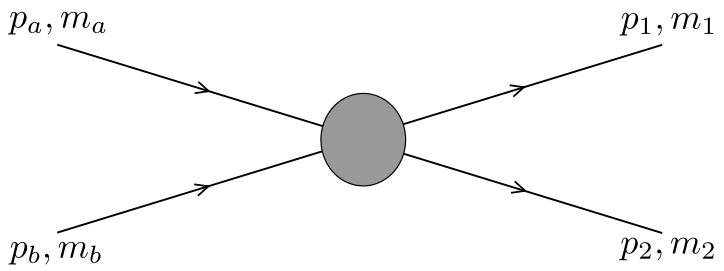

Figure 2.3: $2 \to 2$ scattering. The incoming momenta are denoted by p_a and p_b, while the outgoing momenta are denoted by p_1 and p_2.

set of five invariants for $2 \to 3$ scattering is

$$\begin{aligned} s &= (p_a + p_b)^2 = (p_1 + p_2 + p_3)^2, \\ s_1 &= (p_1 + p_2)^2 = (p_a + p_b - p_3)^2, \\ s_2 &= (p_2 + p_3)^2 = (p_a + p_b - p_1)^2, \\ t_1 &= (p_a - p_1)^2 = (p_2 + p_3 - p_b)^2, \\ t_2 &= (p_b - p_3)^2 = (p_1 + p_2 - p_a)^2, \end{aligned} \tag{2.22}$$

where s is fixed, while s_1, s_2, t_1, and t_2 vary.

We can look at the $2 \to 3$ scattering process as two subsequent processes; $2 \to 2$ scattering followed by a $1 \to 2$ decay process. We choose p_2 and p_3 as the intermediate system. Figure 2.5 shows an illustration of the factorization. By applying Equation (2.21) to the $2 \to 2$ scattering $a, b \to 1, s_2$, we can define five more invariants as linear combinations of s_1, s_2, t_1, and t_2. These allow us to rewrite expressions using only the five standard invariants. They are given by

$$\begin{aligned} t_{a2} &= (p_a - p_2)^2 = t_2 - t_1 - s_1 + m_a^2 + m_1^2 + m_2^2, \\ t_{b2} &= (p_b - p_2)^2 = t_1 - t_2 - s_2 + m_b^2 + m_2^2 + m_3^2, \\ t_{a3} &= (p_a - p_3)^2 = s_1 - s - t_2 + m_a^2 + m_b^2 + m_3^2, \\ t_{b1} &= (p_b - p_1)^2 = s_2 - s - t_1 + m_a^2 + m_b^2 + m_1^2, \\ s_{13} &= (p_1 + p_3)^2 = s - s_1 - s_2 + m_1^2 + m_2^2 + m_3^2. \end{aligned} \tag{2.23}$$

Using Equations (2.22) and (2.23) we can express the ten different scalar products that can arise for general $2 \to 3$ scattering using the five standard

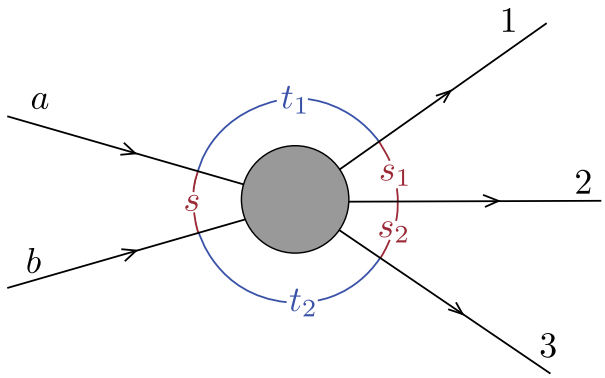

Figure 2.4: Two particles scattering into three particles, where a and b are the incoming particles, and 1, 2, and 3 are the outging particles. The five standard invariants for $2 \to 3$ scattering are shown in between the particle lines.

invariants:

$$\begin{aligned}
2(p_a \cdot p_b) &= s - m_a^2 - m_b^2, \\
2(p_a \cdot p_1) &= m_a^2 + m_1^2 - t_1, \\
2(p_a \cdot p_2) &= s_1 + t_1 - t_2 - m_1^2, \\
2(p_a \cdot p_3) &= s - s_1 + t_2 - m_b^2, \\
2(p_b \cdot p_1) &= s - s_2 + t_1 - m_a^2, \\
2(p_b \cdot p_2) &= s_2 + t_2 - t_1 - m_3^2, \\
2(p_b \cdot p_3) &= m_b^2 + m_3^2 - t_2, \\
2(p_1 \cdot p_2) &= s_1 - m_1^2 - m_2^2, \\
2(p_1 \cdot p_3) &= s - s_1 - s_2 + m_2^2, \\
2(p_2 \cdot p_3) &= s_2 - m_2^2 - m_3^2,
\end{aligned} \tag{2.24}$$

which is useful for rewriting the amplitude for the interaction in terms of invariants only.

Factorizing the phase space integral into the $2 \to 2$ and $1 \to 2$ processes shown in Figure 2.5, it can be written as

$$R_3(s) = \int \mathrm{d}s_2 R_{2\to 2}\left(s, m_1^2, s_2\right) R_{2\to 1}\left(s_2, m_2^2, m_3^2\right), \tag{2.25}$$

where $R_{2\to2}$ corresponds to the $2 \to 2$ scattering and $R_{1\to2}$ corresponds to the $1 \to 2$ process. We can express $R_{2\to2}$ as

$$\begin{aligned} R_{2\to2}(s) =& \frac{1}{4}\lambda^{-1/2}\left(s, m_a^2, m_b^2\right) \\ &\times \int_0^{2\pi} \int \mathrm{d}\phi \mathrm{d}t \Theta\left(1 - \cos^2\theta_{a1}^*\right) \Theta\left(E_1^* - m_1\right), \end{aligned} \tag{2.26}$$

where ϕ is the rotation angle around the beam axis, θ_{a1}^* is the CM scattering angle, and E_1^* is the energy of particle 1 in the CM frame. The function λ is defined by

$$\lambda(x, y, z) = (x - y - z)^2 - 4yz. \tag{2.27}$$

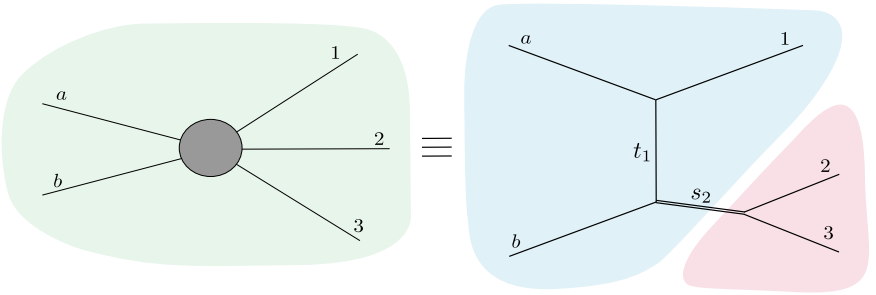

Figure 2.5: Illustration of the factorization of a $2 \to 3$ scattering process into $2 \to 2$ scattering followed by a $1 \to 2$ decay.

We can express $R_{1\to2}$ as

$$R_{1\to2}(s) = \frac{|\mathbf{p_3}|^{R23}}{4\sqrt{s}} \int \mathrm{d}\Omega_3^{R23}, \tag{2.28}$$

where $|\mathbf{p_3}|^{R23}$ is in the R23 frame and Ω_3^{R23} is the solid angle in the R23 frame. The R23 frame is the frame in which $\mathbf{p_3}+\mathbf{p_2} = 0$. In this frame, $\mathbf{p_a}+\mathbf{p_b}-\mathbf{p_1} = 0$, and the vectors $\mathbf{p_a}$, $\mathbf{p_b}$, and $\mathbf{p_1}$ form a plane.

Inserting Equations (2.26) and (2.28) into Equation (2.25) we get

$$R_3 = \frac{1}{8\sqrt{s}|\mathbf{p_a}|^*} \int_0^{2\pi} \mathrm{d}\phi \int\int \mathrm{d}t_1 \mathrm{d}s_2 \frac{|\mathbf{p_3}|^{R23}}{4\sqrt{s_2}} \int \mathrm{d}\Omega_3^{R23}, \tag{2.29}$$

where

$$|\mathbf{p_3}|^{R23} = \frac{\lambda^{1/2}(s_2, m_2^2, m_3^2)}{2\sqrt{s_2}}. \tag{2.30}$$

We choose to work in the Jackson frame, which is the frame where $\mathbf{p_b}$ is used as the polar axis to define the orientation of $\mathbf{p_3}$. In this frame the polar angle is defined as

$$\cos\theta_{b3}^{R23} = \frac{\mathbf{p_b}\cdot\mathbf{p_3}}{|\mathbf{p_b}||\mathbf{p_3}|}, \tag{2.31}$$

and it varies between 0 and π. The azimuthal angle is called the Treiman-Yang angle, and it is defined by

$$\cos\phi_b = -\frac{(\mathbf{p_b}\times\mathbf{p_1})\cdot(\mathbf{p_b}\times\mathbf{p_3})}{|\mathbf{p_b}\times\mathbf{p_1}||\mathbf{p_b}\times\mathbf{p_3}|}. \tag{2.32}$$

We have that

$$\mathrm{d}\Omega_3^{R23} = \mathrm{d}\cos\theta_{b3}^{R23}\mathrm{d}\phi_b, \tag{2.33}$$

and we want to express these angles in terms of the five standard invariants in Equation (2.22). Thus, we need to know the relation between $\cos\theta_{b3}^{R23}$ and t_2, and between ϕ_b and s_1.

The relation between $\cos\theta_{b3}^{R23}$ and t_2 is linear, and it is given by

$$\begin{aligned} t_2 =& m_b^2 + m_3^2 - \frac{1}{2s_2}\left(s_2 + m_b^2 - t_1\right)\left(s_2 + m_3^2 - m_2^2\right) \\ &+ \cos\theta_{b3}^{R23}\frac{1}{2s_2}\lambda^{1/2}\left(s_2, m_b^2, t_1\right)\lambda^{1/2}\left(s_2, m_3^2, m_2^2\right). \end{aligned} \tag{2.34}$$

We also have a linear relationship between the Treiman-Yang angle ϕ_b and s_1:

$$\begin{aligned} \cos\phi_b =& -\det\begin{bmatrix} 2m_b^2 & s_2 - t_1 + m_b^2 & m_b^2 + m_3^2 - t_2 \\ s_2 - t_1 + m_b^2 & 2s_2 & s_2 - m_2^2 + m_3^2 \\ s - m_a^2 + m_b^2 & s + s_2 - m_1^2 & s - s_1 + m_3^2 \end{bmatrix} \\ &\times 2\left[G(s, t_1, s_2, m_a^2, m_b^2, m_1^2)G(s_2, t_2, m_3^2, t_1, m_b^2, m_2^2)\right]^{1/2}, \end{aligned} \tag{2.35}$$

where

$$G(x, y, z, u, v, w) = -\frac{1}{2}\det\begin{bmatrix} 0 & 1 & 1 & 1 & 1 \\ 1 & 0 & v & x & z \\ 1 & v & 0 & u & y \\ 1 & x & u & 0 & w \\ 1 & z & y & w & 0 \end{bmatrix}. \tag{2.36}$$

Expressing the integral over Ω_3^{R23} in terms of invariants, the phase space integral in Equation (2.29) becomes

$$R_3(s) = \frac{\pi}{16\lambda^{1/2}\left(s, m_a^2, m_b^2\right)} \int \frac{\mathrm{d}t_1 \mathrm{d}s_2 \mathrm{d}t_2 \mathrm{d}s_1}{(-\Delta_4)^{1/2}}, \tag{2.37}$$

where Δ_4 is the 4×4 symmetric Gram determinant. Using the standard set of five invariants the Gram determinant can be written as

$$\Delta_4 = \frac{1}{16} \det \begin{bmatrix} 2s_2 & s_2 - t_1 + m_b^2 & s + s_2 - m_1^2 & s_2 - m_2^2 + m_3^2 \\ s_2 - t_1 + m_b^2 & 2m_b^2 & s - m_a^2 + m_b^2 & m_b^2 + m_3^2 - t_2 \\ s + s_2 - m_1^2 & s - m_a^2 + m_b^2 & 2s & s - s_1 + m_3^2 \\ s_2 - m_2^2 + m_3^2 & m_b^2 + m_3^2 - t_2 & s - s_1 + m_3^2 & 2m_3^2 \end{bmatrix}. \tag{2.38}$$

The limits of the physical region can be found from the requirements that $E_1^* \geq m_1$, $\sqrt{s_2} \geq m_2 + m_3$ and $-1 \leq \cos\theta_1^* \leq 1$. These requirements can be expressed in the following useful relations:

$$\begin{aligned} s_2^{\pm} =& s + m_1^2 - \frac{1}{2m_a^2}\left[\left(s + m_a^2 - m_b^2\right)\left(m_a^2 + m_1^2 - t_1\right)\right. \\ & \left. \mp \lambda^{1/2}\left(s, m_a^2, m_b^2\right)\lambda^{1/2}\left(t_1, m_a^2, m_1^2\right)\right] \end{aligned} \tag{2.39}$$

and

$$\begin{aligned} t_1^{\pm} =& m_a^2 + m_1^2 - \frac{1}{2s}\left[\left(s + m_a^2 - m_b^2\right)\left(s - s_2 + m_1^2\right)\right. \\ & \left. \mp \lambda^{1/2}\left(s, m_a^2, m_b^2\right)\lambda^{1/2}\left(s, s_2, m_1^2\right)\right]. \end{aligned} \tag{2.40}$$

These relations constrain the boundary of the physical region in the s_2-t_1 plane. Equation (2.39) is useful for plotting s_2 as a function of t_1, and the opposite for Equation (2.40). We have two more relations restricting the boundary of the physical region, which are

$$s_2 > \left(m_2 + m_3\right)^2 \tag{2.41}$$

and

$$s_2 < \left(\sqrt{s} - m_1\right)^2. \tag{2.42}$$

Looking back at Figure 2.5, it is clear where these boundaries come from. We must have that $s_2 > (m_2 + m_3)^2$ holds because of energy conservation in the process $s_2 \to 2, 3$. The other condition comes from energy conservation in the process of $a, b \to 1, s_2$.

The physical region in the t_1-s_2 plane can be depicted by a Chew-Low plot. A sketch of such a plot is shown in Figure 2.6. If we choose to plot s_2 as a function of t_1, the upper boundary is given by s_2^+. The lower boundary is determined by s_2^-, together with Equation (2.42). In some cases, the lower boundary will be completely determined by the latter.

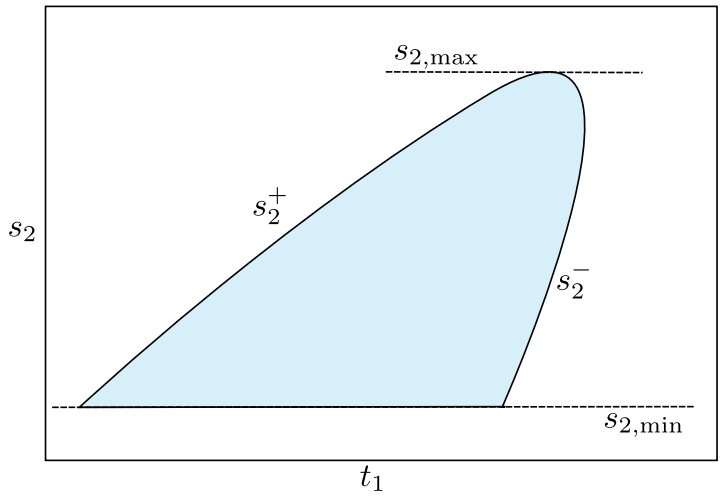

Figure 2.6: Chew-Low plot illustrating the allowed kinematical region in the t_1-s_2 plane. The minimum and maximum values of s_2 are indicated with dashed lines. The border is defined by $s_2^+(t_1)$ and $s_2^-(t_1)$.

The limit for t_2 can be found by inserting $\cos\theta_{b3}^{R23} = \pm 1$ into Equation (2.34), which gives

$$\begin{aligned} t_2^{\pm} =& m_b^2 + m_3^2 - \frac{1}{2s_2}\left(s_2 + m_b^2 - t_1\right)\left(s_2 + m_3^2 - m_2^2\right) \\ & \pm \frac{1}{2s_2}\lambda^{1/2}\left(s_2, m_b^2, t_1\right)\lambda^{1/2}\left(s_2, m_3^2, m_2^2\right). \end{aligned} \tag{2.43}$$

To find the limits for s_1 we solve Equation (2.35) for s_1 and insert $\cos\phi_b = \pm 1$

to get

$$\begin{aligned} s_1^{\pm} =& s + m_3^2 - \frac{1}{\lambda\left(s_2, t_1, m_b^2\right)} \\ & \times \Bigg(\det \begin{bmatrix} 2m_b^2 & s_2 - t_1 + m_b^2 & m_b^2 + m_3^2 - t_2 \\ s_2 - t_1 + m_b^2 & 2s_2 & s_2 - m_2^2 + m_3^2 \\ s - m_a^2 + m_b^2 & s + s_2 - m_1^2 & 0 \end{bmatrix} \\ & \mp 2 \left[G\left(s, t_1, s_2, m_a^2, m_b^2, m_1^2\right) G\left(s_2, t_2, m_3^2, t_1, m_b^2, m_2^2\right) \right]^{1/2} \Bigg), \end{aligned} \tag{2.44}$$

where G was defined in Equation (2.36). We have now presented all the relations needed for calculating the phase space integral for the $2 \to 3$ process of MCP bremsstrahlung.

Chapter 3

Millicharged particles[†]

MCPs are possible candidates in the search for DM. An MCP is a theoretical particle with an electric charge ϵe, where $\epsilon \ll 1$. The coupling strength of a particle with the SM photon is proportional to the charge of the particle. DM candidates have to interact weakly with the SM, otherwise they should already have been detected. An MCP will be weakly coupled to the SM photon with its coupling strength ratio compared to the electron given by ϵ, which makes it a promising candidate for DM.

A minimal MCP model is based on only two assumptions: that the MCP couples to the SM photon with a strength $Q_\chi = \epsilon$e and that it is stable [14]. The MCP has to be stable if Q_χ is the smallest non-zero charge in the dark sector because it would have no legal decay modes. By only making these two assumptions, the derived results are valid for any particle satisfying them, even if the particle turns out not to be DM. However, if the particle is part of stable DM, additional constraints apply, and it will probably make up only a small fraction of the relic DM in the universe [15].

The search for MCPs is being carried out in multiple ways. In recent years existing data from accelerator experiments have been reanalyzed due to the ongoing search for MCPs, and new MCP searches using neutrino experiments have been proposed [15]. Regions of the mass-charge space of possible MCPs have already been ruled out by a variety of constraints. For example, new, improved limits were recently set by the ArgoNeuT experiment at Fermilab, which is the first neutrino experiment dedicated to the search for MCPs [16].

[†]Adapted from [1].

The search for MCPs at SLAC has also ruled out regions of the mass-charge space [17]. Additionally, astrophysical constraints can be obtained from stellar evolution, or cosmological constraints from, e.g., the Big Bang nucleosynthesis limits [9]. MCPs have yet to be detected, but regions of the mass-charge space remain where the possibility of detection has not yet been ruled out [9].

From the lack of detection of particles with masses below the TeV scale, one can conclude that such particles have to be weakly coupled to the SM. Combined with the constraints on other DM candidates, the investigation of light DM particles with masses in the sub-GeV range has gained increasing interest during the last few years [8]. This is also because new research has demonstrated that such light particles might be accessible to direct detection experiments, unlike traditionally thought [8]. For example, a detectable energetic flux of DM can result from the decay of mesons produced in inelastic cosmic ray collisions [18]. An MCP with a mass in the sub-GeV range is thus a promising candidate for DM.

3.1 Cosmic ray production

This subsection is based on [8]. In parallel with the MCP detector searches, the possibility of detecting MCPs from cosmic ray interactions is being explored. Cosmic ray interactions in the atmosphere are a promising source of light DM. Mesons produced by the cosmic ray interactions might decay partially into MCPs, and if this is the case then the resulting MCP flux can be detected by underground detectors. One advantage of this method is that the cosmic ray interactions in the atmosphere depend only on the cosmic ray flux, which is known. Another advantage is that cosmic rays constitute a permanent MCP production source [14].

From the cosmic ray flux of undecayed mesons, one can calculate the resulting flux of exotic particles, as done by Kachelrieß and Tjemsland in [8]. In their article, the energy spectra of the light, neutral mesons $\pi^0, \eta, \rho^0, \omega, \phi$ and J/ψ were evaluated. This was done using the quantum chromodynamics (QCD) inspired event generators DPMjet [19], Sibyll [20], and Pythia [21]. DPMjet and Sibyll were chosen to describe $\pi^0, \eta, \rho^0, \omega$ and ϕ, because they are widely used in the field of cosmic ray physics. For J/ψ, DPMjet predicts a cross section that is too low. Because of this, Pythia was used to describe the J/ψ mesons. From the fluxes of undecayed mesons, the resulting flux of MCPs was calculated. The MCP fluxes for each meson were found from the integrated meson fluxes, scaled by the mesons BRs into MCPs. The BRs were found by rescaling the BRs of

meson decay modes into charged leptons. All the mesons have contributions from the direct decay into MCPs, whose BR was found by rescaling the dilepton decay BR. The mesons η, π^0, and ω have additional contributions from three-body decay modes. The results for MCPs found in [8] are reproduced in this thesis and can be found in Chapter 6.

3.2 MCP signal in experiments

The detection of MCPs in experiments such as the water Cherenkov detector SK is dominated by soft scattering from electrons [14]. Thus, the MCPs are observed as an excess of low-energy recoil electrons in the detector [22]. For the MCPs to be detected, they have to be sufficiently boosted so that they can kick an electron above the detection threshold [14]. The light signal from the electron-MCP scattering can be used to constrain the MCP flux to an energy range $T_{\min} < T < T_{\max}$, which gives a windowed cross section $\tilde{\sigma}_{e\chi}$ for the interactions [8]. As done in [14], this windowed cross section can be approximated as

$$\tilde{\sigma}_{e\chi}\left(\gamma_\chi\right) = \int_{q^2_{\min}}^{q^2_{\max}} \frac{\mathrm{d}\sigma_{e\chi}}{\mathrm{d}q^2}\, \mathrm{d}q^2 \approx \frac{2\pi\alpha^2\varepsilon^2}{2T_{\min}m_e}\left(1 - \frac{T_{\min}}{T_{\max}}\right)\Theta\left(\gamma_\chi - \gamma_{\text{cut}}\right), \tag{3.1}$$

where ϵ is the fractional charge of the MCP, m_e is the electron mass, α is the fine structure constant, q is the momentum transfer and γ_χ is the Lorentz factor of the MCP. We can find γ_{cut} from [14] as

$$\gamma_{\text{cut}} \approx 0.6\sqrt{2T_{\min}/m_e} + 0.4\sqrt{2T_{\max}/m_e}. \tag{3.2}$$

In the approximation used here, we assume a sharp limit between detected and non-detected MCPs at $\gamma = 6$, enforced by the Heaviside step function in Equation (3.1). The total number of electron-MCP scattering events $N_{e\chi}$ is then

$$\begin{aligned} N_{e\chi} &= N_e t \int_{\gamma_{\text{cut}}}^{\infty} \mathrm{d}\gamma_\chi \tilde{\sigma}_{e\chi}\left(\gamma_\chi\right) \frac{\mathrm{d}\Phi_\chi}{\mathrm{d}\gamma_\chi}\left(\gamma_\chi\right) \\ &\approx N_e t \frac{\pi\alpha^2\epsilon^2}{T_{\min}m_e}\left(1 - \frac{T_{\min}}{T_{\max}}\right)\Phi_{\text{cut}}\left(m_\chi\right), \end{aligned} \tag{3.3}$$

where N_e is the number of electrons in the fiducial volume of the detector, t is the data collection period, and Φ_χ is the total integrated MCP flux [14]. Here $\Phi_{\text{cut}}\left(m_\chi\right)$ is the integrated MCP flux for a Lorentz factor of γ_{cut}, which is

proportional to ϵ^{-2}. We can rewrite Equation (3.3) to get the fractional charge ϵ as a function of the MCP mass m_χ:

$$\epsilon = \left(\frac{N_{e\chi} T_{min} m_e}{N_e t \pi \alpha^2 (1 - T_{min}/T_{max})} \left(\tilde{\Phi}_{\text{cut}} (m_\chi) \right)^{-1} \right)^{\frac{1}{4}}, \tag{3.4}$$

where we defined $\tilde{\Phi}_{\text{cut}} (m_\chi) = \epsilon^{-2} \Phi_{\text{cut}} (m_\chi)$.

3.2.1 Super-Kamiokande

The SK detector is a water Cherenkov detector that searches for the light signal emitted by relativistically charged particles [8]. It detects scattered electrons from the Cherenkov radiation they emit in water [11]. The detector is located under approximately 1 km of rock [23].

Supernovae emit most of their energy in the form of neutrinos [24]. They happen rarely in our own galaxy, but there should still be a lot of neutrinos in existence from the supernova explosions throughout the history of the universe [24]. The signal from these relic neutrinos is often referred to as the supernova relic neutrino signal [24]. In [24], data from the SK detector was used to search for the supernova relic neutrino signal, resulting in upper limits for the neutrino flux.

The event shape of MCPs is similar to the event shape of the supernova background [8]. Thus, from the results from SK in [24], we find that cosmic ray MCPs can result in maximum 4 events per year with 90% CL [8]. This means that all MCP candidates with a mass and a charge that predict more than 4 detected events per year must be excluded. Knowing this, we can use Equation (3.4) to make an exclusion plot for MCPs in the mass-charge plane.

Before any results from the SK detector are extracted, all cuts are tuned and background signals are removed [24]. Optimization of the cuts has lowered the energy threshold to 16 MeV, and the upper limit is $T_{\text{max}} = 88$ MeV for the case of comparison with the supernova relic neutrinos [24]. Inserting these values into Equation (3.2) gives a Lorentz factor of $\gamma_{\text{cut}} \approx 6$ [14]. This means that only the MCPs with a Lorentz factor γ greater than 6 will have enough energy to be detected by SK.

The fiducial volume of SK is 22.5 kt of water [24]. The number of electrons in the detector N_e can be calculated using

$$N_e = 10 \frac{m}{M} N_A, \tag{3.5}$$

where m is the mass and M is the molar mass of water, and N_A is Avogadro's number. The factor of 10 comes from the fact that each water molecule has 10 electrons. The atomic weight of water is 18.016 g/mol [25]. Inserting our numbers into Equation (3.5) gives us a total number of $N_e = 7.52 \cdot 10^{33}$ electrons in the detector.

Chapter 4

Feynman rules for QED and application to MCPs[†]

4.1 Feynman rules for QED

The Feynman rules allow us to directly translate a Feynman diagram into a contribution to the amplitude $\mathcal{M}$. The Feynman rules used here follow the formulation in [26], which this section is based on. The QED Lagrangian reads

$$\mathcal{L} = \bar{\psi}(i\partial\!\!\!/ - m)\psi - \frac{1}{4}\left(F_{\mu\nu}\right)^2 - e\bar{\psi}\gamma^\mu\psi A_\mu - \frac{1}{2}\left(\partial_\mu A^\mu\right)^2 \tag{4.1}$$

in the Lorentz-invariant Feynman gauge. From this Lagrangian we can obtain the Feynman rules for QED. The free Lagrangian gives the propagators, while the interaction terms determine the vertex factor and thus the coupling constant which dictates the interaction strength.

The primitive QED vertex diagram is made up of two (anti)fermion lines and one photon line, as shown in Figure 4.1. Generally, straight lines with their arrow pointing in the direction of positive time represent fermions, while straight lines with their arrow pointing backward in time represent antifermions. Photons are denoted by wavy lines. All QED interactions consist of primitive vertices connected by propagators and external lines.

We use here the Feynman rules as expressed in the Feynman gauge. The Dirac propagator should be applied to all internal fermion lines, while the photon

[†]Adapted from [1].

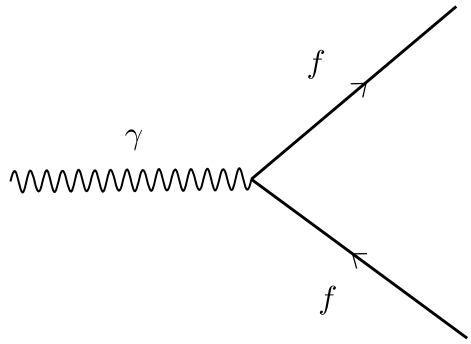

Figure 4.1: Feynman diagram of the primitive QED vertex. The photon γ is denoted by a wavy line, while the (anti)fermion f is denoted by a straight line.

propagator corresponds to an internal photon line. Each vertex gives a factor of $\mathrm{i}Q\mathrm{e}\gamma^\mu$, where for the electron $Q = 1$. All incoming or outgoing lines are denoted as described in Table 4.1, which gives a summary of the Feynman rules for QED.

Table 4.1: Feynman rules for QED.

Dirac propagator (internal fermion)	$\frac{\mathrm{i}(\not{p}+m)}{p^2-m^2+i\epsilon}$
Photon propagator (internal photon)	$\frac{-\mathrm{i}g_{\mu\nu}}{p^2+\mathrm{i}\epsilon}$
Vertex	$\mathrm{i}Q\mathrm{e}\gamma^\mu$
Initial, external fermion	$u^s(p)$
Final, external fermion	$\bar{u}^s(p)$
Initial, external antifermion	$\bar{v}^s(p)$
Final, external antifermion	$v^s(p)$
Initial, external photon	$\epsilon_\mu(p)$
Final, external photon	$\epsilon^*_\mu(p)$

4.1.1 Form factors

Form factors are functions that describe particle interactions without taking into account all of the physics that is involved. They can, e.g., be used to describe meson interactions, which in reality involve a complicated multitude of gluons and quark interactions. The form factor can be said to describe the structure of the meson, which is built up of one valence quark and one valence antiquark, together with a quark sea. Using the form factor, one can treat the meson as a point particle to simplify calculations.

4.1.2 Ward identity

This section gives a brief explanation of the Ward identity, based on Section 8.4 in [27]. We will need this identity for later calculations. A proof of the Ward identity is beyond the scope of this thesis, but can be found in, e.g., [27]. The Ward identity must hold because of Lorentz invariance and the fact that unitary representations for massless spin-1 particles, like the photon, have two polarizations. When calculating matrix elements in QED we will get terms like

$$\mathcal{M} = \epsilon^{\mu} M_{\mu}, \tag{4.2}$$

where M_μ transforms like a four-vector and ϵ^μ is the polarization vector. There are Lorentz transforms under which

$$\mathcal{M} \rightarrow \left(a_1 \epsilon_1^{\mu} + a_2 \epsilon_2^{\mu} + a_3 p^{\mu'} \right) M'_{\mu}, \tag{4.3}$$

where a_1, a_2, a_3 are constants. $\mathcal{M}$ can only be Lorentz invariant if $\mathcal{M} = \epsilon^{\mu'} M_{\mu'}$, where $\epsilon^{\mu'}$ is a linear combination of ϵ_1^μ and ϵ_2^μ. Thus, $\mathcal{M}$ can only be Lorentz invariant if

$$p^{\mu} M_{\mu} = 0, \tag{4.4}$$

which is known as the Ward identity.

4.1.3 Application to MCPs

The Feynman rules for QED can be applied to MCPs interacting with the SM through photons, but their charge has to be accounted for. For an MCP with a charge $Q_\chi = \epsilon e$, the value of Q in the vertex factor is ϵ. This gives the MCPs a weaker coupling to the photon than the coupling for SM fermions. A weaker coupling constant means a weaker interaction strength. The fact that MCPs

would interact weakly with the SM photons means there is a possibility that they exist despite them not having been detected yet.

The MCP χ has an antiparticle partner $\bar{\chi}$, and they play the roles corresponding to fermions and antifermions in QED. Thus, we can apply to them the Feynman rules in the same manner as we do for fermions. This allows for comparison of the MCP production compared to the production of leptons in, e.g., meson decays.

4.2 Meson branching ratios into MCPs

The BR of a meson decaying into MCPs can be found by rescaling its BR for electromagnetic decay into charged leptons. The BR of a decay is defined in Equation (2.6). The main contributions to the MCP production from meson decays come from the direct decay $m \to \chi\bar{\chi}$, the Dalitz decay $P \to \gamma\chi\bar{\chi}$, and the three-body decay $V \to \chi\bar{\chi}P$, where P is a pseudoscalar meson and V is a vector meson [8].

Detailed calculations of the rescaled BRs can be found in Appendix A. Here we will simply present the results. The rescaled BR for the direct decay is given by

$$\frac{\mathrm{BR}(m \to \bar{\chi}\chi)}{\mathrm{BR}\,(m \to l^+l^-)} = \epsilon^2 \sqrt{\frac{1 - 4m_\chi^2/m_m^2}{1 - 4m_l^2/m_m^2}} \left(\frac{1 + 2m_\chi^2/m_m^2}{1 + 2m_l^2/m_m^2} \right), \tag{4.5}$$

where l^+ and l^- are leptons, m_l is the lepton mass, m_χ is the MCP mass and m_m is the meson mass. The rescaled BR for the Dalitz decay is given by

$$\begin{aligned} \frac{\mathrm{BR}(P \to \gamma\bar{\chi}\chi)}{\mathrm{BR}(m \to \gamma\gamma)} =& \frac{2\alpha\varepsilon^2}{3\pi} \int_{4m_\chi^2}^{m_\mathrm{m}^2} \mathrm{d}q^2 \sqrt{1 - \frac{4m_\chi^2}{q^2}} \left(1 + 2\frac{m_\chi^2}{q^2} \right) \\ & \times \frac{1}{q^2} \left(1 - \frac{q^2}{m_m^2} \right)^3 \left| F_m\left(q^2\right) \right|^2, \end{aligned} \tag{4.6}$$

where $\left|F_m\left(q^2\right)\right|$ is the meson form factor and q is the momentum of the virtual photon [8].

We use the parametrizations for the form factors as given in [8]. The form factor used in Equation (4.6) can be approximated for π^0 as

$$F_{\pi^0}\left(q^2\right) \approx 1 + q^2 b_{\pi^0}, \tag{4.7}$$

with $b_{\pi^0} = (5.5 \pm 1.6)\,\mathrm{GeV}^{-2}$. For η, the form factor can be approximated as

$$F_\eta\left(q^2\right) \approx \left(1 - \frac{q^2}{\Lambda_\eta^2}\right)^{-1}, \tag{4.8}$$

with $\Lambda_\eta = (0.716 \pm 0.011)\,\mathrm{GeV}$.

With these expressions for the BRs of mesons decaying into MCPs, we can find the MCP flux resulting from the decays of cosmic ray mesons.

Chapter 5

Earth attenuation of MCPs

MCPs can approach the Earth from all directions, but due to the Earth's density they might not be able to reach an underground detector from all angles. Several articles, such as [8], assume that only downward-moving MCPs reach the detector. It is, however, interesting to investigate if upward-moving MCPs can also reach the detector with sufficient energy left to be detectable. Additionally, there is also a possibility that not all of the downward-moving MCPs reach the detector.

The flux of MCPs that reach an underground detector, as well as their energy spectrum, depends on the zenith angle of the incoming MCPs [28]. The more ground the MCPs have to travel through to reach the detector, the more energy they will lose. If the energy loss is substantial, their remaining energy might drop below the detection threshold and thus they will no longer be detectable [22].

The attenuation of a charged particle flux propagating through matter strongly depends on the charge-to-mass ratio of the particles, as can be seen from the comparison of electrons and muons propagating through matter [22]. A bigger charge increases the interaction strength. The incoming energy and zenith angle are also important parameters for investigating if an MCP is likely to be detected. Energetic MCPs are more likely to still have enough remaining energy when they reach the detector, while the zenith angle decides how much material the MCP has to traverse on its path toward the detector and thus the number of interactions.

To study the energy loss of MCPs traversing the Earth, we need to know the average number of interactions along the path toward the detector as well as the average energy loss per interaction. The average energy loss wil depend

on the energy, mass, and charge of the MCP, as well as the mass and charge of the other particle participating in the interaction. Since the MCP will lose some of its energy for each interaction, the energy loss for each interaction will vary along the path toward the detector.

A first approximation can be done by finding the average energy loss for the incoming MCP energy and assuming the energy loss remains the same value for all interactions. This means not taking into account the decreasing value of the incoming energy for each interaction. Then the energy loss per distance can be expressed as

$$\frac{\mathrm{d}E}{\mathrm{d}x} = n\sigma\langle y\rangle, \tag{5.1}$$

where E is the energy of the incoming MCP, x is the position along the path to the detector, n is the number density of the interacting particles, σ is the total cross section for the interaction in question, and $\langle y\rangle$ is the average energy loss per interaction. We can integrate over x to find the total energy lost along the path.

MCPs traversing the Earth lose energy due to electron-MCP scattering, scattering off nuclei, pair production, and bremsstrahlung [22]. We do not consider radiation losses due to scattering off electrons, as this process is suppressed by a factor of $1/Z^2$, where Z is the nuclear charge [22]. The processes of electron-MCP scattering, scattering off nuclei and bremsstrahlung will be treated separately in the following subsections.

5.1 Earth composition and density

To model the energy loss of MCPs traversing the Earth, we need some information about the Earth's composition and density. The inside of the Earth can be divided into three sections: the core, the mantle, and the crust. The border between the core and the mantle is at a radius of approximately 3473 km, while for the border between the mantle and the crust, the radius is approximately 6338 km [29].

To model the energy loss of MCPs due to scattering off nuclei, we need to know what nuclei the MCPs are interacting with. For this, we need data about the chemical composition of the Earth. We use the data given in [30], of which a summary is shown in Table 5.1. The continental crust makes up about 41% of the total crust [31]. For simplicity, we use this information to find the average density of the total crust from the data for the oceanic and the continental crust given in [30]. To find the energy loss due to scattering off electrons, we need

Table 5.1: Chemical composition of the layers of the Earth, given as percentages of the total mass. Data taken from [30]. The values for the crust are taken as the average values using the data for the oceanic and the continental crust. Only the most common elements are included, and empty fields correspond to approximately zero.

Element	Core	Mantle	Crust
O	3.00	44.12	45.53
Si	7.00	20.89	24.94
Mg		25.09	3.84
Al		1.24	8.42
Ca		1.49	6.64
Fe	80.00	6.53	6.92
Ni	4.65	0.17	0.18
S	4.00	0.01	

to know the average number of electrons a particle will pass by along its path through the Earth to reach the detector. For simplicity we assume the Earth to be a perfect sphere. We use the density profile for the Earth found in [32]:

$$\rho(r) = \begin{cases} 13.0885 - 8.8381x^2, & r < 1221.5 \\ 12.5815 - 1.2638x - 3.6426x^2 - 5.5281x^3, & 1221.5 < r < 3480 \\ 7.9565 - 6.4761x + 5.5283x^2 - 3.0807x^3, & 3480 < r < 5701 \\ 5.3197 - 1.4836x, & 5701 < r < 5771 \\ 11.2494 - 8.0298x, & 5771 < r < 5971 \\ 7.1089 - 3.8045x, & 5971 < r < 6151 \\ 2.691 + 0.6924x, & 6151 < r < 6346.6 \\ 2.9, & 6346.6 < r < 6356 \\ 2.6, & 6356 < r < 6368 \\ 1.02, & r \leq R_\oplus \end{cases}, \tag{5.2}$$

where r is the distance from the center of the Earth. Here x is a scaled, radial variable defined by $x \equiv r/R_\oplus$, where $R_\oplus = 6371\,\text{km}$ is the radius of the Earth [32]. The density ρ is measured in g/cm^3 and the distance r is measured in km. Figure 5.1 shows a plot of Equation (5.2). The plot illustrates how the density is higher closer to the core.

The geometry of our problem is sketched in Figure 5.2. To find the amount

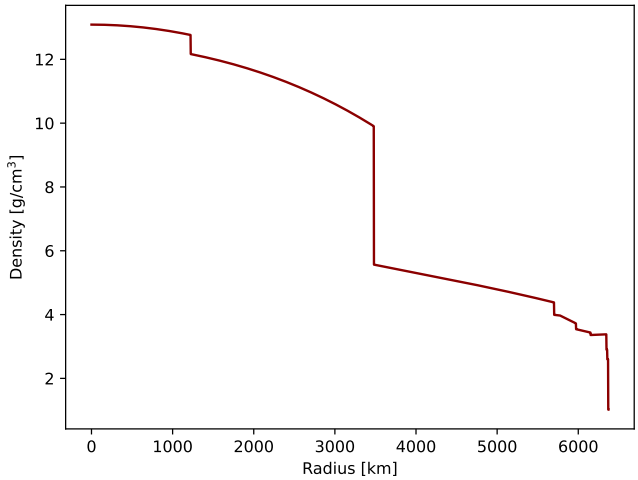

Figure 5.1: Earth's density plotted as a function of radius, using the density profile in [32].

of material traversed on a particle's path through the Earth toward the detector, we need an expression for the distance from the center of the Earth along a path with an incoming angle θ. From Figure 5.2 we see that this can be expressed as

$$r(x) = \sqrt{(R_\oplus - d)^2 + x^2 - 2\,(R_\oplus - d)\,x\cos\tau}, \tag{5.3}$$

where $\tau = \pi - \theta$ and x is the coordinate of the particle along its path toward the detector. An equivalent expression was found in [15]. The total path length for a particle incoming at an angle θ with respect to the detector can be expressed as

$$X = \sqrt{(d - R_\oplus)^2 \cos^2\tau - d\,(d - 2R_\oplus)} + (R_\oplus - d)\cos\tau. \tag{5.4}$$

To find the total mass traversed we integrate the density along the particle path using Equation (5.2) for each incoming angle θ:

$$m_{\text{tot}} = \int_0^X \rho(r(x))\mathrm{d}x. \tag{5.5}$$

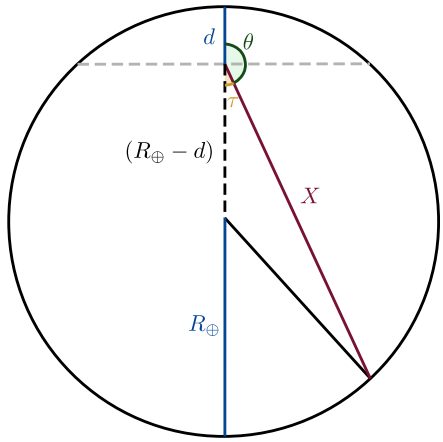

Figure 5.2: MCP path through Earth toward an underground detector at depth d. The MCP's total path length is denoted by X, and the radius of the Earth is denoted by $R_\oplus$. The angle θ is the incoming angle at the detector.

To find the number of electrons this m_{tot} corresponds to, we assume that the Earth contains an equal number of neutrons and protons. The number of electrons equals the number of protons. Thus, we can find the total number of electrons from

$$N_e = \frac{m_{\text{tot}}}{2m_p}, \tag{5.6}$$

where m_p is the proton mass.

5.2 Electron-MCP scattering

For an MCP with an incoming energy E_i scattering off another particle we define the variable

$$y = \frac{E_i - E_f}{E_i} \tag{5.7}$$

describing the MCP's fractional energy loss, where E_f is the MCP's energy after scattering. The average energy loss per interaction can be found from

$$\langle y \rangle = \frac{1}{\sigma} \int \frac{\mathrm{d}\sigma}{\mathrm{d}y} y \, \mathrm{d}y, \tag{5.8}$$

where σ is the total scattering cross section for the interaction in question.

MCPs traversing the Earth will lose energy through interactions with electrons. The Feynman diagram for electron-MCP scattering is shown in Figure 5.3. To be able to find the average energy loss per interaction, given by Equation (5.8), we have to find $\frac{\mathrm{d}\sigma_{\chi\mathrm{e}}}{\mathrm{d}y}$. To do this we use that

$$\frac{\mathrm{d}\sigma_{\chi\mathrm{e}}}{\mathrm{d}y} = \frac{\mathrm{d}\sigma_{\chi\mathrm{e}}}{\mathrm{d}\theta_\chi}\frac{\mathrm{d}\theta_\chi}{\mathrm{d}y}, \tag{5.9}$$

where $\frac{\mathrm{d}\sigma_{\chi\mathrm{e}}}{\mathrm{d}\theta_\chi}$ is the differential cross section for electron-MCP scattering in the lab frame. We use the expression given in [22], where

$$\begin{aligned}\frac{d\sigma_{\chi e}}{d\theta_\chi} &= \frac{2}{\pi}\sin\theta_\chi \frac{\epsilon^2 r_e^2 m_e |\mathbf{p_1}|}{E_2|\mathbf{p_a}|} \\ &\times \frac{m_e^2\left(E_a^2+E_1^2\right)+\frac{1}{2}\left(m_e^2+m_\chi^2\right)\left(2m_\chi^2-2\left(p_a\cdot p_1\right)\right)}{\left(2m_\chi^2-2\left(p_a\cdot p_1\right)\right)^2},\end{aligned} \tag{5.10}$$

with the symbols defined as shown in Figure 5.3, and where r_e is the classical radius of the electron given by $r_e = \alpha/m_e$ [22].

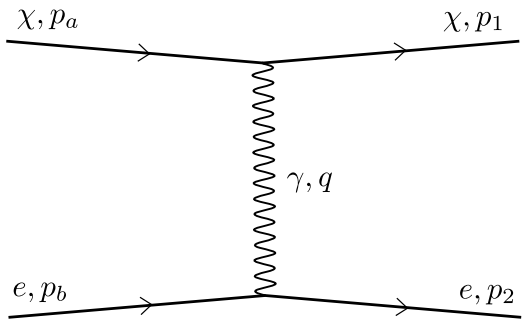

Figure 5.3: Feynman diagram of MCP-electron scattering. The incoming and outgoing MCPs are denoted by a and 1, respectively, while the incoming and outgoing electrons are denoted by b and 2.

Figure 5.4 shows an illustration of MCP-electron scattering in the rest frame of the electron. The subscripts a and 1 refer to the incoming and outgoing

MCPs, respectively, while the subscripts b and 2 refer to the incoming and outgoing electrons. By using the equation for the Mandelstam variable t as given in Equation (2.20) in the lab frame, where p_b is at rest, we can write

$$\begin{aligned} \left(p_a - p_1\right)^2 &= \left(p_b - p_2\right)^2 \\ 2m_\chi^2 - 2\left(E_a E_1 - |\mathbf{p_a}||\mathbf{p_1}|\cos\theta_\chi\right) &= 2m_e^2 - 2E_b E_2, \end{aligned} \tag{5.11}$$

which we rewrite to find an expression for the lab-frame scattering angle θ_χ:

$$\cos\theta_\chi = \frac{m_e^2 - m_\chi^2 + E_a E_1 - E_b E_2}{|\mathbf{p_a}||\mathbf{p_1}|}. \tag{5.12}$$

We would like to express everything in terms of y, E_a, m_e, and m_χ. Since the initial electron is at rest, we have that $|\mathbf{p_b}| = 0$, which gives that $E_b = m_e$. Using our definition of y in Equation (5.7), the outgoing MCP energy can be expressed as $E_1 = E_a(1-y)$. From energy conservation, we have that $E_a + E_b = E_1 + E_2$, and thus we can express the energy of the outgoing electron as $E_2 = m_e + E_a y$. The absolute value of the incoming MCP momentum is given by $|\mathbf{p_a}| = \sqrt{E_a^2 - m_\chi^2}$. In the same way, using that $E_1 = E_a(1-y)$, we can express the absolute value of the outgoing MCP momentum as $|\mathbf{p_1}| = \sqrt{E_a^2(1-y)^2 - m_\chi^2}$. Inserting these substitutions into Equation (5.12) we get

$$\cos\theta_\chi = \frac{E^2(1-y) - m_\chi^2 - m_e E y}{\sqrt{E^2 - m_\chi^2}\sqrt{E^2(1-y)^2 - m_\chi^2}}, \tag{5.13}$$

where we have renamed E_a to E for simplicity.

By substituting in the same way for Equation (5.10), we end up with

$$\begin{aligned} \frac{\mathrm{d}\sigma_{\chi\mathrm{e}}}{\mathrm{d}\theta_\chi} =& \frac{\epsilon^2 r_e^2 \sin\theta_\chi}{2\pi} \\ &\times \frac{\sqrt{E^2(1-y)^2 - m_\chi^2}\, m_e^2\left(E^2 + E^2\left(1-y\right)^2\right) + E m_e\left(m_\chi^2 + m_e^2\right) y}{2E^3\sqrt{E^2 - m_\chi^2}\, m_e \pi (1-y) y^2}, \end{aligned} \tag{5.14}$$

where

$$\sin\theta_\chi = \sqrt{1 - \frac{\left(E^2(1-y) - m_\chi^2 - m_e E y\right)^2}{(E^2 - m_\chi^2)(E^2(1-y)^2 - m_\chi^2)}}. \tag{5.15}$$

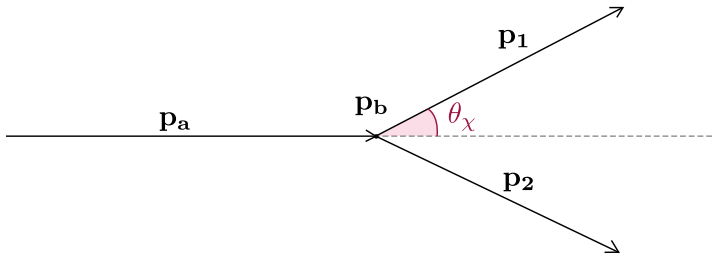

Figure 5.4: $2 \to 2$ scattering in the lab frame, where $\mathbf{p_b}$ is zero. The deflection angle is denoted by θ_χ. Arrow lengths and angles are not to scale.

We can find $\frac{\mathrm{d}\theta_\chi}{\mathrm{d}y}$ from solving Equation (5.13) for θ_χ and differentiating with respect to y:

$$\begin{aligned}\frac{\mathrm{d}\theta_\chi}{\mathrm{d}y} =& \frac{1}{\sin\theta_\chi} \frac{1}{\sqrt{E^2 - m_\chi^2}\sqrt{E^2(1-y)^2 - m_\chi^2}} \\ &\times \left[-\left(E^2 + Em_e\right) + \frac{E^2(1-y)(E^2(1-y) - m_\chi^2 - m_e E y)}{E^2(1-y)^2 - m_\chi^2} \right].\end{aligned} \tag{5.16}$$

Now inserting Equations (5.14) and (5.16) into Equation (5.9) gives

$$\begin{aligned}\frac{\mathrm{d}\sigma_{\chi\mathrm{e}}}{\mathrm{d}y} =& \frac{\epsilon^2 r_e^2 \left(m_\chi^2 m_e + E^2 m_e (y-1) + E m_\chi^2 y\right)}{2\pi E \left(E^2 - m_\chi^2\right)\left(E^2(y-1)^2 - m_\chi^2\right)(y-1)y^2} \\ &\times \left[\left(m_\chi^2 + m_e^2\right) y + E m_e \left(2 - 2y + y^2\right)\right],\end{aligned} \tag{5.17}$$

where the factors of $\sin\theta_\chi$ have canceled each other out.

For $m_\chi < m_e$ the maximum value of y is given by

$$y_{\max} = \frac{E - m_\chi}{E}, \tag{5.18}$$

which corresponds to the MCP transferring all of its kinetic energy to the electron. An additional constraint on y comes from Equation (5.13), where we must have that $\cos\theta_\chi \in [-1, 1]$.

For $m_\chi > m_e$, the lab frame scattering angle is limited by a maximum value of $\theta_{\chi,\max} = \arcsin\left(m_e/m_\chi\right)$ [33]. The corresponding upper limit for y can be

found from inserting $\theta_{\chi,\max}$ into Equation (5.13) and solving for y, giving

$$\begin{aligned} y_{\max} = &\Big[2\left(E\left(E^2-m_\chi^2\right)\cos^2\theta_{\max} - E^3 - E^2 m_e + E m_\chi^2 + m_e m_\chi^2\right) \\ &+ \left(E^2-m_\chi^2\right)\cos\theta_{\max}\sqrt{2\left(2m_e^2 - m_\chi^2 + m_\chi^2\cos 2\theta_{\max}\right)}\Big] \\ &\times \left[2E\left(\left(E^2-m_\chi^2\right)\cos^2\theta_{\max} - \left(E+m_e\right)^2\right)\right]^{-1}. \end{aligned} \tag{5.19}$$

The lower limit for y is $y_{\min} = \frac{\alpha^2}{2} m_e$, and it comes from the fact that the energy of the initial electron is below its mass due to the binding energy $-\alpha^2 m_e/2$ [22].

The total scattering cross section $\sigma_{\chi \mathrm{e}}$ can be found by integrating Equation (5.17) over y. To find the average energy loss per interaction we can then use Equation (5.8) together with Equation (5.17) and the result for $\sigma_{\chi \mathrm{e}}$. When this is done we can use Equation (5.1) together with the total number of electrons along an MCP's path to find how much of its energy is left when it reaches an underground detector.

5.3 Nucleus-MCP scattering

In the same way as for MCP-electron scattering, the MCPs can also lose energy from interactions with nuclei on their path through the Earth. The Feynman diagram for MCP-nucleus scattering is shown in Figure 5.5. We can use the same method as was described for electron-MCP energy loss for the case of nucleus-MCP scattering, just changing the differential cross section. We can reuse the expression for $\frac{\mathrm{d}\theta_\chi}{\mathrm{d}y}$ in Equation (5.16). Since the MCP mass does not exceed the nucleus mass, the maximum value of y is given by Equation (5.18), with the additional constraint that $\cos\theta_\chi \in [-1, 1]$ in Equation (5.13).

The differential scattering cross section for an MCP scattering off a nucleus is given by

$$\frac{d\sigma_{Z\chi}}{d\theta_\chi} = \frac{Z^2\epsilon^2 r_e^2 m_e^2}{4E_a^2\beta_\chi^2} \frac{1-\beta_\chi^2\sin^2\left(\frac{\theta_\chi}{2}\right)}{\sin^2\left(\frac{\theta_\chi}{2}\right) + 1/\left(2ap_a\right)^2} 2\pi\sin\theta_\chi, \tag{5.20}$$

where Z is the nuclear charge, $a \simeq 111 Z^{-1/3}/m_e$ is a screening parameter and β_χ is the velocity of the MCP [22]. We can rewrite this expression in terms of

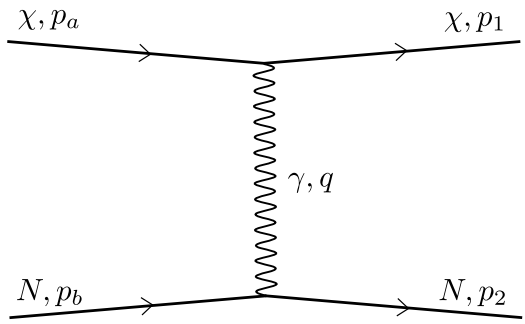

Figure 5.5: Feynman diagram of MCP-nucleus scattering. The incoming and outgoing MCPs are denoted by a and 1, respectively, while the incoming and outgoing nuclei are denoted by b and 2.

y, E, m_χ, and m_e in the same manner as we did for Equation (5.9). Doing this gives

$$\begin{aligned}\frac{d\sigma_{Z\chi}}{d\theta_\chi} =& \frac{-\epsilon^2 m_e^2 \pi r_e^2 Z^2}{2E^2(1-\frac{m_\chi^2}{E^2})} \sin\theta_\chi \left[1 - \left(1 - \frac{m_\chi^2}{E^2}\right) R^2\right] \\ & \times \left[\frac{1}{4a^2(E^2 - m_\chi^2) + R^2}\right]^{-1},\end{aligned} \tag{5.21}$$

where we have defined

$$R = \frac{1}{\sqrt{2}} \sqrt{1 - \frac{E^2(1-y) - m_\chi^2 - Eym_e}{\sqrt{E^2 - m_\chi^2}\sqrt{E^2(1-y)^2 - m_\chi^2}}}. \tag{5.22}$$

For the nucleus-photon interaction, we use the vertex factor given in [22]:

$$ieZF\left(-q^2\right)\gamma_\mu, \tag{5.23}$$

where $F\left(-q^2\right)$ is a form factor. This form factor can be written as

$$F(t) = \frac{a^2 t}{(1 + a^2 t)} \frac{1}{(1 + t/d)}, \tag{5.24}$$

where $t = -q^2$ and $d = 0.164 A^{-2/3}\,\mathrm{GeV}^2$ with A as the atomic number [22]. The form factor allows us to treat the nucleus as a point particle, and it scales

the charge of the nucleus according to the momentum transfer q. It acts as an extra factor in the amplitude of the nucleus-MCP interaction, and thus it will play the same role in the differential cross section. We take this into account by multiplying the differential cross section $\frac{\mathrm{d}\sigma_{Z\chi}}{\mathrm{d}y}$ with the form factor squared in our calculations.

Multiplying Equations (5.16) and (5.21) together with the form factor squared gives our final expression for the differential cross section:

$$\begin{aligned}\frac{\mathrm{d}\sigma_{Z\chi}}{\mathrm{d}y} =& \frac{a^2\epsilon^2 m_e^2 \pi r_e^2 Z^2}{E(E^2-m_\chi^2)} F^2(t)\left[m_\chi^2 m_N + E^2 m_N(y-1) + E m_\chi^2 y\right] \\ &\times \Bigg[- m_\chi^2(m_\chi^2 + \sqrt{E^2-m_\chi^2}\sqrt{E^2(1-y)^2-m_\chi^2}) \\ &- E^2(\sqrt{E^2-m_\chi^2}\sqrt{E^2(1-y)^2-m_\chi^2} + m_\chi^2(y-2)) \\ &+ E^4(y-1) + E^3 m_N y - E m_\chi^2 m_N y\Bigg] \\ &\times \left[\left(m_\chi^2 - E^2(y-1)^2\right)^2\left(1+4a^2\left(E^2-m_\chi^2\right)R^2\right)\right]^{-1}.\end{aligned} \tag{5.25}$$

Now that $\frac{\mathrm{d}\sigma_{Z\chi}}{\mathrm{d}y}$ is known, we can find the total energy loss due to scattering off nuclei using Equation (5.1). The total cross section $\sigma_{Z\chi}$ can be found from numerical integration of $\frac{\mathrm{d}\sigma_{Z\chi}}{\mathrm{d}y}$ over y.

The density of nuclei in the Earth can be found using the density profile of the Earth in Equation (5.2) together with the information about the Earth's composition in Table 5.1. We find the total number of protons along a path in the same way as we did for electrons. Then we use the composition data to find how many nuclei of a given element this corresponds to. We can then find how much of an MCP's energy is lost due to scattering off nuclei on its way toward an underground detector by inserting into Equation (5.1).

5.4 Bremsstrahlung

In addition to scattering off electrons and nuclei, MCPs also lose energy due to bremsstrahlung. The energy loss of MCPs due to bremsstrahlung scales as $\epsilon^4 E_a/m_\chi^2$, meaning the energy loss is more effective for lighter MCPs [22]. The Feynman diagrams for these processes are illustrated in Figure 5.6. The

energy loss calculations now become much more complicated due to the three-particle final states. However, we can still use Equation (5.8) to find the average energy loss per interaction. Now we do not have a given expression for the differential cross section, so we have to start from the beginning by calculating the amplitude for the process, and then performing the phase space integral using Equation (2.37). We will name the particles as shown in Figure 5.6, meaning a refers to the incoming MCP and 1 is the outgoing MCP.

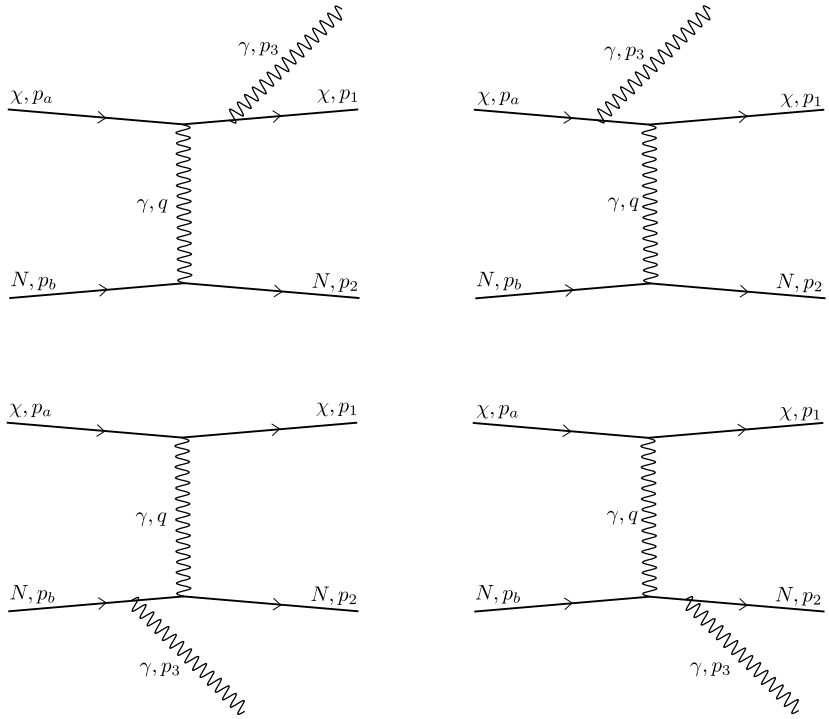

Figure 5.6: Feynman diagrams for Bremsstrahlung. The incoming and outgoing MCPs are denoted by a and 1, respectively, while the incoming and outgoing nuclei are denoted by b and 2. The outgoing photon is denoted by 3, while q is the momentum of the virtual photon.

We want to find the fractional energy loss using Equation (5.1), and thus we need to find the average energy loss per interaction $\langle y \rangle$. To do this we first have

to find $\frac{\mathrm{d}\sigma_{\mathrm{brems}}}{\mathrm{d}y}$. We will start from an expression for the total cross section σ_{brems}, and we factorize the $2 \to 3$ scattering process to a $2 \to 2$ scattering followed by a $1 \to 2$ decay as shown in Figure 5.7 and explained in Section 2.3.2. Inserting Equation (2.37) for the phase space factor into Equation (2.18) and including the form factor for the nucleus-photon vertex, we get

$$\begin{aligned}\sigma_{\mathrm{brems}} =& \frac{1}{64(2\pi)^4 \lambda\left(s, m_\chi^2, m_N^2\right)} \\ &\times \iiiint \frac{|\mathcal{M}|^2 F^2(t_{b2})}{(-\Delta_4)^{1/2}} \mathrm{d}s_1 \mathrm{d}t_2 \mathrm{d}t_1 \mathrm{d}s_2,\end{aligned} \tag{5.26}$$

where $F(t_{b2})$ is the form factor defined in Equation (5.24), t_{b2} is the invariant defined in Equation (2.23), and we used Equation (2.19) to simplify the denominator.

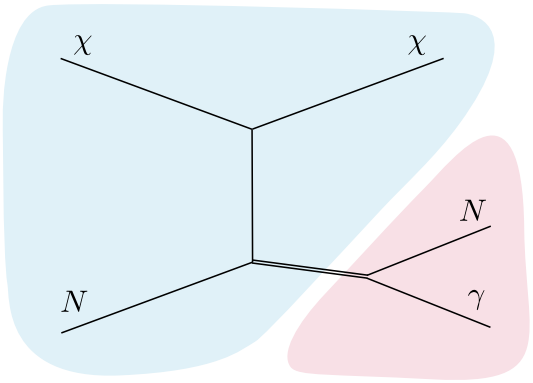

Figure 5.7: Illustration of the kinematic process of Bremsstrahlung factorized into a $2 \to 2$ scattering followed by a $1 \to 2$ decay. The photon is denoted by γ, the MCP is denoted by χ and N refers to a nucleus.

Because we want to find $\frac{\mathrm{d}\sigma_{\mathrm{brems}}}{\mathrm{d}y}$, we need to perform a change of variables to incorporate the variable y. To do this, we start by rewriting the invariant variable s_2 defined in Equation (2.22). In the lab frame, we have that

$$s_2 = 2m_\chi^2 + m_N^2 + 2E_a E_b - 2E_a E_1 + 2|\mathbf{p_a}||\mathbf{p_1}| \cos\theta_{a1} + 2E_b E_1, \tag{5.27}$$

where θ_{a1} is the angle between $\mathbf{p_a}$ and $\mathbf{p_1}$, and where we have inserted $|\mathbf{p_b}| = 0$. Rewriting this expression using the definition of the variable y in Equation (5.7)

we get

$$\begin{aligned} s_2 =& 2m_\chi^2 + m_N^2 - 2E^2(1-y) + 2Em_N y \\ &+ 2\sqrt{E^2 - m_\chi^2}\sqrt{E^2(1-y)^2 - m_\chi^2}\cos\theta_{a1}, \end{aligned} \tag{5.28}$$

where we have renamed E_a to E for simplicity. We now have an expression for s_2 as a function of y, but we introduced an additional variable θ_{a1}.

We can also rewrite the expression for t_1 from Equation (2.22) in terms of y and θ_{a1}. Again we start by writing out the expression in the lab frame, giving

$$t_1 = 2m_\chi^2 - 2\left(E_a E_1 - |\mathbf{p_a}||\mathbf{p_1}|\cos\theta_{a1}\right), \tag{5.29}$$

which we can again rewrite using the definition of y. Doing this gives

$$t_1 = 2m_\chi^2 - 2E^2(1-y) + 2\sqrt{E^2 - m_\chi^2}\sqrt{E^2(1-y)^2 - m_\chi^2}\cos\theta_{a1}. \tag{5.30}$$

Now we have two functions $s_2(y, \theta_{a1})$ and $t_1(y, \theta_{a1})$ which allow us to change variables in the integral in Equation (5.26) from s_1, t_2, t_1, and s_2, to s_1, t_2, θ_{a1}, and y. When performing the change of variables Equation (5.26) becomes

$$\begin{aligned} \sigma =& \frac{1}{64(2\pi)^4\lambda(s, m_\chi^2, m_N^2)} \\ &\times \iiint J \frac{|\mathcal{M}|^2 F^2(t_{b2})}{(-\Delta_4)^{1/2}} \mathrm{d}s_1 \mathrm{d}t_2 \mathrm{d}\theta_{a1} \mathrm{d}y, \end{aligned} \tag{5.31}$$

where J is the Jacobian and we insert Equations (5.28) and (5.30) for s_2 and t_1 in the integrand. The Jacobian is given by

$$J = \det \begin{bmatrix} 1 & 0 & 0 & 0 \\ 0 & 1 & 0 & 0 \\ 0 & 0 & \frac{\partial t_1}{\partial \theta_{a1}} & \frac{\partial t_1}{\partial y} \\ 0 & 0 & \frac{\partial s_2}{\partial \theta_{a1}} & \frac{\partial s_2}{\partial y} \end{bmatrix}. \tag{5.32}$$

To find an explicit expression for the Jacobian, we find $\frac{\partial t_1}{\partial \theta_{a1}}$ and $\frac{\partial t_1}{\partial y}$ by differentiating Equation (5.30) with respect to θ_{a1} and y, which gives

$$\frac{\partial t_1}{\partial \theta_{a1}} = -2\sqrt{E^2 - m_\chi^2}\sqrt{E^2(1-y)^2 - m_\chi^2}\sin\theta_{a1} \tag{5.33}$$

and

$$\frac{\partial t_1}{\partial y} = 2E^2 - \frac{2E^2\sqrt{E^2 - m_\chi^2}(1-y)\cos\theta_{a1}}{\sqrt{E^2(1-y)^2 - m_\chi^2}}. \tag{5.34}$$

In the same way we find $\frac{\partial s_2}{\partial \theta_{a1}}$ and $\frac{\partial s_2}{\partial y}$ from Equation (5.28), giving

$$\frac{\partial s_2}{\partial \theta_{a1}} = -2\sqrt{E^2 - m_\chi^2}\sqrt{E^2(1-y)^2 - m_\chi^2}\sin\theta_{a1} \tag{5.35}$$

and

$$\frac{\partial s_2}{\partial y} = 2E^2 + 2Em_N - \frac{2E^2\sqrt{E^2 - m_\chi^2}(1-y)\cos\theta_{a1}}{\sqrt{E^2(1-y)^2 - m_\chi^2}}. \tag{5.36}$$

Now we can insert our results into Equation (5.32), and after some simplification we get the following expression for the Jacobian:

$$J = 4Em_N\sqrt{E^2 - m_\chi^2}\sqrt{E^2(y-1)^2 - m_\chi^2}\sin\theta_{a1}. \tag{5.37}$$

Since we would like to find $\frac{\mathrm{d}\sigma_{\mathrm{brems}}}{\mathrm{d}y}$, we rewrite Equation (5.31) as

$$\begin{aligned}\frac{\mathrm{d}\sigma_{\mathrm{brems}}}{\mathrm{d}y} =& \frac{1}{64(2\pi)^4\lambda\left(s, m_\chi^2, m_N^2\right)} \\ &\times \iiint J\frac{|\mathcal{M}|^2F^2(t_{b2})}{(-\Delta_4)^{1/2}}\mathrm{d}s_1\mathrm{d}t_2\mathrm{d}\theta_{a1},\end{aligned} \tag{5.38}$$

where we can use Equations (5.28) and (5.30) to insert for s_2 and t_1 in the integrand. The invariant t_{b2} can be written in terms of our new variables as

$$t_{b2} = m_\chi^2 + 2m_N^2 - t_2 - 2Em_N y + \sqrt{E^2 - m_\chi^2}\sqrt{E^2(1-y)^2 - m_\chi^2}\cos\theta_{a1}. \tag{5.39}$$

We want to find the fractional energy loss due to bremsstrahlung for an MCP passing through the Earth toward an underground detector. To do this we use Equation (5.1) and the definition of $\langle y\rangle$ in Equation (5.8) to write

$$\frac{\mathrm{d}E}{\mathrm{d}x} = n_N\int y\frac{\mathrm{d}\sigma_{\mathrm{brems}}}{\mathrm{d}y}\mathrm{d}y, \tag{5.40}$$

which does not depend on the total cross section explicitly.

Figure 5.8 depicts the region of integration in the t_1-s_2 plane. The borders are given by Equations (2.39) and (2.40) We can find the corresponding curve in the θ_{a1}-y plane by inserting our expressions for $s_2(y, \theta_{a1})$ and $t_1(y, \theta_{a1})$ in Equation (2.40). Solving for y gives an upper limit of $y_{\max} = (E - m_\chi)/E$, as expected. Solving for θ_{a1} gives a lower limit of 0 and an upper limit of π, also as expected since we do not have any additional limits to θ_{a1} like we did in some

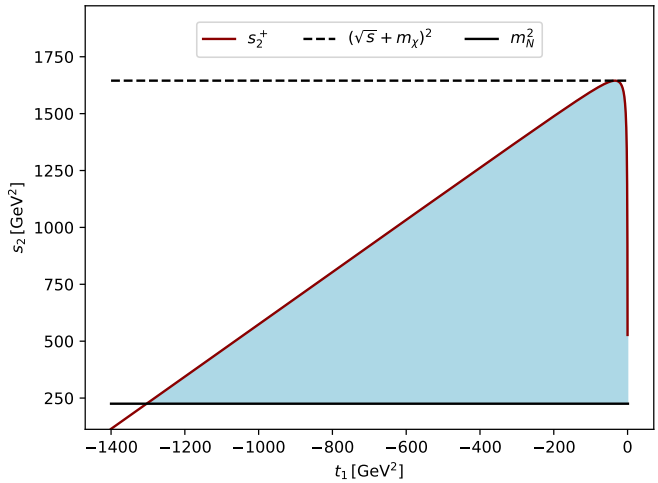

Figure 5.8: Chew-low plot, depicting the allowed kinematical region in the t_1-s_2 plane. The allowed region is shaded blue, while the solid lines correspond to the boundary. In this example we use the values $m_\chi = 1\,\mathrm{GeV}$, $Z = 8$, and $E_a = 50 m_\chi$.

cases for the MCP electron interaction described in Section 5.2. The limits for s_1 and t_2 are given by Equations (2.43) and (2.44), respectively.

We can now insert our expression for $\frac{\mathrm{d}\sigma_{\mathrm{brems}}}{\mathrm{d}y}$ into Equation (5.40) to find the average energy loss per distance. The number of nuclei encountered along a path toward the detector N_N can be calculated as described in Section 5.3. The squared amplitude can be calculated using the CalcHEP package [34], which is a package for calculating Feynman diagrams and cross sections. We should then be able to calculate how much energy an MCP will lose due to bremsstrahlung on its way toward an underground detector.

Chapter 6

Results

In this section we present our results. We start by reproducing some of the results found by Kachelrieß and Tjemsland in [8], using their cosmic ray fluxes of the π^0, η, ρ^0, ω, ϕ and J/ψ mesons to find the resulting integrated flux of MCPs. We find both the total MCP flux, and the flux counting only the MCPs with $\gamma > 6$. From the latter we construct an exclusion plot in the MCP mass-charge plane using the results from SK presented in Section 3.2.1. We then investigate the attenuation of MCPs traveling through the Earth to see if they will make it to the detector without their energy dropping below the detection threshold. We find the energy fraction that is left for MCPs of different charges and masses as a function of their incoming angles at the detector. The attenuation due to scattering off electrons and nuclei are treated separately, before looking at the total attenuation from both processes added together. For the attenuation by bremsstrahlung we encounter numerical problems, and we investigate the possible causes of these issues.

6.1 Total MCP flux[†]

From the flux of different mesons as a function of their energies per mass, the resulting integrated flux of MCPs is calculated. The mesons $\pi^0, \eta, \rho^0, \omega, \phi,$ and J/ψ are investigated. All of them have contributions from their direct decay into MCPs. In addition, π^0 and η also have contributions from the Dalitz decay. The three-body decay $\omega \to \pi^0 \bar{\chi}\chi$, which was included in [8], is not taken into

[†]Adapted from [1].

account here. The BRs are calculated using Equations (4.5) and (4.6), for which the known BRs for the dilepton and diphoton decays were found in [10]. For the dilepton BR, muons are used for comparison for all mesons except π^0, for which the electron is used. The meson form factors were taken into account using the parametrizations in Section 4.2.

The meson flux is integrated over E/m_m, where m_m is the meson mass. We perform our integrations using the SciPy function for Simpson's method**. The integrated MCP flux resulting from a given decay of a given meson is calculated by multiplying the integrated meson flux with the BR for the decay in question. A factor of 2 is added to take into account the fact that one meson produces two MCPs.

The total MCP flux resulting from the meson decays is plotted in Figure 6.1 separately for each meson and for each event generator. In [8], the meson flux data for J/ψ is from Pythia only, while the other meson fluxes were calculated using both DPMjet and Sibyll. The black lines show the total MCP fluxes from all mesons added together, with separate linestyles for the three different event generators. The step-like shape is due to the cutoffs at $m_\chi = m_m/2$. Decays with m_χ larger than this are not possible due to energy conservation.

The integrated MCP flux resulting solely from the direct decays and only using the meson flux from DPMjet is plotted together with the corresponding results from [8] in Figure 6.2. From the figure we see that the integrated MCP flux calculated here is slightly larger than the one found in [8]. This is because [8] did not include the helium flux, which means the meson fluxes used in their calculations were slightly different from the ones we used*.

The fluxes from π^0 and η are larger in Figure 6.1 than in Figure 6.2, and they also have a smoother shape. Both are due to their contribution from the Dalitz decay.

6.2 MCP flux above $\gamma = 6$†

The cutoff at the Super-Kamiokande experiment in their search for relic supernova neutrinos corresponds to a cutoff at the Lorentz factor $\gamma_\chi = E/m_\chi = 6$ [8], as described in Section 3.2. This means that only the MCPs with $\gamma > 6$ would be detected in the experiment. To find the integrated MCP flux above $\gamma = 6$, the meson flux is for each energy multiplied with its average number of

**https://docs.scipy.org/doc/scipy/reference/generated/scipy.integrate.simpson.html

*Private correspondence with Jonas Tjemsland.

†Adapted from [1].

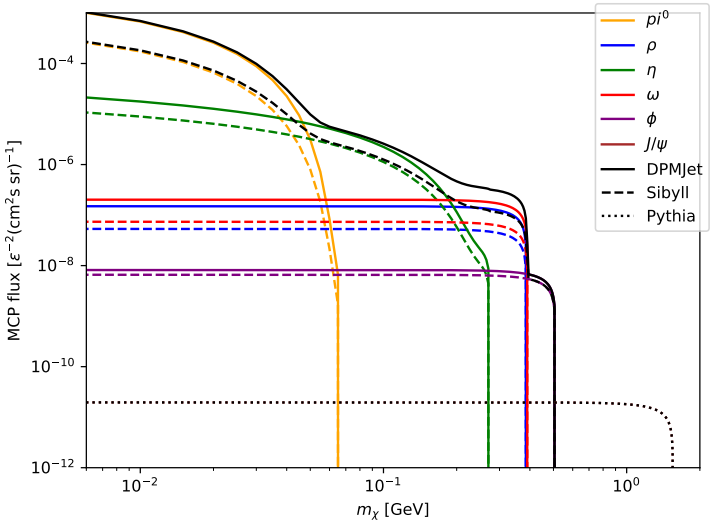

Figure 6.1: Integrated MCP flux resulting from the decays of the $\pi^0, \eta, \rho^0, \omega, \phi$, and J/ψ mesons. The solid lines use the meson fluxes calculated using DPMjet, while the dashed lines use Sibyll and the dotted line uses Pythia. The black lines show the total MCP flux from all mesons.

detectable MCPs produced. The MCPs are considered to be detected if they have $\gamma > 6$ and they are moving toward the detector. Then the meson flux is integrated, and the MCP flux is calculated in the same manner as described in the previous section.

To calculate how many MCPs would have $\gamma > 6$, the `phasespace` package [35] for Python was used. This package runs a Monte Carlo simulation using the method described in [36]. The function for generating decays takes the mass of the decaying particle and the masses of the decay products as inputs. If not specified, the matrix element is assumed to be constant. We will use this assumption in our calculations. The function returns the momentum four-vectors of the decay products and their associated weights. The weights give the probabilities for the different kinematical states to occur. A meson of higher energy has more available kinematical states to decay into. This is taken into account by scaling the importance of each event by its weight.

The phasespace package is used to calculate how many detectable MCPs of a given mass are produced on average for a given meson of a given momentum. 5000 simulations are run, and the MCPs are counted only if they have $\gamma > 6$

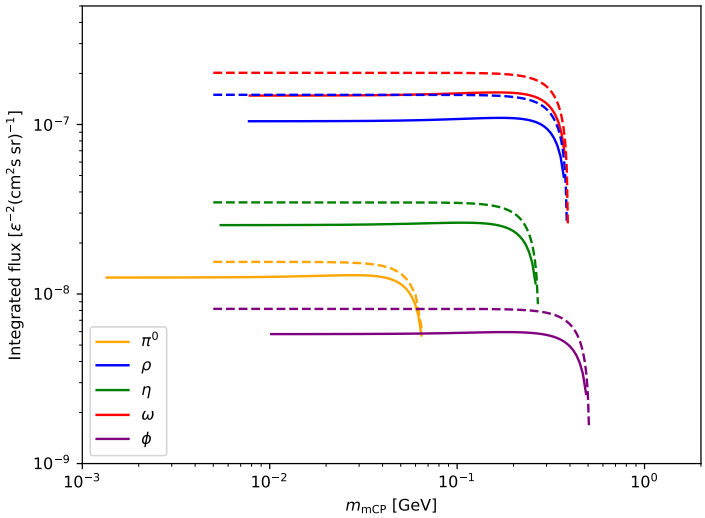

Figure 6.2: Integrated MCP flux from the direct meson decay into two MCPs calculated from the DPMJET meson flux found in [8]. The dashed lines correspond to the flux calculated here, while the solid lines correspond to the flux found in [8].

and they are moving toward the detector. Each detected MCP is counted as many times as its weight predicts. The results are plotted together with the total MCP flux (corresponding to $\gamma = 1$) in Figure 6.3.

The results in Figure 6.3 are in reasonable agreement with Figure 5 in [8]. The most noticable difference between the two plots is that there is an additional increase of flux for the smallest MCP masses in [8]. This is due to the different methods used to calculate the flux, where the method used in [8] takes into account the three-body decay of π^0 to MCPs*. This decay was not taken into account in the method used here. The extent to which this affects the results will be discussed in Section 7.1.

To investigate if the assumption of constant matrix elements is reasonable in the calculations of the MCP flux above $\gamma = 6$, we make Dalitz plots for the Dalitz decays of η and π^0 for different values of the MCP mass. These results can be found in Appendix B, and they show that the variance of $|\mathcal{M}|^2$ is small. This indicates that the approximation of a constant matrix element is

*Private correspondence with Jonas Tjemsland.

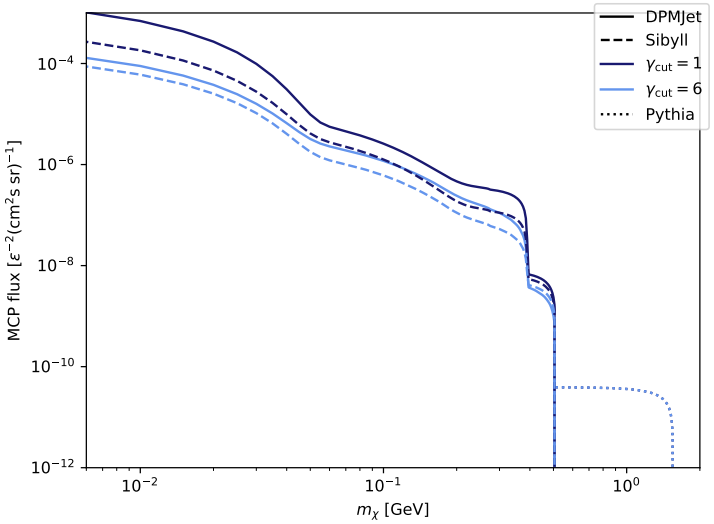

Figure 6.3: Total MCP flux resulting from the decays of $\pi^0, \eta, \rho^0, \omega, \phi$, and J/ψ mesons added together. The solid lines use the meson fluxes from DPMjet, while the dashed lines use Sibyll and the dotted line uses Pythia (J/ψ only). The dark blue lines show the total MCP flux, while the light blue lines include only produced MCPs with $\gamma > 6$ that are moving toward the detector. For J/ψ, the lines are practically overlapping.

reasonable.

6.3 Exclusion plot[†]

From the MCP flux plotted in Figure 6.3, we use Equation (3.4) to find $\epsilon(m_\chi)$. From Section 3.2.1 we know the values $N_e = 7.52 \cdot 10^{33}$, $t = 22.5\,\mathrm{kt\,yr}$ and $N_{e\chi} = 4$. We plot ϵ as a function of m_χ, and show the result in Figure 6.4. The black lines correspond to the limiting value of $N_{e\chi} = 4$, and the grey area illustrates what parts of the mass-charge plane are excluded. As described in Section 3.2.1, this section corresponds to MCPs that would result in a detection of more than 4 events per year, which is not in accordance with the observations at SK found in [24].

[†]Adapted from [1].

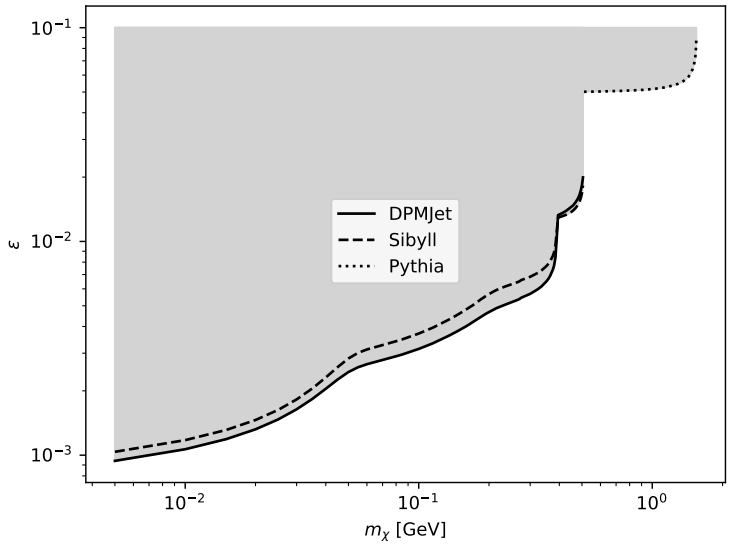

Figure 6.4: Upper limit for MCPs in the mass-charge plane. The grey area corresponds to more than 4 events detected per year and is therefore excluded. The black lines correspond to the MCP flux above $\gamma = 6$. The solid line uses data from DPMjet and the dashed line uses data from Sibyll. The dotted line uses data from Pythia (J/ψ only).

Figure 6.4 excludes MCPs of certain masses and charges from being candidates for DM, and thus helps narrowing the allowed parameter space of millicharged DM. The white areas of the plot still remain as candidates for DM.

6.4 Attenuation by scattering off electrons

6.4.1 Number density of electrons

We use the method described in Section 5.1 to find the average number density of electrons encountered by a particle passing through the Earth toward an underground detector at a depth d. The angle at which the particle approaches the detector from is denoted by θ. Figure 5.2 illustrates the geometry of the problem. We set $d = 1\,\text{km}$, which is the depth of SK. The average number

density of electrons as a function of the incoming angle at a detector with $d = 1\,\text{km}$ is plotted in Figure 6.5. We see that the number density of electrons greatly increases once the MCP has to pass through the Earth's core. This leads to a sudden increase in electron density at around 180°.

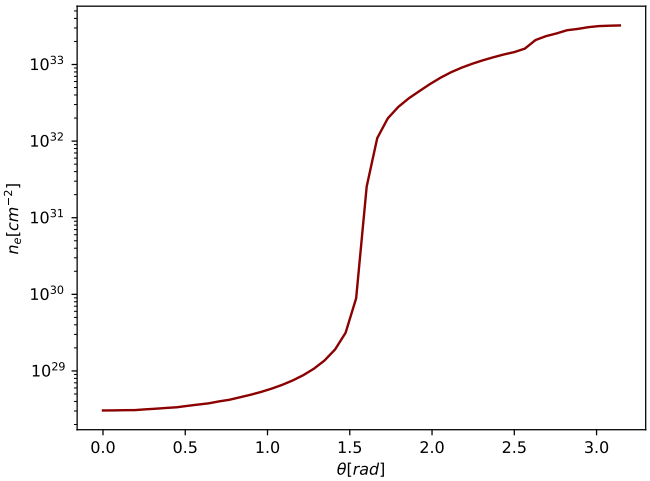

Figure 6.5: Number of electrons n_e per square cm encountered by a particle passing through the Earth, plotted as a function of the particle's incoming angle θ with respect to the detector. The detector is placed underground at a depth of 1 km.

6.4.2 Cross section and average energy loss

We will use the method described in Section 5.2 to calculate the fractional energy that an MCP with a given mass m_χ, charge eϵ and incoming energy E will have left when reaching an underground detector at a depth $d = 1\,\text{km}$ for different incoming angles θ.

We start by calculating the differential scattering cross section $\frac{\mathrm{d}\sigma}{\mathrm{d}y}$ using Equation (5.17). The result is plotted for different values of m_χ and E in Figure 6.6, with the dependence on ϵ factored out. Note that for the cases with larger m_χ the maximum value of y decreases significantly. This is due to there being a maximum value of the scattering angle when $m_\chi > m_e$, as described in Section 5.2.

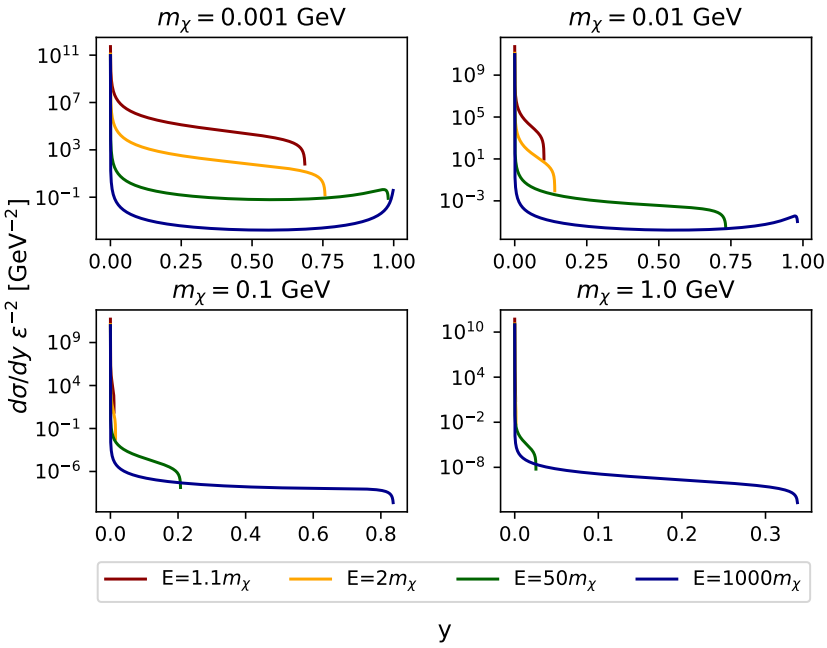

Figure 6.6: Differential cross section plotted as a function of the fractional energy loss y for different values of the MCP mass m_χ and incoming energy E. Each subplot represents a different value of m_χ and each color corresponds to a different value of E.

The total cross section is found by integrating the differential cross section over y. This was done numerically using the SciPy function for Simpson's method**. The result is shown for different values of m_χ in Figure 6.7, where the total cross section is plotted as a function of the incoming kinetic energy of the MCP. Again the charge-scaling factor ϵ has been factored out. As can be seen from the plots, the total cross section increases with the kinetic energy of the MCP. We also see that a larger MCP mass leads to a smaller total cross section.

The average fractional energy loss per interaction was found by inserting the results for the total cross section σ and the differential cross section $\frac{\mathrm{d}\sigma}{\mathrm{d}y}$ in Equa-

**https://docs.scipy.org/doc/scipy/reference/generated/scipy.integrate.simpson.html

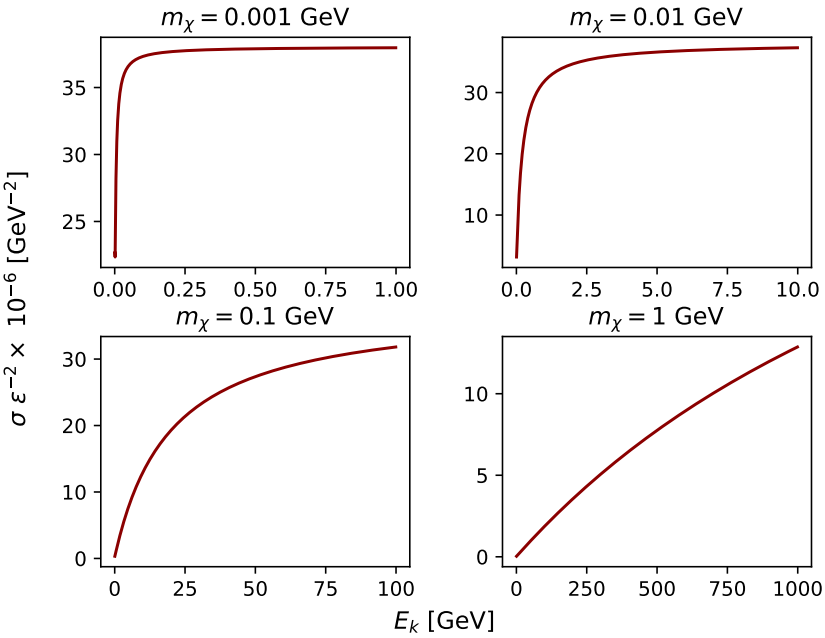

Figure 6.7: Total cross section for electron-MCP scattering plotted as a function of kinetic energy E_k. Each subplot corresponds to a different value of the MCP mass m_χ. Note that the charge scaling factor ϵ has been factored out from the total cross section.

tion (5.8). The result is shown in Figure 6.8, with each subplot corresponding to a different m_χ. We see that the energy loss decreases for increased kinetic energy. The energy loss also decreases for higher values of m_χ.

6.4.3 Energy left when reaching detector

We find the total energy loss along an MCP's path toward a detector due to scattering off electrons by using Equation (5.1). As a first approximation, we do the calculations treating the whole path as one single step. Due to this approximation, in some cases the fractional energy loss wil become more than 1. To solve this problem, we simply set the fractional energy loss equal to 1 in these cases.

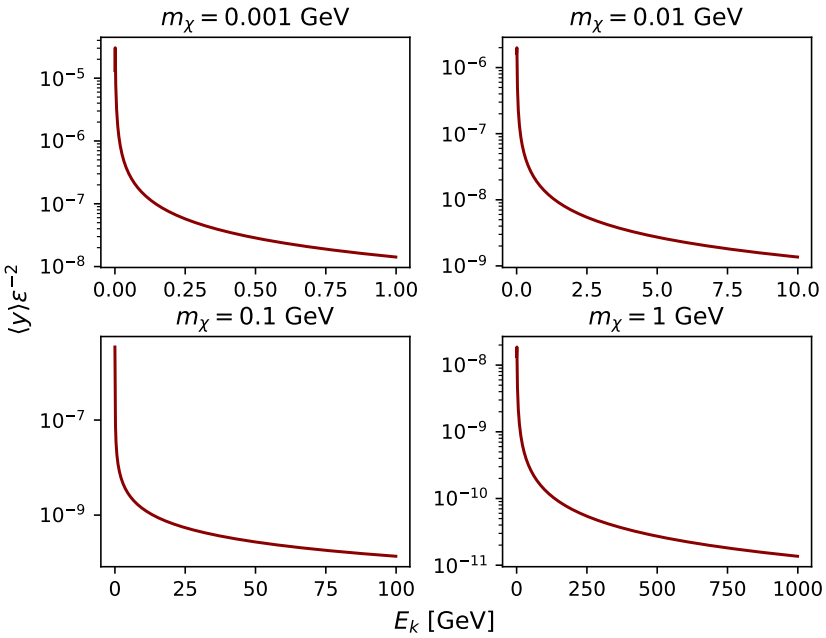

Figure 6.8: Average fractional energy loss due to scattering off electrons for electron-MCP scattering plotted as a function of the kinetic energy of the incoming MCP. The charge scaling factor ϵ has been factored out. The four subplots correspond to different values of the MCP mass m_χ.

The fractional energy left when reaching the detector for an MCP scattering off electrons is plotted as a function of the incoming angle θ in Figures 6.9 to 6.12. Each figure corresponds to different values of ϵ, and the subplots correspond to different values of m_χ. For each value of ϵ and m_χ, the energy fraction is plotted for different values of the energy of the MCP when entering the Earth's crust.

The effect of the Earth's core is clearly visible at approximately 180°, because of the shape of the number density of electrons plotted in Figure 6.5. The attenuation greatly increases once the MCPs have to pass through the core due to its high density.

From Figures 6.9 to 6.12, we see that a lower value of ϵ means less energy lost on the path to the detector. This is expected, as the interaction strength

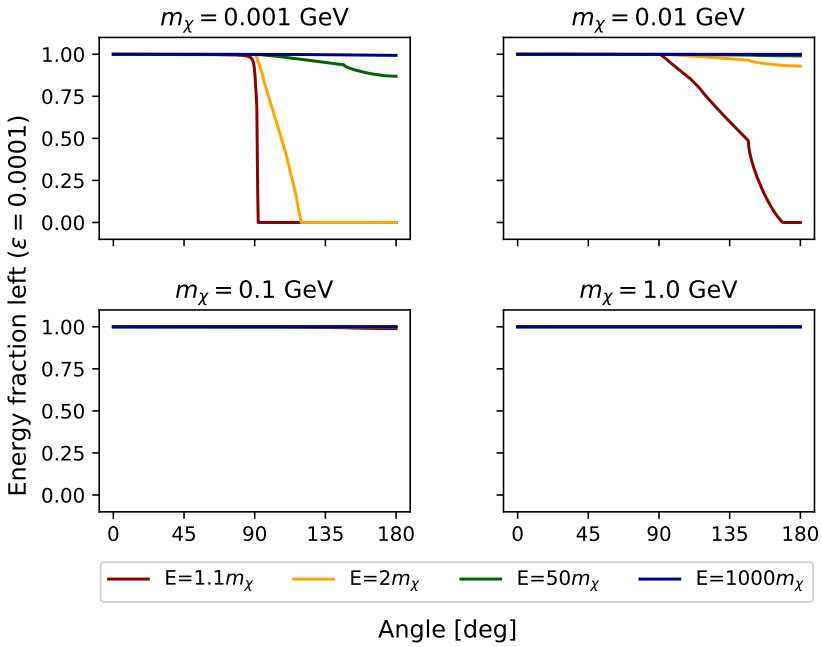

Figure 6.9: Fractional energy loss due to scattering off electrons for an MCP with $\epsilon = 10^{-4}$ and an incoming energy E when entering the Earth. Each subplot corresponds to different MCP masses m_χ, and show the energy left when reaching the detector for different values of the incoming energy.

between the MCPs and electrons is scaled by a factor of ϵ^2. We also see that a larger mass m_χ leads to reduced energy loss. For the cases of $\epsilon = 10^{-4}$ and $m_\chi > 0.1\,\text{GeV}$ or $\epsilon = 10^{-3}$ and $m_\chi = 1\,\text{GeV}$, virtually no energy is lost before reaching the detector. Thus, MCPs with relatively large masses and small charges will in general reach the detector without having lost much of their energy.

For the still open region of the MCP mass-charge plane in Figure 6.4, the contribution from upward-moving MCPs is considerable. This can be seen from, e.g., the plots for $\epsilon = 10^{-4}$ and $m_\chi \in [0.01, 0.1, 1]\,\text{GeV}$ in Figure 6.9, for $\epsilon = 10^{-3}$ and $m_\chi \in [0.1, 1]\,\text{GeV}$ in Figure 6.10 and the plot for $\epsilon = 0.01$ and $m_\chi = 1\,\text{GeV}$ in Figure 6.11. This means that the upward contribution has to be taken into

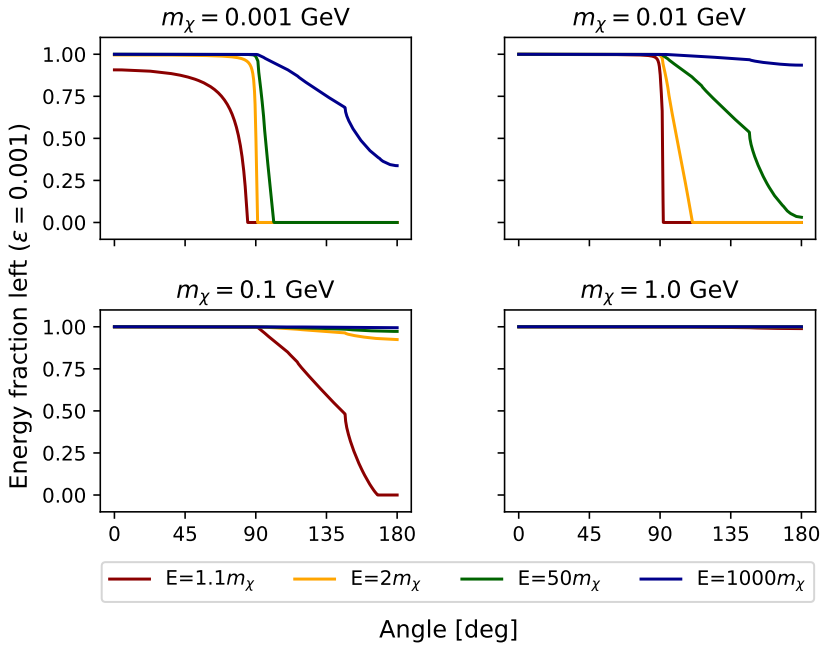

Figure 6.10: Fractional energy loss due to scattering off electrons for an MCP with $\epsilon = 10^{-3}$ and an incoming energy E when entering the Earth. Each subplot corresponds to different MCP masses m_χ, and show the energy left when reaching the detector for different values of the incoming energy.

account when exploring this region of the parameter space. For the excluded region, most upward-moving MCPs will not reach the detector. This is illustrated by Figure 6.12 and the plots for $\epsilon = 0.01$ and $m_\chi \in [0.001, 0.01, 0.1]$ GeV in Figure 6.11. Thus, one can argue that only taking into account downward-moving MCPs is a reasonable assumption for cases in the excluded region.

From our results we see that in almost all cases the downward-moving MCPs do reach the detector. Only for the cases of relatively large $\epsilon = 0.1$ and small mass m_χ does the Earth attenuation affect the MCPs arriving at the detector from above, as Figure 6.12 shows. Thus, in most cases we do not have to take into account the attenuation for downward-moving MCPs.

Figure 6.13 shows the energy fraction left for four different points approxi-

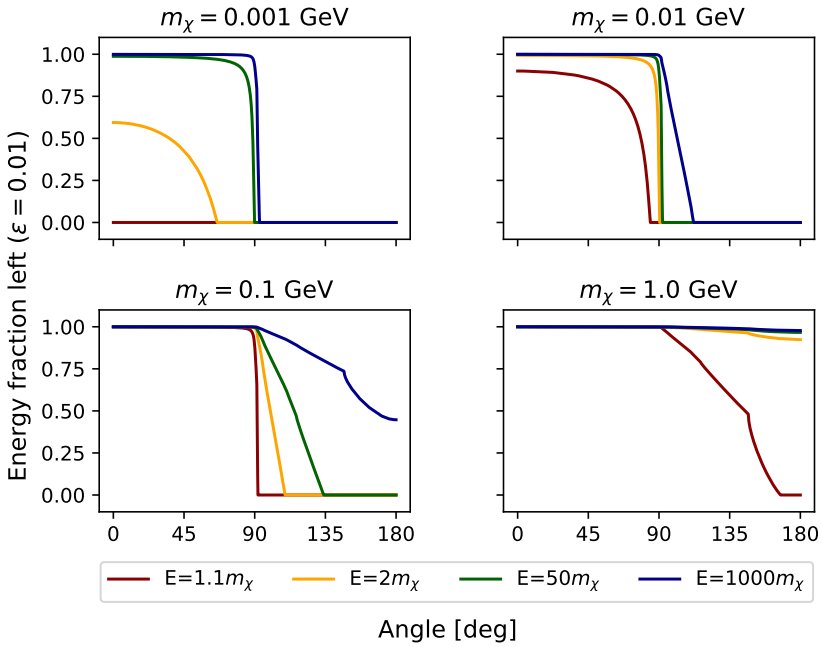

Figure 6.11: Fractional energy loss due to scattering off electrons for an MCP with $\epsilon = 0.01$ and an incoming energy E when entering the Earth. Each subplot corresponds to different MCP masses m_χ, and show the energy left when reaching the detector for different values of the incoming energy.

mately along the border of the excluded region in Figure 6.4. From these plots we see that only the MCPs with high incoming energies will have a significant energy fraction left when reaching the detector. The lowest energy MCPs on the other hand will have lost most of their energy when reaching the detector from below. It seems like the border along the excluded region is approximately where the assumption of MCPs only arriving from above starts to weaken.

To see if the one-step approximation described in the beginning of this section holds, we calculate the energy loss using a more precise method to allow for comparison. A first attempt was made choosing the step length so that the probability of interaction $N_e\sigma$ never exceeds 1. However, this turned out to be far too computationally time consuming for our purposes. Instead, we use

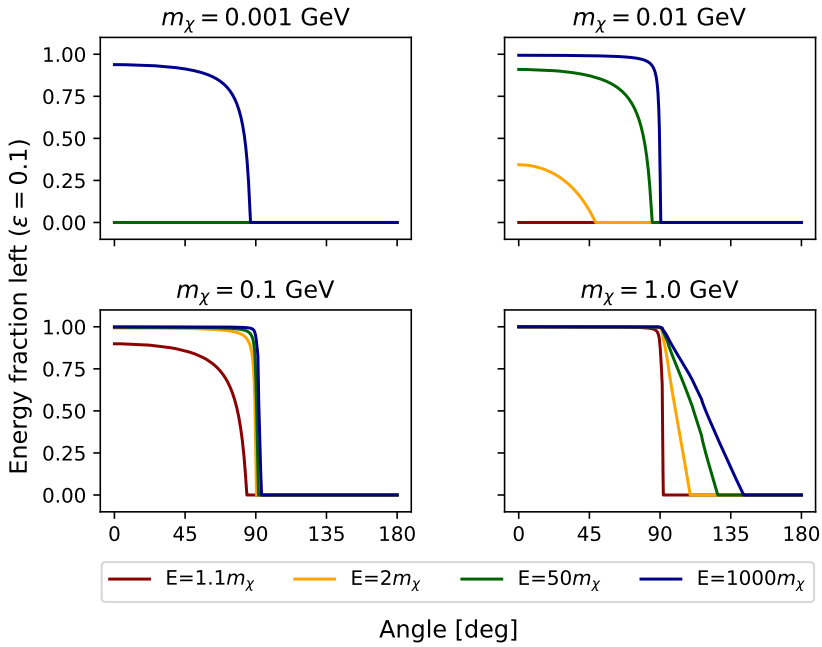

Figure 6.12: Fractional energy loss due to scattering off electrons for an MCP with $\epsilon = 0.1$ and an incoming energy E when entering the Earth. Each subplot corresponds to different MCP masses m_χ, and show the energy left when reaching the detector for different values of the incoming energy.

Equation (5.1) dividing the MCP path into smaller steps where the step length is for each step chosen so that the electron density and the MCP's energy both change with maximum 5% for each step. Figure 6.13 compares some results calculated using both methods. The difference between the results from the two methods is small as long as virtually all or no energy is lost. However, in the cases where a significant fraction of the energy is lost, the difference can be significant. This is the case for, e.g., $m_\chi = 1$, $\epsilon = 0.05$ and $E = 50m_\chi$ in Figure 6.13. Despite these differences the qualitative results can be argued to be the same since the parameter space where all or no energy is lost is virtually the same for both methods.

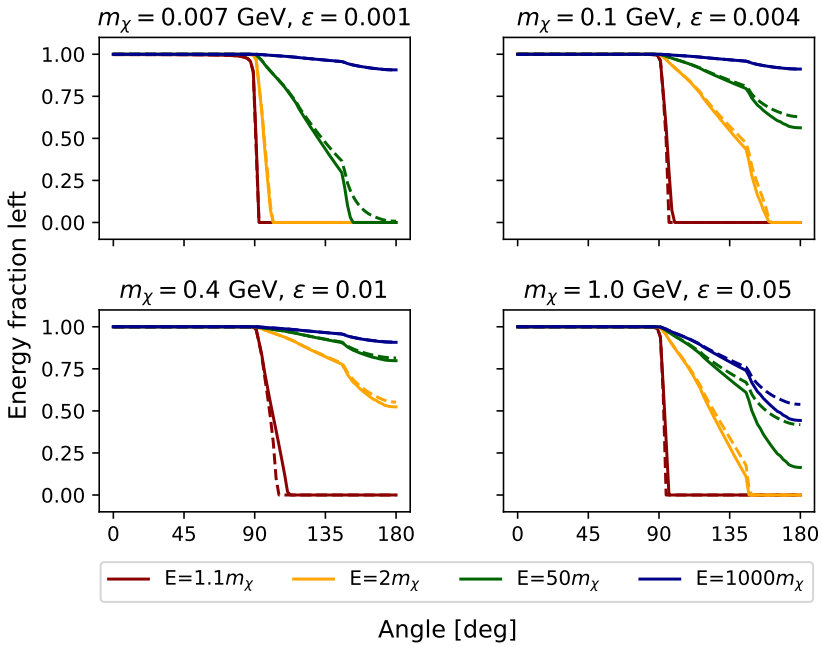

Figure 6.13: Fractional energy loss due to scattering off electrons for an MCP with incoming energy E when entering the Earth. The solid lines use the approximation of calculating the energy loss in just one step, while the dashed lines use a dynamic step length. Each subplot corresponds to different MCP masses m_χ and charge scaling factors ϵ, and they show the energy left when reaching the detector for different values of the incoming MCP energy. The points in the MCP mass-charge parameter space plotted for here are placed along the border of the excluded region.

6.5 Attenuation by scattering off nuclei

To find the average energy loss for MCPs scattering off nuclei, we use the same method as we did for MCPs scattering off electrons. The main difference is that we now have to include the form factor in Equation (5.24), reducing the total cross section for the interactions. We integrate Equation (5.25) over y to find the total cross section. We then insert into Equation (5.8) to find the average energy loss per interaction, using the same one-step approximation as we did

for scattering off electrons.

For the case of nuclei in Section 5.3, we have to take into account the chemical composition of the Earth to find the total number of nuclei of a given type encountered along a path of a given angle toward the detector. We do this using the data from Table 5.1 together with the density profile of the Earth given by Equation (5.2), as described in Section 5.3. The density as a function of the Earth's radius is found separately for each element. The energy loss calculations are also done separately for each element, before all the contributions are added together in the end.

The number of nuclei encountered is plotted as a function of the incoming angle at the detector for the different elements in Table 5.1 separately in Figure 6.14. The black line corresponds to the total number of nuclei, adding the contribution from all the elements together. Sulfur (S), which is practically not present in the Earth's crust, does not contribute to any energy loss of the MCPs arriving at the detector from above. Note also that for the elements practically not present in the core, e.g., for oxygen, the number of nuclei encountered decreases when the angle goes toward 180°, which is when the MCP has to pass through the core. The same effect can be seen for aluminum (Al) and calcium (Ca) just past 90° due to the high content in the crust and low content in the mantle.

6.5.1 Form factor

Figure 6.15 shows the form factor in Equation (5.24) plotted for the most common elements in the Earth. A form factor of 1 means that there is no reduction in the interaction strength. The form factor obtains values of order 10^{-3}, and thus it is important to consider.

From Figure 6.15 we see that the elements with higher atomic numbers and thus higher charges have a larger reduction of the interaction strength due to their form factor. Oxygen, having an atomic number of 8, has the largest form factor. The heaviest element, Nickel, has the smallest form factor, meaning a more prominent reduction of the total cross section. We also see that the reduction of the cross section is stronger for higher momentum transfers, with a rapid increase for small t.

6.5.2 Energy left when reaching detector

In general the energy loss of MCPs due to scattering off nuclei shows the same tendencies as the case for electrons, in that the energy loss is greater for bigger

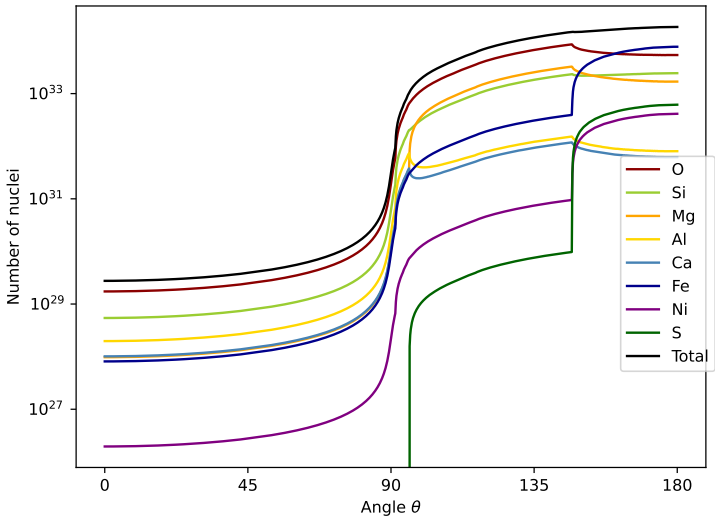

Figure 6.14: Number of nuclei encountered along an MCP's path toward an underground detector plotted as a function of the incoming angle at the detector. The different colored lines correspond to different elements. The black line shows the total number of nuclei for all elements added together.

charges and smaller masses. For masses of 1 GeV, the energy loss for MCPs with $E > 5m_\chi$ is negligible even for relatively large charges ϵe with $\epsilon = 0.1$. In the same case for low energy MCPs, the energy loss is negligible if $\epsilon < 10^{-3}$. For cases with a small $\epsilon = 10^{-4}$, only low-energy MCPs lose a significant amount of energy, even when the mass is as small as $m_\chi = 10^{-3}$ GeV.

Figure 6.16 shows the energy fraction that is left when reaching a detector placed 1 km underground for MCPs of different charges, masses, energies and incoming angles at the detector. The values were chosen to show the interesting cases where only a fraction of the energy is lost. Note that the energy factors here are smaller than in the corresponding plots for MCPs scattering off electrons.

6.6 Attenuation by bremsstrahlung

As already mentioned in Section 5.4, for the case of MCP energy loss due to bremsstrahlung the differential scattering cross section is not given. Because of this we have to carry out the calculations from the beginning, starting with the

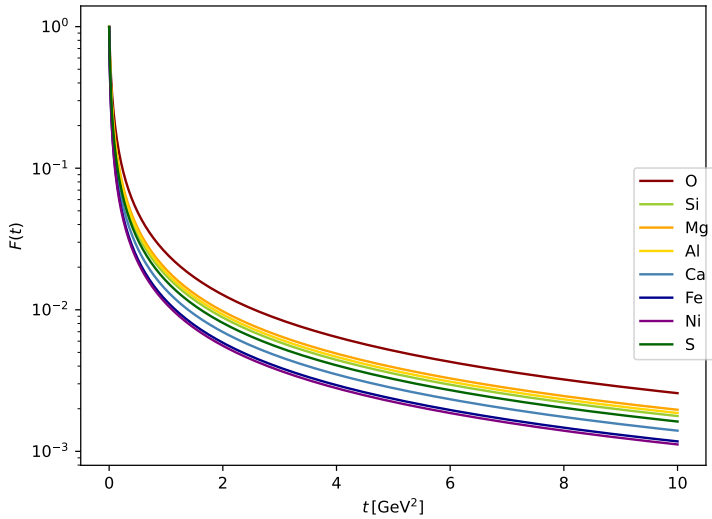

Figure 6.15: Form factor for the NNγ-vertex for an MCP scattering off a nucleus, plotted for different elements. The form factor F is plotted as a function of $t = -q^2$, where q is the momentum transfer of the interaction.

squared amplitude. We can then follow the method described in Section 5.4 to find the average energy loss per interaction. From this we can find the total energy loss of MCPs traversing the Earth due to bremsstrahlung.

We start by finding a symbolic expression for the squared amplitude for the Feynman diagrams shown in Figure 5.6 using the CalcHEP package [34]. Our CalcHEP model consists of the SM plus the added MCP which couples to the photon with a strength scaled by the small factor ϵ. A nucleus was also added as a new particle to include the nucleus mass and charge in our calculations. To add the MCP to the model, we edit the CalcHEP SM model files, which are described in the documentation [34]. We add the MCP mass and the charge factor ϵ as variables to the `varsN.mdl` file. To the `prtclsN.mdl` file we add the MCP as a new particle with spin 1/2 and an antiparticle partner. We then add a photon-MCP vertex scaled by the ϵ factor to the `lgrngN.mdl` file. The nucleus was added to the model in the same way, by introducing its mass as a variable, adding it to the particle list and including a photon-nucleus vertex.

We use Mathematica* to further carry out our calculations, utilizing CalcHEPs

*https://www.wolfram.com/mathematica/

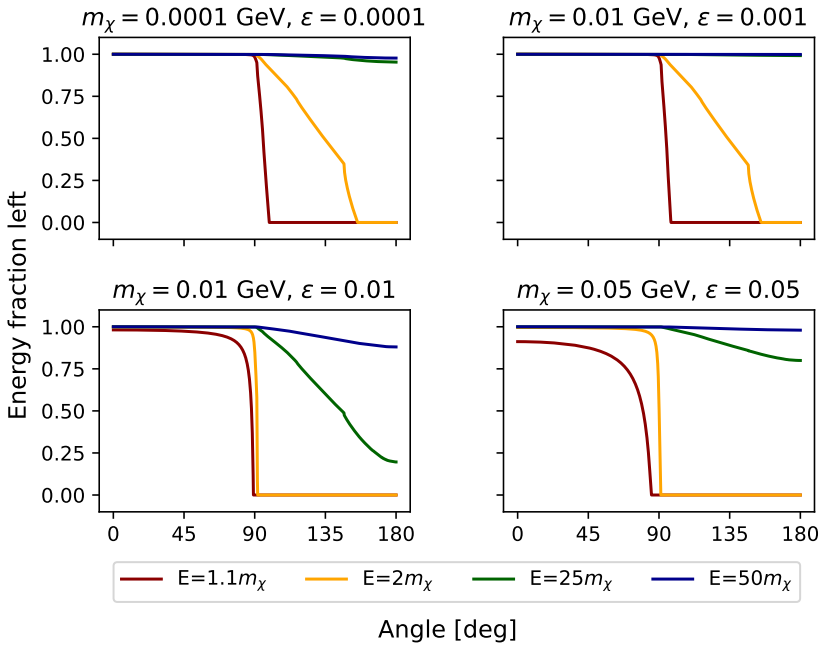

Figure 6.16: Fractional energy left for MCPs traversing the Earth while losing energy due to scattering off nuclei, plotted as a function of the incoming angle at the detector. Each plot corresponds to different values of the MCP mass m_χ and the charge scaling factor ϵ. The different colors correspond to different MCP energies.

option of getting the squared amplitude as output for Mathematica. A first attempt was made to find an analytic expression for $\frac{\mathrm{d}\sigma_{\mathrm{brems}}}{\mathrm{d}y}$. However, no expression was found, either because the computation was far too time-consuming, or because the expression was not analytically solvable. Because of this, we decide to use the `NIntegrate` function in Mathematica to try to evaluate the integral numerically. We run into several problems trying to do this, among them problems with convergence, the estimated error being of the same order of magnitude as the output and the output having imaginary parts. These issues prevailed regardless of the chosen integration strategy.

To investigate where these problems arise, we decide to look more closely at

each of the factors making up the integrand in Equation (5.38). We do not find any problems regarding the form factor or the Jacobian. The squared amplitude is positive for all of our parameter space, but we notice some inaccuracies when the energy loss y becomes very small in the form of slighty negative numbers very close to zero. This is probably due to numerical inaccuracies.

We run into trouble regarding the factor of the integrand stemming from the phase space integral, $1/\sqrt{(-\Delta_4)}$. We evaluate the phase space factor for different combinations of y, θ, t_2, and s_1 and note that when two or more parameters are close to their minimum or maximum value simultaneously, the factor evaluates to complex numbers. We find that this is caused by $-\Delta_4$ evaluating to a small, negative number, possibly due to numerical inaccuracy. This produces an imaginary number when taking the square root. Since we divide by $\sqrt{(-\Delta_4)}$, this small, imaginary factor becomes large. It seems like increasing m_χ allows us to come closer to the integration boundary before this problem arises. This issue could be solved by only taking the real part of the integral.

We construct plots for the phase space factor in the s_1-t_2 plane for given values of y and θ. One such plot is shown in Figure 6.17. As can be seen from the figure the integration region is relatively smooth, but the boundary of the integration region is covered by sharp peaks. These peaks arise when $\sqrt{(-\Delta_4)}$ becomes close to zero, and they will cause convergence problems when we try to integrate numerically. Suggestions on how to approach this issue will be presented in Chapter 7.

Changing our parameters affects the size of the integration region in the s_1-t_2 plane and the relative height of the peaks. Increasing the MCP mass makes the integration region larger and gives relatively smaller peaks. The same goes for increasing the incoming energy of the MCP. Larger atom numbers also decrease the relative height of the peaks. Decreasing θ or y makes the integration region smaller. This means that extra care has to be taken especially for small values of m_χ, m_N, and the incoming energy E.

6.7 Total attenuation

Figure 6.18 shows the energy loss for MCPs due to scattering off electrons and scattering off nuclei added together. From the plot, it is clear that the energy loss due to electrons dominates. This is because of the screening parameter and the form factor in Equation (5.24), both leading to a reduction of the cross section of the MCP-nucleus interaction. The cross section for MCP-nucleus scattering

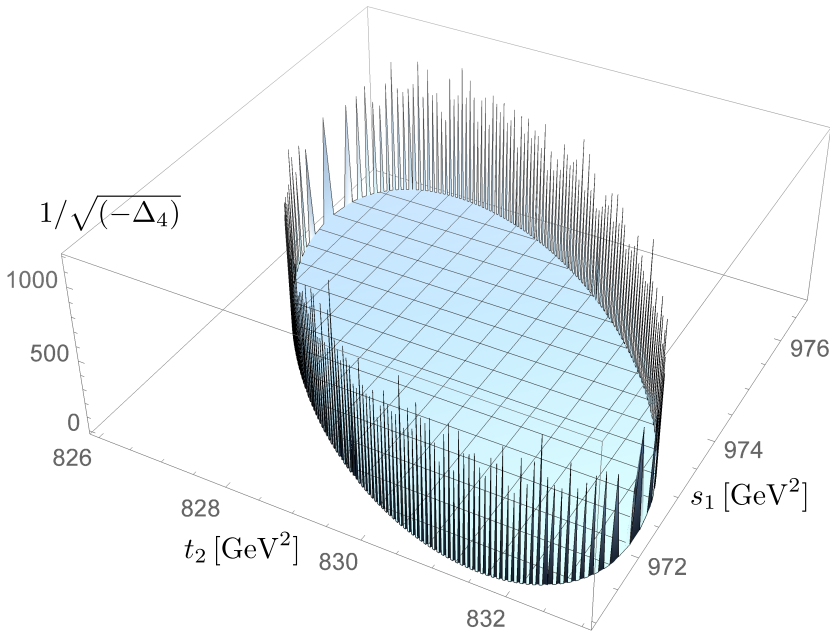

Figure 6.17: The phase space factor $1/\sqrt{(-\Delta_4)}$, plotted for $y = 0.45$ and $\theta = 0.5\pi$ in the s_1-t_2 plane. The other parameters were set to $m_\chi = 0.1\,\mathrm{GeV}$, $E = 25m_\chi$ and $Z = 16$.

is scaled by a factor of Z^2, but this does not increase the total energy loss because the total number of protons equals the number of electrons. Figure 6.18 shows that the results including electrons only in most cases are fairly similar to the total result. Thus, considering electrons only could be used as a useful approximation. However, MCP-nucleus scattering still plays an important role in the attenuation of the MCP flux, and thus should also be considered for more accurate results.

To briefly summarize our results for the Earth attenuation of MCPs, it seems that for the excluded area the assumption of only counting downward-moving MCPs is reasonable. However, for the still remaining area MCPs arriving from below the detector should also be taken into consideration. The border between these two areas shows cases of only energetic MCPs reaching the detector from below.

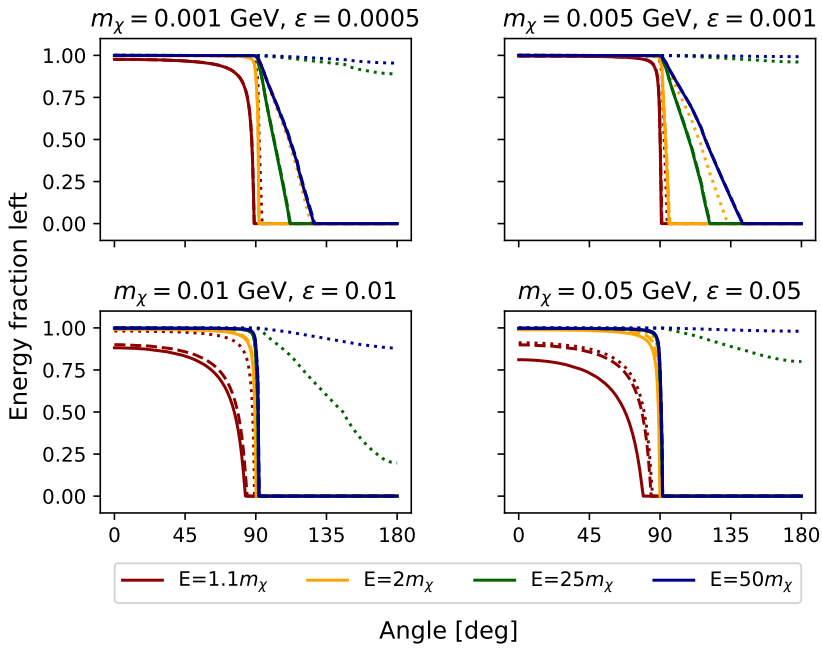

Figure 6.18: Energy fraction left for MCPs reaching an underground detector at a depth of 1 km from an incoming angle θ. The dashed lines show the contribution from scattering off electrons only, the dotted lines show the contribution from scattering off nuclei only, while the solid lines show the results for both the mentioned processes added together. Each plot corresponds to different values of the MCP mass m_χ and the charge scaling factor ϵ. The different colors correspond to different MCP energies.

Chapter 7

Discussion

In this section we discuss the accuracy and applicability of our results and the validity of our assumptions. We also present some suggestions for further work. The last section presents new experimental results that can be used to improve our exclusion plot in the MCP mass-charge plane.

7.1 MCP flux and exclusion plot[†]

Our results for the MCP fluxes and the exclusion plot are in relatively good agreement with [8], [14]. However, there are ways in which the accuracy of the results can be improved.

Since our results are calculated using the cosmic ray meson fluxes, improved estimations of them will lead to improved approximations of the MCP fluxes. The exclusion plot, which is arguably the most important result, is calculated using the integrated MCP flux above $\gamma = 6$. Thus, more accurate calculations of the MCP flux above $\gamma = 6$ will give a more accurate exclusion plot.

In our calculations of the MCP flux above $\gamma = 6$, we assumed the matrix elements to be constant. We notice some slight differences between our results and the corresponding results found in [8], [14], and the reason behind this could be our constant matrix element approximation. The Dalitz plots presented in Appendix B show that the matrix elements have relatively small variances, which means approximating them as constant is reasonable. To further investigate the accuracy of this approximation, one could include the actual matrix elements

[†]Adapted from [1].

and compare the results directly with the results obtained with the constant matrix element approximation. Including the matrix elements could also improve the accuracy of the exclusion plot.

Another suggestion for improvement is including the contribution from the $\omega \to \pi^0 \chi \bar{\chi}$ decay. This was done in [8], but not in [14]. The BR for $\omega \to \pi^0 \ell^+ \ell^-$ is about ten times larger than the direct lepton decay of ω, but the decay is only valid for MCP masses below 325 MeV, while the direct decay is valid for MCP masses up to 390 MeV [14]. This means that the three-body decay of ω will only contribute for MCP masses below 32 MeV. In the region of $275\,\text{MeV} > m_\gamma > 325\,\text{MeV}$, neglecting the three-body decay will lead to the MCP flux being underestimated by a small factor [14]. In conclusion, including the three-body decay will give slightly more accurate results, but not taking it into account is a reasonable approximation.

7.2 Earth attenuation

Comparing the energy loss for MCPs due to scattering off nuclei with the energy loss due to scattering off electrons, it is clear that the energy loss due to electron-MCP scattering dominates. This is because of the screening effect, which was taken into account by the screening parameter a. The form factor also reduces the interaction strength, especially for higher momentum transfers. Since the energy loss from scattering off electrons dominates, a useful approximation is to only consider this process when looking at the attenuation due to the $2 \to 2$ processes. This is why the electron results were investigated more thoroughly in Chapter 6. Most of the observations made regarding the MCPs scattering off electrons also apply to the case of MCPs scattering off nuclei.

We encountered numerical problems when trying to evaluate the integral for finding the average energy loss per interaction for the case of bremsstrahlung. As Figure 6.17 shows, the region of integration for the phase space factor diplays sharp peaks along the boundary of the integration region causing convergence problems when we try to evaluate the integral numerically. Because of the high dimensionality it was not possible to solve this problem by simply increasing the minimum limits and decreasing the maximum limits slightly. To eliminate the problematic areas completely we would have to increase or decrease the limits by a significant percentage to avoid the cases where we get sharp peaks due to all four variables being close to their extreme values simultaneously. This would alter the final evaluation of the integral too much due to the integrand increasing toward the boundaries in some cases.

One way to approach this problem is by evaluating the integral using a Monte Carlo method with a low number of sampling points. Few sampling points gives a small probability of hitting one of the peaks along the boundary. When the number of sampling points is increased, the error estimate will suddenly become larger once there is enough sampling points for the probability of hitting one of the peaks to be considerable. This strategy would also help us deal with the inaccuracies very close to the lower limit of y for the squared amplitude. One could also try to avoid $\sqrt{-\Delta_4}$ becoming imaginary by adding a very small number inside the square root. Due to the time limit there was not enough time to explore these strategies.

Because of the problems we encountered when trying to solve the integral in Mathematica, it might be better to try some other software that can handle our complicated integrand in a more sophisticated way. Once the average energy loss per interaction is found, the method used for finding the total energy loss from scattering off electrons and nuclei can easily be applied to the case of bremsstrahlung.

The total scattering cross section for the bremsstrahlung process can be calculated using CalcHEP. For a future check of the validity of our results, $\mathrm{d}\sigma_{\mathrm{brems}}/\mathrm{d}y$ can be integrated numerically over y to compare with the total scattering cross section computed by CalcHEP.

It would be interesting to investigate some limiting cases, for example for small m_χ. Approximating m_χ as small could help us simplify the integrand for the case of bremsstrahlung, allowing us to investigate the bremstrahlung energy loss for low mass MCPs. It would also be interesting to see how changing the depth of the detector affects the energy loss for downward-moving MCPs.

We did not include the attenuation from e^+e^- pair production, but this process should be included in further analyses. The four particle final states complicates the calculations severely, both for finding the amplitude and for the phase space integral. It should be possible to find the average energy loss per interaction for this process using the same method as we described for bremsstrahlung. However, due to the increased complications numerical difficulties should be expected.

The fact that in some cases also upward-moving MCPs can reach the detector means that the expected number of events in the detector will increase in some cases. In general, larger m_χ, smaller ϵ and higher incoming energy will have contributions from upward-moving MCPs giving a larger expected number of detector signals than anticipated with previous analyses. This will impose a stricter limit in the exclusion plot, because more of the MCP parameter space will lead to a number of events that is larger than the one observed. On the other

hand, our results also demontrated that in some cases when m_χ is small while ϵ is large, low energy MCPs will experience a significant attenuation also when arriving at the detector from above. For this region of the MCP parameter space, the number of events would be lower than expected, thus perhaps reopening some regions of the MCP parameter space.

From the results from [22], we find that for low energy MCPs in our studied mass range of approximately 10^{-3} GeV to 1 GeV the energy loss due to ionization dominates. However, for MCPs with $E > 10$ GeV, the energy loss due to e^+e^- pair production dominates [22]. This process was not included here, which means our results are most accurate for lower energy MCPs. For an accurate analysis of the higher energy MCPs the pair production prosesses need to be considered. The energy loss due to bremsstrahlung is larger for more energetic MCPs and smaller masses [22], which means the effects of not taking it into account are more prominent for these cases.

The energetic MCPs will experience more attenuation than what our analysis shows due to the dominating contribution from e^+e^- pair production, and due to bremsstrahlung. However, our results are highly applicable to lower energy MCPs, for which ionization is the main cause of energy loss. We also note that in the cases where energetic MCPs do not reach the detector due to scattering off electrons and nuclei, including the energy loss from pair production would not affect the results. It is for the cases where all or some energetic MCPs reach the detector that our results are not necessarily valid.

Some of the MCPs that reach the detector might have lost so much of their energy that they drop below the threshold for them to be observable [22]. As mentioned in Section 3.2, only MCPs with a Lorentz factor $\gamma > 6$ will have enough energy to be detected by SK. Thus, when using our results for the energy fraction left for MCPs reaching the detector, one should keep this threshold in mind when deciding if a given MCP will produce a signal.

Including analyses for the energy loss of MCPs due to pair-production and bremsstrahlung is arguably what will have the most impact on the accuracy of the exclusion plot. Once the average energy loss per interaction is found for these cases, we can apply the same method as we did for scattering off nuclei and electrons to find the total energy loss.

7.2.1 Assumptions

Several assumptions were made about the Earth. First of all, the Earth was assumed to be perfectly spherical. In reality, the oblate spheroid shape of the Earth gives the MCP a slightly shorter path if it is travelling from south to a

detector placed at the northern hemisphere, than if it is travelling along the equator. However, the ratio between the semiminor and semimajor axis of the Earth is approximately 0.9966 [37], and thus this should not affect the results noticeably. With our simplified model, mountains are not taken into account and we take the density of the crust as the average of oceanic and continental crust. If the detector is placed under a large mountain, this would lead to less MCPs reaching it from above than anticipated with our model. However, we are mostly interested in the attenuation of upward-moving MCPs, for which this would not affect our results. As can be seen in Figure 5.1, the density is much higher at the core than in the crust, and so the passing through the core leads to significantly more energy loss than passing through the crust. Using a more detailed model of the Earth's shape and composition would improve the results slightly, especially for downward-moving MCPs. However, there are other ways to increase the accuracy which should be considered first, such as including all attenuation processes.

When calculating the energy loss of the MCPs traversing the Earth, the deflection angles due to the interactions with electrons and nuclei were not taken into account. In other words the MCP paths were treated as being straight. This assumption is reasonable because the MCPs that reach the detector will mostly lose a small amount of their kinetic energy in each interaction, which corresponds to a small deflection angle. A large deflection angle means a greater loss of kinetic energy, which reduces the chances of the MCP reaching the detector. Thus, in general the MCPs reaching the detector will not have experienced any large angle deflections. In addition, several smaller angle deflections would to some degree cancel each other out.

7.2.2 Calculation of fractional energy loss

The approximation that was used when calculating the energy loss along the MCP's path toward the detector works well for the cases where virtually all or none of the energy is lost. This is because when the energy loss is very small, the number of interactions and the change in energy is also small and thus the two methods will give almost the same results. When the fractional energy loss is close to 1, the MCPs lose their energy quickly and thus the approximation of only one step is reasonable. However, as already mentioned, the results are not as accurate when the fractional energy loss is not close to 0 or 1. This is because in these cases the reduction of the energy loss per interaction due to decreasing energy becomes significant.

To check our one step approximation, We investigated a method with a

dynamic step length chosen so that the change in energy and density remain small. As long as both these parameters remain fairly constant, a larger step length will give accurate results. We compared the results obtained with this method with the one-step simplification in Figure 6.13, and the results were qualitatively very similar. Because of this we continued to use the simpler method, as this was less time consuming. However, further analyses should preferably be done using the dynamic step length method. The highest accepted change for each step could also be set to a smaller number than the 5 % limit we used here.

7.3 Outlook[†]

New, experimental results can further constrain the possible regions for MCPs in the mass-charge plane. Some examples are given below. The method for finding the upper limit for MCPs in the mass-charge plane that was described in Section 3.2 can be applied to the new data from these upcoming experiments.

To increase the sensitivity of the SK, 13 tons of gadolinium was added to the water of the detector in 2020 [38]. In July 2022, the gadolinium concentration was increased from 0.011% to 0.033%, increasing the neutron capture percentage from 50% to 75% [39]. The new measurements for SK with gadolinium loaded water can be used to better estimate the background contamination in the search for solar neutrinos [39], thus improving the accuracy of the results in [24] that we used to construct our exclusion plot. Future measurements are expected to be even more efficient [39].

The upcoming Hyper-Kamiokande (HK) is a next generation large water Cherenkov detector based on the SK detector [40]. It will exceed the performance of SK, with far-reaching sensitivities and it has a great potential for exploring low energy physics [40]. Thus, HK can give new results aiding the search for MCPs in the sub-GeV mass range.

Borexino is a large volume liquid scintillator detector with a main goal of measuring low energy solar neutrinos [41]. The detection mechanism used in the Borexino detector has several advantages over the water Cherenkov detectors, such as SK, allowing for effective detection of sub-MeV solar neutrinos [41]. The first measurements of directionality of sub-MeV solar neutrinos scattering elastically off electrons in a liquid scintillator target was recently published by the Borexino Collaboration [42]. This information on directionality can be used to improve background suppression and to distinguish different signals from each

[†]Adapted from [1].

other [42]. Combined with our information about the directional attenuation of MCPs, the directionality information about the solar neutrinos could be used to distinguish the two signals from each other.

New data from these experiments can help us move forward in the search for DM by placing even stricter limits on the possible masses and charges for MCPs. This means that we can create even more stringent exclusion plots, helping us move further in the search for millicharged DM.

Chapter 8

Conclusion

From the cosmic ray meson fluxes found by Kachelrieß and Tjemsland in [8], we found the resulting flux of MCPs with enough energy to produce a signal in the SK detector. From these results we constructed an exclusion plot in the MCP mass-charge plane, ruling out parts of the MCP parameter space as candidates for DM. Our results are in agreement with [8], [14].

As a manner of improving these results, we chose to focus on analyzing the attenuation of the incoming MCP flux due to the Earth's density. We found that the attenuation of the MCP flux is important to take into account when using the results of underground detectors such as SK to construct exclusion plots in the MCP mass-charge plane. Future improved exclusion plots should thus be constructed with this or similar analyses in mind.

We found that in the excluded region of the MCP mass-charge plane, most upward-moving MCPs will not reach the detector. Thus, it is a reasonable assumption to only count downward-moving MCPs for cases in the excluded region. However, for the still open region the contribution from upward-moving MCPs is significant and should be considered. We also found that the attenuation of downward-moving MCPs only needs to be considered for large ϵ and small m_χ, with small incoming energies.

Most of the MCPs' energy loss was due to scattering off electrons, but scattering off nuclei should also be counted in, although the effects are less prominent. We also note that for a complete analysis, the calculation of the energy loss from bremsstrahlung should be completed. The energy loss due to pair-production should also be considered, especially for energetic MCPs for which this is the dominant energy loss mechanism.

With our analysis of the Earth attenuation of MCPs, we can improve the estimations of the number of MCP signals in an underground detector. The information about the MCP directionality can be combined with the new results on the directionality of solar neutrinos from the Borexino collaboration to distinguish the signals from each other. This new information will allow us to create even more stringent exclusion plots, moving us one step further in the search for millicharged DM.

Appendix A

Calculation of meson branching ratios into MCPs[†]

In this section, we will show how to calculate the rescaled BRs presented in Section 4.2. We start by calculating the rescaled BR for the direct decay of a meson into two MCPs. We will then perform the calculations for the Dalitz decay $P \to \gamma\chi\bar{\chi}$.

A.1 Direct decay

The Feynman diagram for the direct decay of a meson into two charged leptons is shown in Figure A.1, where the grey circle represents the mechanism described by the form factor of the meson. From Equation (2.6) we have that the BR of the direct decay of a meson into two leptons is given by

$$\mathrm{BR}(m \to l^+ l^-) = \frac{\Gamma_{m\to l^+l^-}}{\Gamma_{\mathrm{tot}}}, \tag{A.1}$$

where $\Gamma_{m\to l^+l^-}$ is the decay rate of the direct lepton decay. From Equation (A.1), we get that the ratio between the BRs for the direct decay of a

[†]Adapted from [1].

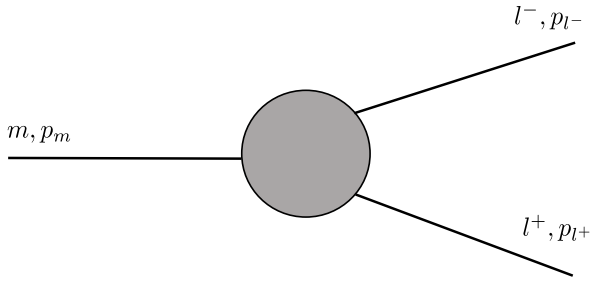

Figure A.1: Feynman diagram of the direct decay of a meson m with four-momentum p_m into two leptons l^- and l^+ with four-momenta p_{l^-} and p_{l^+}.

meson into leptons versus MCPs is given by

$$\frac{\mathrm{BR}(m \to \bar{\chi}\chi)}{\mathrm{BR}(m \to l^+l^-)} = \frac{\Gamma_{m\to l^+l^-}}{\Gamma_{m\to\bar{\chi}\chi}}, \tag{A.2}$$

where $\Gamma_{m\to\bar{\chi}\chi}$ is the decay rate of the direct decay into two MCPs. We start by calculating $\Gamma_{m\to l^+l^-}$ by using Equation (2.8), which states that

$$\begin{aligned}\Gamma_{m\to l^+l^-} =& \frac{S}{2m_m}\int |\mathcal{M}|^2 (2\pi)^4 \delta^4(p_m - p_{l^+} - p_{l^-}) \\ &\times \frac{1}{2\sqrt{\mathbf{p_{l^+}}^2 + m_l^2}} \frac{1}{2\sqrt{\mathbf{p_{l^-}}^2 + m_l^2}} \frac{\mathrm{d}^3\mathbf{p_{l^+}}}{(2\pi)^3} \frac{\mathrm{d}^3\mathbf{p_{l^-}}}{(2\pi)^3},\end{aligned} \tag{A.3}$$

where m_m is the meson mass, m_l is the lepton mass, p_{l^-} and p_{l^+} are the four-momenta of the leptons, and p_m is the meson four-momentum. In the meson rest frame we can rewrite the delta function as

$$\begin{aligned}\delta^4(p_m - p_{l^+} - p_{l^-}) =& \delta^3\left(\mathbf{p_{l^+}} + \mathbf{p_{l^-}}\right) \\ &\times \delta\left(m_m - \sqrt{\mathbf{p_{l^+}}^2 + m_l^2} - \sqrt{\mathbf{p_{l^-}}^2 + m_l^2}\right).\end{aligned} \tag{A.4}$$

We use the first delta function when doing the integral over $\mathbf{p_{l^-}}$, which gives

$$\Gamma_{m\to l^+l^-} = \frac{S}{32\pi^2 m_m} \times \int |\mathcal{M}|^2 \frac{\delta\left(m_m - \sqrt{\mathbf{p_{l^+}}^2 + m_l^2} - \sqrt{\mathbf{p_{l^-}}^2 + m_l^2}\right)}{\mathbf{p_{l^+}}^2 - m_l^2} \mathrm{d}^3\mathbf{p_{l^+}}. \tag{A.5}$$

Now only the integral over $\mathbf{p_{l^+}}$ remains, and to evaluate it we switch to spherical coordinates with $\mathrm{d}^3\mathbf{p_{l^+}} = |\mathbf{p_{l^+}}|^2 \sin\theta \mathrm{d}|\mathbf{p_{l^+}}|\mathrm{d}\theta\mathrm{d}\phi$. Since there is no angular dependence, the angular integrals evaluate to 4π and we are left with

$$\Gamma_{m\to l^+l^-} = \frac{S}{8\pi m_m} \int |\mathcal{M}|^2 \frac{\delta\left(m_m - 2\sqrt{|\mathbf{p_{l^+}}|^2 + m_l^2}\right)}{|\mathbf{p_{l^+}}|^2 - m_l^2} |\mathbf{p_{l^+}}|^2 \mathrm{d}|\mathbf{p_{l^+}}|. \tag{A.6}$$

We now do another change of variables to $E_{l^+} = |\mathbf{p_{l^+}}|^2 + m_l^2$, and we use the delta function when doing the integral. This leaves us with the following expression for the decay rate:

$$\Gamma_{m\to l^+l^-} = \frac{S|\mathcal{M}|^2}{8\pi m_m^2} \sqrt{1 - \frac{4m_l^2}{m_m^2}}. \tag{A.7}$$

The calculation is similar for the decay $m \to \chi\bar{\chi}$, with the MCPs in place of the leptons. The only difference is that the squared amplitude is scaled by a factor of ϵ^2 compared to the squared amplitude for the leptons. This is due to the difference in the interaction strength. The ratio between the BRs (or decay rates) is thus

$$\frac{\mathrm{BR}(m \to \bar{\chi}\chi)}{\mathrm{BR}(m \to l^+l^-)} = \frac{\Gamma_{m\to l^+l^-}}{\Gamma_{m\to\bar{\chi}\chi}} \propto \epsilon^2 \frac{\sqrt{1 - 4m_\chi^2/m_m^2}}{\sqrt{1 - 4m_l^2/m_m^2}}, \tag{A.8}$$

where the last factor comes solely from the phase space calculations. To get a more accurate expression one could also take into account the matrix element, giving an additional factor determined by the phase space integral of the squared amplitude for the process of $\gamma^* \to l^+l^-$, where γ^* is a virtual photon. This was done in [43] by using the optical theorem. The derivation is outside of the scope of this thesis, and we quote the result which is an additional factor of $(1 + 2m_l^2/m_m^2)$. An equivalent factor of $(1 + 2m_\chi^2/m_m^2)$ is also added for the MCP decay, and thus we will insert an additional factor of

$$\left(\frac{1+2m_\chi^2/m_m^2}{1+2m_l^2/m_m^2}\right) \tag{A.9}$$

into Equation (A.8). The same factor is found in [44]. Doing this we end up with

$$\frac{\mathrm{BR}(m\to\bar{\chi}\chi)}{\mathrm{BR}\,(m\to l^+l^-)} = \epsilon^2\sqrt{\frac{1-4m_\chi^2/m_m^2}{1-4m_l^2/m_m^2}}\left(\frac{1+2m_\chi^2/m_m^2}{1+2m_l^2/m_m^2}\right), \tag{A.10}$$

which is the same expression as found in [8].

A.2 Dalitz decay

The calculations in this section follow the method used in [45], but with more details and with MCPs in place of the charged leptons. The BR will be found from comparison with the decay of the meson into two photons, $m\to\gamma\gamma$. The Feyman diagram of this process is shown in Figure A.2. We start by calculating the decay rate for the diphoton decay. For the massless photons Equation (A.7) reads

$$\Gamma = \frac{S|\mathbf{p}||\mathcal{M}|^2}{8\pi m_m^2}, \tag{A.11}$$

where $|\mathbf{p}|$ is the absolute value of the momentum of the outgoing particles. In the meson rest frame, it can be written as $|\mathbf{p}_\gamma| = E_\gamma = E_m = m_m/2$, where E_γ is the energy of the photons and E_m is the energy of the meson. The symmetry factor is $S = 1/2$ because of the two interchangeable photons. Inserting all of this into Equation (A.11) yields

$$\Gamma_{\gamma\gamma} = \frac{|\mathcal{M}|^2}{32\pi m_m}. \tag{A.12}$$

$|\mathcal{M}|^2$ is found by applying the Feynman rules in Table 4.1 to Figure A.2 and squaring the expression, which gives

$$|\mathcal{M}|^2 = |F_m|^2\epsilon_{\mu\nu\rho\sigma}\epsilon_{\mu'\nu'\rho'\sigma'}\epsilon_1^\mu p^\nu\epsilon_2^\rho k^\sigma\epsilon_1^{\mu'}p^{\nu'}\epsilon_2^{\rho'}k^{\sigma'}, \tag{A.13}$$

where p and k are the momenta of the photons, ϵ_1 and ϵ_2 are their polarizations, and $\epsilon_{\mu\nu\rho\sigma}$ is the antisymmetric Levi Civita tensor. Here the form factor $|F_m|^2$

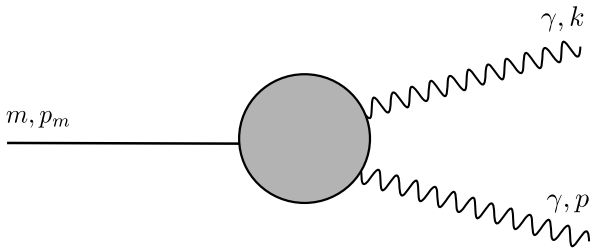

Figure A.2: Feynman diagram of the direct decay of a meson m with four-momentum p_m into two photons with four-momenta k and p.

is constant as both decay products are on-shell. We can simplify the expression by summing over the photon polarization states using Equation (A.26) in [26]:

$$\sum_{\text{polarizations}} \epsilon_\mu \epsilon_{\mu'} \rightarrow -g_{\mu\mu'}. \tag{A.14}$$

Performing this replacement and renaming $\nu \longleftrightarrow \rho$ and $\nu' \longleftrightarrow \rho'$ gives

$$\begin{aligned} |\mathcal{M}|^2 =& |F_m|^2 \epsilon_{\mu\nu\rho\sigma} \epsilon_{\mu'\nu'\rho'\sigma'} g^{\mu\mu'} g^{\rho\rho'} p^\nu k^\sigma p^{\nu'} k^{\sigma'} \\ =& |F_m|^2 \epsilon_{\mu\nu\rho\sigma} \epsilon^{\mu'\nu'}{}_{\rho'\sigma'} p^\nu k^\sigma p^{\nu'} k^{\sigma'}. \end{aligned} \tag{A.15}$$

We can simplify further by using Equation (A.30) from [26]:

$$\epsilon^{\mu\nu\rho'\sigma'} \epsilon_{\mu\nu\rho\sigma} = -2 \left(\delta^{\rho'}_{\rho} \delta^{\sigma'}_{\sigma} - \delta^{\rho'}_{\sigma} \delta^{\sigma'}_{\rho} \right), \tag{A.16}$$

which leaves us with

$$|\mathcal{M}|^2 = -2|F_m|^2 \left(p_\rho p^\rho k_\sigma k^\sigma - p_\sigma p^\rho k_\rho k^\sigma \right) = -2|F_m|^2 \left(p^2 k^2 - (p \cdot k)^2 \right). \tag{A.17}$$

Now we can rewrite $(p \cdot k) = \frac{1}{2}(p+k)^2$ and use that $m_m^2 = (p+k)^2$ to get the final expression for the absolute value of the squared amplitude, which reads

$$|\mathcal{M}|^2 = \frac{|F_m|^2}{2} m_m^4. \tag{A.18}$$

Inserting Equation (A.18) into Equation (A.12) yields the final expression for the diphoton decay rate;

$$\Gamma_{\gamma\gamma} = \frac{|F_m|^2}{64\pi} m_m^3. \tag{A.19}$$

Now it remains to find an expression for the three-body decay rate $\Gamma_{\gamma\bar{\chi}\chi}$ for the decay $P \to \gamma\bar{\chi}\chi$. For this purpose we use Equation (2.10), which in this case is written as

$$\mathrm{d}\Gamma = \frac{1}{(2\pi)^5}\frac{1}{16M^2}|\mathcal{M}|^2\left|\boldsymbol{p}_\chi\right|\left|\boldsymbol{q}\right|\mathrm{d}q\mathrm{d}\Omega_\chi\mathrm{d}\Omega_k, \tag{A.20}$$

where $(|p_\chi|, \Omega_\chi)$ is in the rest frame of χ and $\bar{\chi}$, Ω_k is the solid angle of the photon in the rest frame of the decaying meson, M is the mass of the meson and q is the momentum of the virtual photon. We start by calculating $|\mathcal{M}|^2$. Using the Feynman rules in Table 4.1, the amplitude $\mathcal{M}$ for the Dalitz decay shown in Figure A.3 can be expressed as

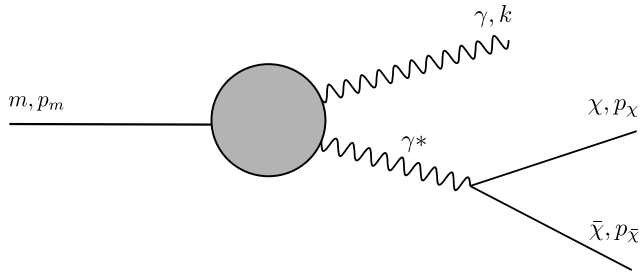

Figure A.3: Feynman diagram of the Dalitz decay of a meson m with 4-momentum p_m into two MCPs χ and $\bar{\chi}$ with 4-momenta p_χ and $p_{\bar{\chi}}$ and a photon γ with four-momentum k. γ^* denotes a virtual photon.

$$\mathcal{M} = |F(q^2)|Q_\chi\epsilon_{\mu\nu\rho\sigma}\frac{1}{q^2}\left[\bar{u}^s(p_-)\gamma^\mu v^s(p_+)\right]q^\nu\epsilon^\rho k^\sigma, \tag{A.21}$$

where $|F(q^2)|$ is the meson form factor, $[\bar{u}^s(p_-)\gamma^\mu v^s(p_+)]$ is the lepton current and ϵ and k are the polarization and momentum of the outgoing photon. Note that now the form factor is no longer constant but depends on q^2 because the decay contains an off-shell photon. The expression for the squared amplitude is then

$$\begin{aligned}|\mathcal{M}|^2 =& \frac{Q_\chi^2}{q^4}|F(q^2)|^2\epsilon_{\mu\nu\rho\sigma}\epsilon_{\mu'\nu'\rho'\sigma'}\left[\bar{u}^s(p_-)\gamma^\mu v^s(p_+)\right] \\ &\times\left[\bar{v}^s(p_+)\gamma^{\mu'}u^s(p_-)\right]q^\nu\epsilon^\rho k^\sigma q^{\nu'}\epsilon^{\rho'}k^{\sigma'}.\end{aligned} \tag{A.22}$$

We start evalutaing this expression by summing over the spins using the completeness relations given in Equation (A.22) in [26]:

$$\begin{aligned}\sum_s u^s(p)\bar{u}^s(p) &= \not{p} + m \\ \sum_s v^s(p)\bar{v}^s(p) &= \not{p} - m\end{aligned} \tag{A.23}$$

to find that

$$\begin{aligned}\sum_{s,s'} \left[\bar{u}_a^s(p_-)\gamma_{ab}^\mu v_b^s(p_+)\right]\left[\bar{v}_c^s(p_+)\gamma_{cd}^{\mu'} u_d^s(p_-)\right] \\ = (\not{p}_+ - m)_{da}\gamma_{ab}^\mu(\not{p}_- + m)_{bc}\gamma_{cd}^{\mu'} \\ = \mathrm{Tr}\left[(\not{p}_+ - m)\gamma^\mu(\not{p}_- + m)\gamma^{\mu'}\right].\end{aligned} \tag{A.24}$$

Evaluating this expression using the formulas for the gamma matrices found in the appendix of [26] and reformulating the expression gives

$$\begin{aligned}4\left[p_-^\mu p_+^{\mu'} + p_-^{\mu'} p_+^\mu - g^{\mu\mu'}\left((p_+ \cdot p_-) + m^2\right)\right] \\ = 2q^2\left[-g^{\mu\mu'} + \frac{p^\mu p^{\mu'}}{q^2} - \frac{(p_+ - p_-)^\mu (p_+ - p_-)^{\mu'}}{q^2}\right],\end{aligned} \tag{A.25}$$

where the mass squared term was dropped due to the small value of the MCP mass, and the relation $q = p_+ + p_-$ was used. The term $(p^\mu p^{\mu'})/q^2$ can be dropped because of the Ward identity, which was described in Section 4.1.2. Inserting into Equation (A.22) we have

$$\begin{aligned}|\mathcal{M}|^2 =& \frac{Q_\chi^2}{q^4}|F(q^2)|^2\epsilon_{\mu\nu\rho\sigma}\epsilon_{\mu'\nu'\rho'\sigma'}2q^2\left[-g^{\mu\mu'} - \frac{(p_+ - p_-)^\mu(p_+ - p_-)^{\mu'}}{q^2}\right] \\ &\times q^\nu \epsilon^\rho k^\sigma q^{\nu'}\epsilon^{\rho'}k^{\sigma'}.\end{aligned} \tag{A.26}$$

Now we use Equation (A.14) in the same manner as earlier together with substituting $k = p_m - q$ and $p_- = q - p_+$. This leaves us with

$$\begin{aligned}|\mathcal{M}|^2 =& \frac{Q_\chi^2}{q^4}|F(q^2)|^2\epsilon_{\mu\nu\rho\sigma}\epsilon_{\mu'\nu'\rho'\sigma'}g^{\nu\nu'}2q^2 \\ &\times\left[-g^{\mu\mu'} - \frac{(2p_+ - q)^\mu(2p_+ - q)^{\mu'}}{q^2}\right] \\ &\times (q^\rho p_m^\sigma - q^\rho q^\sigma)(q^{\rho'}p_m^{\sigma'} - q^{\rho'}q^{\sigma'}).\end{aligned} \tag{A.27}$$

The terms with more than one q with indices from the same metric tensor have to be zero because of the antisymmetry of the metric tensor. Thus, multiplying out we get

$$\begin{aligned}|\mathcal{M}|^2 =& \frac{2\mathrm{e}^2|F(q^2)|^2}{q^2}\Bigg(\varepsilon_{\mu\nu\rho\sigma}\varepsilon^{\mu\nu}{}_{\rho'\sigma'}q^\rho P^\sigma q^{\rho'}P^{\sigma'} \\ &+\frac{4}{q^2}\varepsilon_{\mu\nu\rho\sigma}\varepsilon^{\mu}{}_{\nu'\rho'\sigma'}p_+^\nu p_+^{\nu'}q^\rho q^{\rho'}p_m^\sigma p_m^{\sigma'}\Bigg).\end{aligned} \tag{A.28}$$

In the rest frame of the meson we have that $p_m^\sigma = m_m\delta^{\sigma 0}$. Switching to this frame thus lets us simplify the expression to

$$|\mathcal{M}|^2 = \frac{2\mathrm{e}^2|F(q^2)|^2}{q^2}m_p^2\left(\varepsilon_{\mu\nu\rho}\varepsilon^{\mu\nu}{}_{\rho'}q^\rho q^{\rho'} - \frac{4}{q^2}\varepsilon_{\mu\nu\rho}\varepsilon^{\mu}{}_{\nu'\rho'}p_+^\nu p_+^{\nu'}q^\rho q^{\rho'}\right). \tag{A.29}$$

Finally, we use the tensor properties $\varepsilon_{\mu\nu\rho}\varepsilon^{\mu\nu}{}_{\rho'} = 2\delta_{\rho\rho'}$ and $\varepsilon_{\mu\nu\rho}\varepsilon^{\mu}{}_{\nu'\rho'} = \delta_{\nu\nu'}\delta_{\rho\rho'} - \delta_{\nu\rho'}\delta_{\rho\nu'}$ to get the final expression for the squared amplitude, which reads

$$|\mathcal{M}|^2 = \frac{2\mathrm{e}^2\epsilon^2|F(q^2)|^2m_m^2}{q^2}\left(2|\mathbf{q}|^2 - \frac{4}{q^2}|\mathbf{q}|^2|\mathbf{p}_\chi|^2\sin^2\theta\right), \tag{A.30}$$

where θ is the angle between $\mathbf{p}_\chi$ and $\mathbf{q}$. Now it remains to calculate the partial decay rate. Inserting Equation (A.30) into Equation (A.20) gives

$$\begin{aligned}\mathrm{d}\Gamma = &\frac{1}{(2\pi)^5}\frac{2\mathrm{e}^2\epsilon^2|F(q^2)|^2}{16q^2}\left(2|\mathbf{q}|^2 - \frac{4}{q^2}|\mathbf{q}|^2|\mathbf{p}_\chi|^2\sin^2\theta\right) \\ &\times|\mathbf{p}_\chi||\mathbf{q}|\mathrm{d}\Omega_\chi\mathrm{d}\Omega_k\mathrm{d}q.\end{aligned} \tag{A.31}$$

Using Equations (2.11) and (2.12) we can write

$$|\mathbf{q}| = \frac{m_m^2 - q^2}{2m_m} \tag{A.32}$$

and

$$|\mathbf{p}_\chi| = \frac{qX}{2};\quad X = \sqrt{1 - \frac{4m_\chi^2}{q^2}}, \tag{A.33}$$

which we insert to get

$$\mathrm{d}\Gamma = \frac{\mathrm{e}^2\epsilon^2|F(q^2)|^2}{(2\pi)^5 8q}\left(\frac{m_m^2 - q^2}{2m_m}\right)^3\frac{X}{2}\left(2 - \sin^2\theta X^2\right)\mathrm{d}\Omega_\chi\mathrm{d}\Omega_k\mathrm{d}q. \tag{A.34}$$

Integration over $\mathrm{d}\Omega_k$ gives a factor of 4π. Performing the integration over Ω_k and using the relation $q\mathrm{d}q = \mathrm{d}q^2/2$ gives

$$\mathrm{d}\Gamma = \frac{\mathrm{e}^2\epsilon^2|F(q^2)|^2 X}{(2\pi)^4 16q^2}\left(\frac{m_m^2 - q^2}{2m_m}\right)^3 \left(2 - \sin^2\theta X^2\right)\mathrm{d}\Omega_\chi \mathrm{d}q^2. \tag{A.35}$$

Now we perform the integral over $\mathrm{d}\Omega_\chi = \sin\theta \mathrm{d}\theta\mathrm{d}\phi$ and get

$$\mathrm{d}\Gamma = \frac{\mathrm{e}^2\epsilon^2|F(q^2)|^2}{(2\pi)^3 4q^2}\left(\frac{m_m^2 - q^2}{2m_m}\right)^3 X\left(1 - \frac{X^2}{3}\right)\mathrm{d}q^2. \tag{A.36}$$

We factor out $|F_m|^2$ from $|F(q)|^2$, which means changing $|F(q)|^2$ in our equation with $|F_m|^2|F_m(q^2)|^2$. Inserting $e^2 = 4\pi\alpha$ and the expression for X in Equation (A.33), together with simplifying our expression, we end up with

$$\begin{aligned}\Gamma =& \frac{m_m^3|F_m|^2}{64\pi}\frac{2\alpha\epsilon^2}{3\pi}\int \frac{1}{q^2}\left(1 - \frac{q^2}{m_m^2}\right)^3\left(1 - \frac{4m_\chi^2}{q^2}\right)^{1/2} \\ &\times \left(1 + \frac{2m_\chi^2}{q^2}\right)|F_m(q^2)|^2\mathrm{d}q^2.\end{aligned} \tag{A.37}$$

Noting that the first term is equal to the expression for $\Gamma_{\gamma\gamma}$ in Equation (A.19) allows us to write

$$\frac{\Gamma}{\Gamma_{\gamma\gamma}} = \int \frac{2\alpha\epsilon^2}{3\pi q^2}\left(1 - \frac{q^2}{m_m^2}\right)^3\left(1 - \frac{4m_\chi^2}{q^2}\right)^{1/2}\left(1 + \frac{2m_\chi^2}{q^2}\right)|F_m(q^2)|^2\mathrm{d}q^2, \tag{A.38}$$

which is equivalent to the expression found in [8], [46]:

$$\begin{aligned}\frac{\mathrm{BR}(P \to \gamma\bar{\chi}\chi)}{\mathrm{BR}(m \to \gamma\gamma)} =& \frac{2\alpha\varepsilon^2}{3\pi}\int_{4m_\chi^2}^{m_\mathrm{m}^2} \mathrm{d}q^2\sqrt{1 - \frac{4m_\chi^2}{q^2}}\left(1 + 2\frac{m_\chi^2}{q^2}\right) \\ &\times \frac{1}{q^2}\left(1 - \frac{q^2}{m_m^2}\right)^3\left|F_m\left(q^2\right)\right|^2.\end{aligned} \tag{A.39}$$

Appendix B

Dalitz plots[†]

It is interesting to investigate whether assuming constant matrix elements in the calculations of the MCP flux above $\gamma = 6$ is a reasonable approximation or not. To do this we make Dalitz plots for the Dalitz decays of η and π^0 for different values of the MCP mass. We use the `phasespace` package [35] to get an array of valid decays containing the momenta of the decay products. 100 000 simulations were run, producing the same amount of data points for the plots. For each decay, we easily find the values of m_{12} and m_{23} as defined by Equation (2.9). The corresponding value of $|\mathcal{M}|^2$ is calculated using Equation (A.30).

The Dalitz plots for η are shown in Figure B.1, and the Dalitz plots for π^0 are shown in Figure B.2. The values of $|\mathcal{M}|^2$ have been rescaled so that the maximum value is 1. Note that the x- and y-axes are different for each of the subplots, as the allowed phase space area decreases with increased MCP mass.

The only parameters that change our Dalitz plots are the values of the meson mass and the MCP mass. The limits of the allowed kinematic region are defined as illustrated in Figure 2.2. Thus, the shape and the values of the Dalitz plots for η and π^0 are the same for equal ratios of the meson mass versus MCP mass.

As can be seen from the Dalitz plots in Figure B.1 and Figure B.2, $|\mathcal{M}|^2$ is not constant, but has regions of higher values. These regions are smaller for smaller values of m_χ. For values of m_χ close to the limit of the maximum value possible, corresponding to the lower right Dalitz plots, the region of the higher values of $|\mathcal{M}|^2$ is larger. It can be argued that as long as the region of higher values of $|\mathcal{M}|^2$ stays small, it will not affect the results significantly.

[†]Adapted from [1].

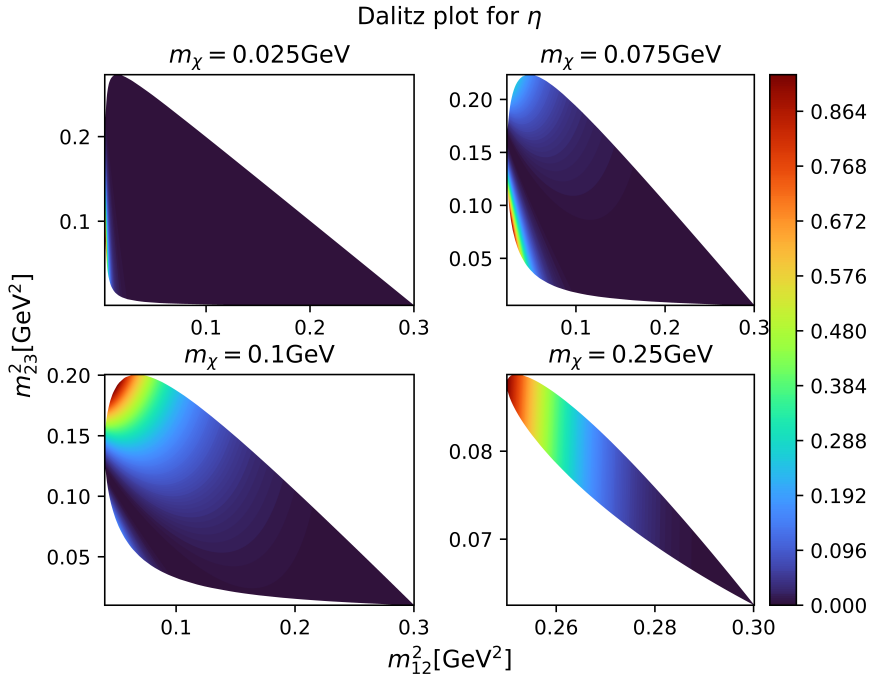

Figure B.1: Dalitz plot for the decay of η mesons into two MCPs and a photon. The subplots correspond to different values of the MCP mass. The colour map shows the normalized values of the squared amplitude.

In order to further investigate the impact of assuming a constant matrix element, we calculate the variance for $|\mathcal{M}|^2$ for each of the plots in Figure B.1 and Figure B.2. The results are shown in Table B.1. The calculated variances for the MCP masses chosen for the plots in Figure B.1 and Figure B.2 were between 0.063 and 0.097. The variance was larger for smaller values of m_χ, for which there is a sharper increase of $|\mathcal{M}|^2$ towards the left of the allowed kinematical region in the Dalitz plot.

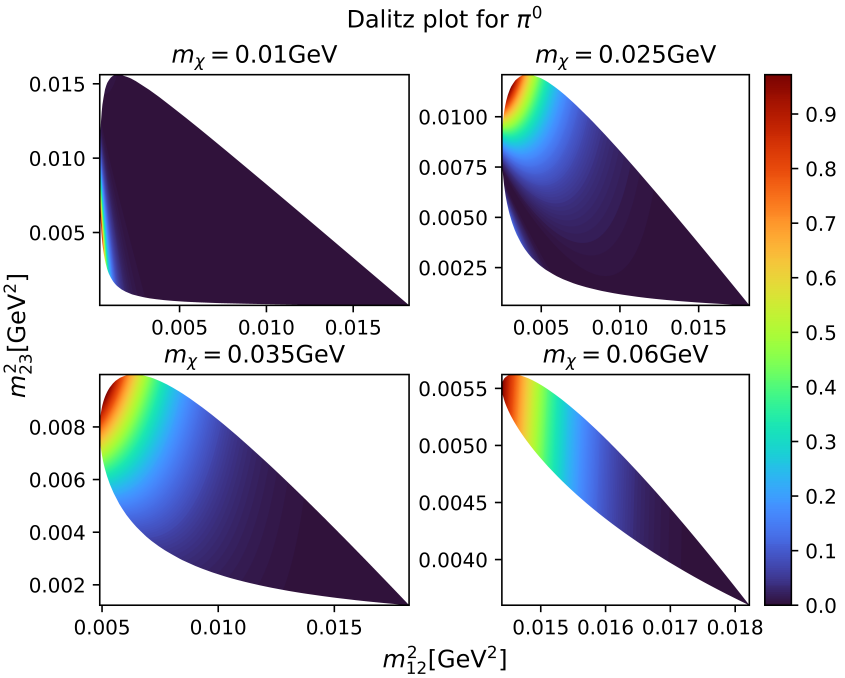

Figure B.2: Dalitz plot for the decay of π^0 mesons into two MCPs and a photon. The subplots correspond to different values of the MCP mass. The colour map shows the normalized values of the squared amplitude.

Table B.1: Variances σ^2 of $|\mathcal{M}|^2$ in the Dalitz plots for the Dalitz decays of the η and π^0 mesons into MCPs. The variance is calculated for different values of the MCP mass m_χ.

Table B.2: η

m_χ [GeV]	σ^2
0.025	0.097
0.075	0.087
0.100	0.078
0.250	0.063

Table B.3: π^0

m_χ [GeV]	σ^2
0.010	0.095
0.075	0.080
0.100	0.071
0.250	0.065

Bibliography

[1] K. Schuller, *Millicharged Particles*. Norwegian University of Science and Technology, 2022.

[2] G. Bertone, *Particle Dark Matter: Observations, Models and Searches*. Cambridge: Cambridge University Press, 2010.

[3] F. Zwicky, "Die rotverschiebung von extragalaktischen nebeln," *Helvetica physica acta*, vol. 6, pp. 110–127, 1933.

[4] J. de Swart, G. Bertone, and J. van Dongen, "How Dark Matter Came to Matter," *Nature Astron.*, vol. 1, p. 0059, 2017. DOI: 10.1038/s41550017-0059. arXiv: 1703.00013.

[5] V. C. Rubin and W. K. Ford Jr, "Rotation of the andromeda nebula from a spectroscopic survey of emission regions," *The Astrophysical Journal*, vol. 159, p. 379, 1970.

[6] G. Bertone and D. Hooper, "History of dark matter," *Rev. Mod. Phys.*, vol. 90, no. 4, p. 045 002, 2018. DOI: 10.1103/RevModPhys.90.045002. arXiv: 1605.04909.

[7] L. Bergstrom, "Non-baryonic dark matter: Observational evidence and detection methods," *Reports on Progress in Physics*, vol. 63, no. 5, pp. 793–841, 2000. DOI: 10.1088/0034-4885/63/5/2r3.

[8] M. Kachelrieß and J. Tjemsland, "Meson production in air showers and the search for light exotic particles," *Astropart. Phys.*, vol. 132, p. 102 622, 2021. DOI: 10.1016/j.astropartphys.2021.102622. arXiv: 2104.06811.

[9] S. Davidson, S. Hannestad, and G. Raffelt, "Updated bounds on millicharged particles," *JHEP*, vol. 05, p. 003, 2000. DOI: 10.1088/1126-6708/2000/05/003. arXiv: hep-ph/0001179.

[10] J. Beringer, J. F. Arguin, R. M. Barnett, *et al.*, "Review of particle physics," *Phys. Rev. D*, vol. 86, p. 010 001, 1 2012. DOI: 10.1103/PhysRevD.86.010001.

[11] D. Griffiths, *Introduction to elementary particles*. Weinheim: Viley-VCH, 2008, ISBN: 9783527406012.

[12] R. L. Workman, V. D. Burkert, V. Crede, *et al.*, "Review of Particle Physics," *Progress of Theoretical and Experimental Physics*, vol. 2022, no. 8, 2022. DOI: 10.1093/ptep/ptac097.

[13] E. Byckling, *Particle kinematics*. London: Wiley, 1973, ISBN: 0471128856.

[14] R. Plestid, V. Takhistov, Y.-D. Tsai, T. Bringmann, A. Kusenko, and M. Pospelov, "New Constraints on Millicharged Particles from Cosmic-ray Production," *Phys. Rev. D*, vol. 102, p. 115 032, 2020. DOI: 10.1103/PhysRevD.102.115032. arXiv: 2002.11732.

[15] C. A. Argüelles, K. J. Kelly, and V. M. Muñoz, "Millicharged particles from the heavens: Single-and multiple-scattering signatures," *Journal of High Energy Physics*, vol. 2021, no. 11, pp. 1–34, 2021. DOI: 10.1007/JHEP11(2021)099. arXiv: 2104.13924.

[16] R. Acciarri *et al.*, "Improved Limits on Millicharged Particles Using the ArgoNeuT Experiment at Fermilab," *Phys. Rev. Lett.*, vol. 124, no. 13, p. 131 801, 2020. DOI: 10.1103/PhysRevLett.124.131801. arXiv: 1911.07996.

[17] A. A. Prinz *et al.*, "Search for millicharged particles at SLAC," *Phys. Rev. Lett.*, vol. 81, pp. 1175–1178, 1998. DOI: 10.1103/PhysRevLett.81.1175. arXiv: hep-ex/9804008.

[18] J. Alvey, M. D. Campos, M. Fairbairn, and T. You, "Detecting light dark matter via inelastic cosmic ray collisions," *Phys. Rev. Lett.*, vol. 123, p. 261 802, 26 2019. DOI: 10.1103/PhysRevLett.123.261802.

[19] S. Roesler, R. Engel, and J. Ranft, "The monte carlo event generator DPMJET-III," in *Advanced Monte Carlo for Radiation Physics, Particle Transport Simulation and Applications*, Springer Berlin Heidelberg, 2001, pp. 1033–1038. DOI: 10.1007/978-3-642-18211-2_166.

[20] F. Riehn, H. P. Dembinski, R. Engel, A. Fedynitch, T. K. Gaisser, and T. Stanev, "The hadronic interaction model sibyll 2.3c and feynman scaling," 2017. DOI: 10.48550/ARXIV.1709.07227.

[21] T. Sjöstrand, S. Ask, J. R. Christiansen, *et al.*, "An introduction to pythia 8.2," *Computer Physics Communications*, vol. 191, pp. 159–177, 2015. DOI: https://doi.org/10.1016/j.cpc.2015.01.024.

[22] N. Arefyeva, S. Gninenko, D. Gorbunov, and D. Kirpichnikov, *Passage of millicharged particles in the electron beam-dump: Refining constraints from slacmq and estimating sensitivity of na64e*, 2022. DOI: 10.1103/PhysRevD.106.035029. arXiv: 2204.03984.

[23] S. Fukuda, Y. Fukuda, T. Hayakawa, *et al.*, "The super-kamiokande detector," *Nuclear Instruments and Methods in Physics Research Section A: Accelerators, Spectrometers, Detectors and Associated Equipment*, vol. 501, no. 2, pp. 418–462, 2003. DOI: https://doi.org/10.1016/S0168-9002(03)00425-X.

[24] K. Bays *et al.*, "Supernova Relic Neutrino Search at Super-Kamiokande," *Phys. Rev. D*, vol. 85, p. 052 007, 2012. DOI: 10.1103/PhysRevD.85.052007. arXiv: 1111.5031.

[25] A. Blackman, *Aylward and Findlay's SI Chemical Data*. Milton: John Wiley & Sons, 2014, ISBN: 9780730302469.

[26] M. E. Peskin and D. V. Schroeder, *An introduction to quantum field theory*. Reading, Mass: Addison-Wesley, 1995, ISBN: 0-201-50397-2.

[27] M. D. Schwartz, *Quantum field theory and the standard model*. Cambridge: Cambridge University Press, 2014, ISBN: 9781107034730.

[28] P.-K. Hu, A. Kusenko, and V. Takhistov, "Dark cosmic rays," *Physics Letters B*, vol. 768, pp. 18–22, 2017. DOI: https://doi.org/10.1016/j.physletb.2017.02.035.

[29] F. Birch, "Elasticity and constitution of the earth's interior," *Journal of Geophysical Research (1896-1977)*, vol. 57, no. 2, pp. 227–286, 1952. DOI: https://doi.org/10.1029/JZ057i002p00227.

[30] M. Javoy, "Chemical earth models," *Comptes Rendus de l'Académie des Sciences - Series IIA - Earth and Planetary Science*, vol. 329, no. 8, pp. 537–555, 1999. DOI: https://doi.org/10.1016/S1251-8050(00)87210-9.

[31] W. Mooney, "1.11 - crust and lithospheric structure - global crustal structure," in *Treatise on Geophysics (Second Edition)*, Oxford: Elsevier, 2015, pp. 339–390, ISBN: 978-0-444-53803-1. DOI: https://doi.org/10.1016/B978-0-444-53802-4.00010-5.

[32] R. Gandhi, C. Quigg, M. H. Reno, and I. Sarcevic, "Ultrahigh-energy neutrino interactions," *Astropart. Phys.*, vol. 5, pp. 81–110, 1996. DOI: 10.1016/0927-6505(96)00008-4. arXiv: hep-ph/9512364.

[33] L. D. Landau, *The Classical Theory of Fields.* (COURSE OF THEORETICAL PHYSICS). Pergamon, 1980, vol. 4th ed, ISBN: 9780080250724.

[34] A. Belyaev, N. D. Christensen, and A. Pukhov, "CalcHEP 3.4 for collider physics within and beyond the standard model," *Computer Physics Communications*, vol. 184, no. 7, pp. 1729–1769, 2013. DOI: 10.1016/j.cpc.2013.01.014.

[35] A. Puig and J. Eschle, "Phasespace: N-body phase space generation in python," *Journal of Open Source Software*, 2019. DOI: 10.21105/joss.01570.

[36] F. E. James, "Monte carlo phase space," CERN, Tech. Rep., 1968.

[37] DEFENSE MAPPING AGENCY WASHINGTON DC, *Department of Defense World Geodetic System 1984: Its Definition and Relationships with Local Geodetic Systems. Second Edition*, 1991. https://apps.dtic.mil/sti/citations/ADA280358.

[38] K. Abe, C. Bronner, Y. Hayato, *et al.*, "First gadolinium loading to super-kamiokande," *Nuclear Instruments and Methods in Physics Research Section A: Accelerators, Spectrometers, Detectors and Associated Equipment*, vol. 1027, p. 166 248, 2022. DOI: https://doi.org/10.1016/j.nima.2021.166248.

[39] Kamiokande Collaboration, M. Shinoki, K. Abe, *et al.*, *Measurement of the cosmogenic neutron yield in super-kamiokande with gadolinium loaded water*, 2022. DOI: 10.48550/ARXIV.2212.10801.

[40] M. Yokoyama, *The hyper-kamiokande experiment*, 2017. DOI: 10.48550/ARXIV.1705.00306.

[41] G. Alimonti, C. Arpesella, H. Back, *et al.*, "The borexino detector at the laboratori nazionali del gran sasso," *Nuclear Instruments and Methods in Physics Research Section A: Accelerators, Spectrometers, Detectors and Associated Equipment*, vol. 600, no. 3, pp. 568–593, 2009. DOI: https://doi.org/10.1016/j.nima.2008.11.076.

[42] Borexino Collaboration, M. Agostini, K. Altenmüller, *et al.*, "Correlated and integrated directionality for sub-mev solar neutrinos in borexino," *Phys. Rev. D*, vol. 105, p. 052 002, 5 2022. DOI: 10.1103/PhysRevD.105.052002.

[43] M. Kachelrieß, *Quantum fields : from the Hubble to the Planck Scale*. Oxford: Oxford University Press, 2018, ISBN: 0-19-184133-1.

[44] X. Chu, J.-L. Kuo, and J. Pradler, "Dark sector-photon interactions in proton-beam experiments," *Phys. Rev. D*, vol. 101, no. 7, p. 075 035, 2020. DOI: 10.1103/PhysRevD.101.075035. arXiv: 2001.06042.

[45] M. C. Kunkel, *Photoproduction of 7π 0 on hydrogen with CLAS from 1.1 GeV-5.45 GeV using e+e–γ decay*. Old Dominion University, 2014.

[46] L. G. Landsberg, "Electromagnetic Decays of Light Mesons," *Phys. Rept.*, vol. 128, pp. 301–376, 1985. DOI: 10.1016/0370-1573(85)90129-2.

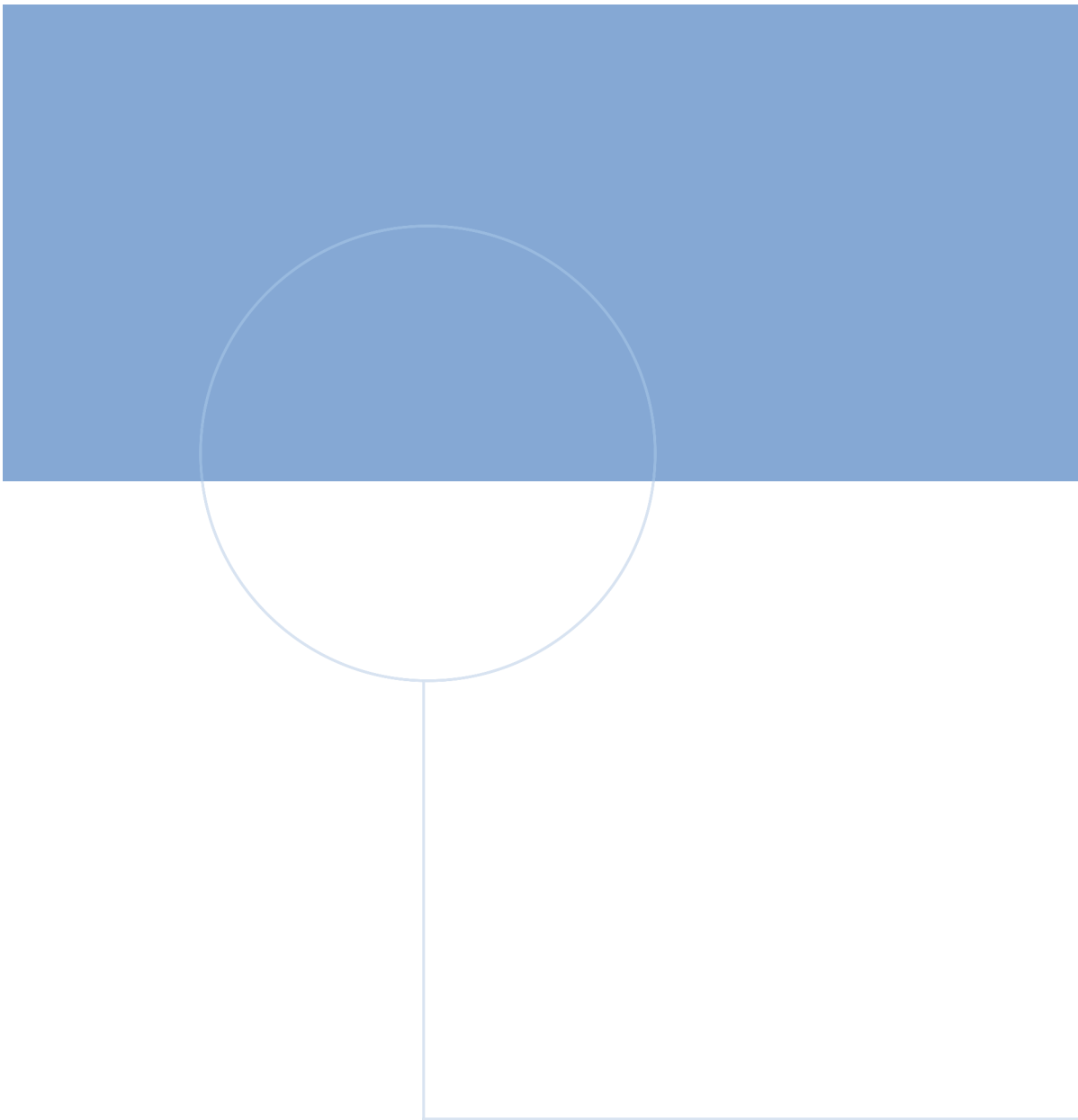

NTNU

Norwegian University of
Science and Technology